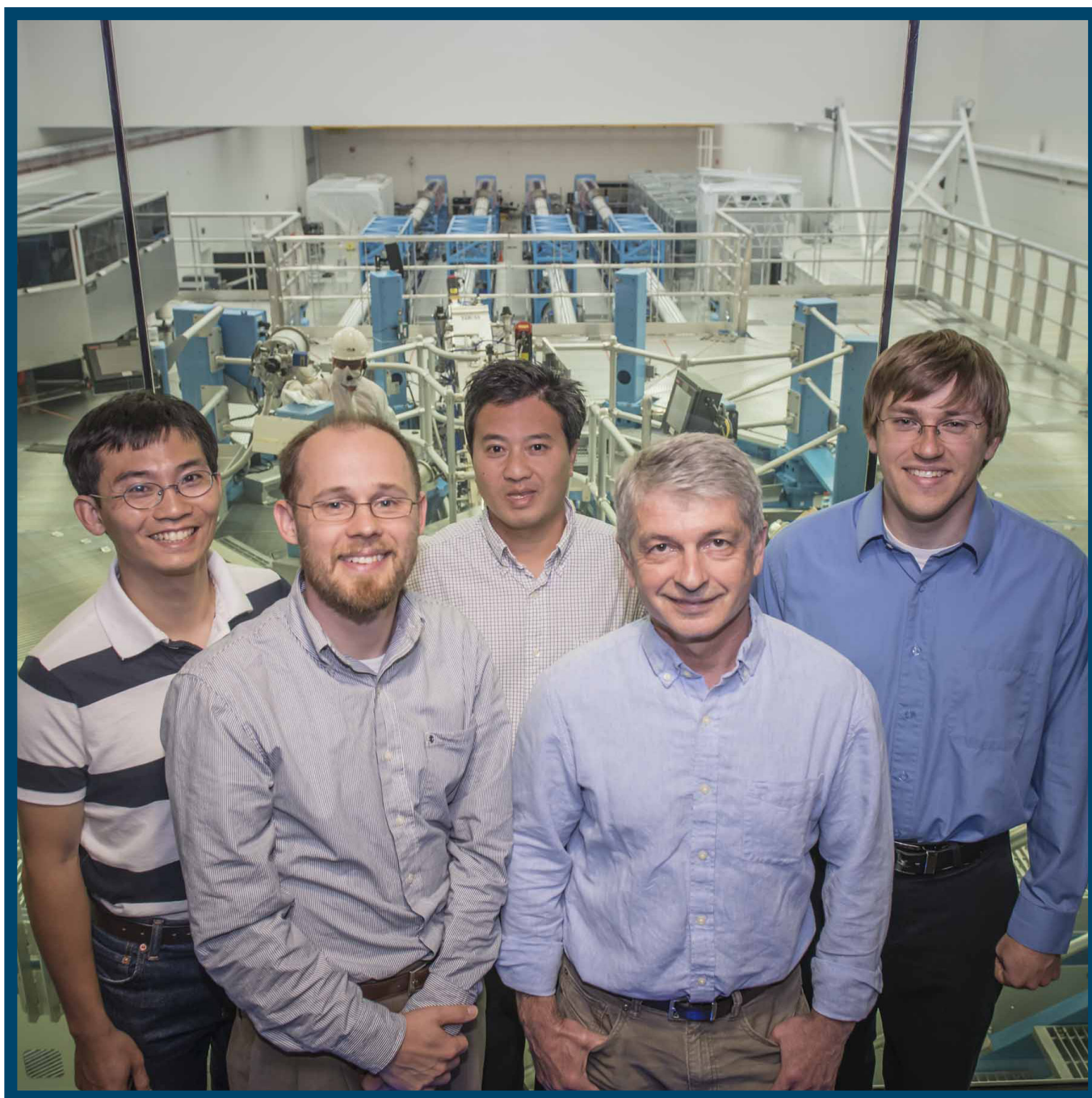


LLE Review

Quarterly Report



About the Cover:

The photograph on the cover presents (left to right) P.-Y. Chang, W. Fox, S. X. Hu, G. Fiksel, and D. H. Barnak, who report on demonstrating the magnetic reconnection between colliding magnetized, laser-produced plasma plumes in experiments on the OMEGA EP Laser System (p. 153). This work is a result of a collaboration between researchers from Princeton University, the University of New Hampshire, and LLE under the National Laser Users' Facility Program. The photograph is taken in the OMEGA EP viewing gallery and shows the Laser Bay, with four beamlines in the background.

The photograph below shows G. Fiksel (center) and W. Fox (right) in the OMEGA EP control room during an experiment. G. Fiksel points to the image of the experimental setup explained in Fig. 139.1 (p. 153).



This report was prepared as an account of work conducted by the Laboratory for Laser Energetics and sponsored by New York State Energy Research and Development Authority, the University of Rochester, the U.S. Department of Energy, and other agencies. Neither the above-named sponsors nor any of their employees makes any warranty, expressed or implied, or assumes any legal liability or responsibility for the accuracy, completeness, or usefulness of any information, apparatus, product, or process disclosed, or represents that its use would not infringe privately owned rights. Reference herein to any specific commercial product, process, or service by trade name, mark, manufacturer, or otherwise, does not necessarily constitute or imply its endorsement, recommendation, or favoring

by the United States Government or any agency thereof or any other sponsor. Results reported in the LLE Review should not be taken as necessarily final results as they represent active research. The views and opinions of authors expressed herein do not necessarily state or reflect those of any of the above sponsoring entities.

The work described in this volume includes current research at the Laboratory for Laser Energetics, which is supported by New York State Energy Research and Development Authority, the University of Rochester, the U.S. Department of Energy Office of Inertial Confinement Fusion under Cooperative Agreement No. DE-NA00001944, and other agencies.

Printed in the United States of America

Available from

National Technical Information Services
U.S. Department of Commerce
5285 Port Royal Road
Springfield, VA 22161
www.ntis.gov

For questions or comments, contact Andrey Solodov, Editor, Laboratory for Laser Energetics, 250 East River Road, Rochester, NY 14623-1299, (585) 273-3686.

Worldwide-Web Home Page: <http://www.lle.rochester.edu/>
(Color online)

LLE Review

Quarterly Report



Contents

In Brief	iii
Magnetic Reconnection Between Colliding Magnetized, Laser-Produced Plasma Plumes	153
Implosion Dynamics in Direct-Drive Experiments	158
X-Ray Continuum as a Measure of Pressure and Fuel–Shell Mix in Compressed Isobaric Hydrogen Implosion Cores	166
Soft X-Ray Backlighting of Cryogenic Implosions Using a Narrowband Crystal Imaging System	184
Time-Resolved Compression of a Spherical Shell with a Re-Entrant Cone to High Areal Density for Fast-Ignition Laser Fusion	191
Precompensation of Gain Nonuniformity in a Nd:Glass Amplifier Using a Programmable Beam-Shaping System	198
A New Neutron Time-of-Flight Detector for a Fuel-Areal-Density Measurements on OMEGA	208
Publications and Conference Presentations	

In Brief

This volume of the LLE Review, covering April–June 2014, features “Magnetic Reconnection Between Colliding Magnetized, Laser-Produced Plasma Plumes,” by G. Fiksel, D. H. Barnak, P.-Y. Chang, and P. M. Nilson, and S. X. Hu (LLE and Fusion Science Center); W. Fox and A. Bhattacharjee (Princeton University); and K. Germaschewski (University of New Hampshire). This article (p. 153) reports on the first demonstration of magnetic reconnection between colliding plumes of externally magnetized, laser-produced high-energy-density plasmas. Two counter-propagating plasma flows are created by IR-radiating oppositely placed plastic targets with 1.8-kJ, 2-ns laser beams on the OMEGA EP Laser System. The two plumes are magnetized by an externally controlled magnetic field, imposed perpendicular to the plasma flow. The interaction region is prefilled with a low-density background plasma. The counter-flowing plumes sweep up and compress the magnetic field and the background plasma into a pair of magnetized ribbons, which collide, stagnate, and reconnect at the midplane, allowing for the first detailed observation of a stretched current sheet in laser-driven reconnection experiments. The dynamics of current sheet formation is in good agreement with first-principles particle-in-cell simulations that model the experiments.

Additional highlights of research presented in this issue include the following:

- D. T. Michel, R. S. Craxton, A. K. Davis, R. Epstein, V. Yu. Glebov, V. N. Goncharov, S. X. Hu, I. V. Igumenshchev, D. D. Meyerhofer, P. B. Radha, T. C. Sangster, W. Seka, C. Stoeckl, and D. H. Froula investigate two approaches to increase the ablation pressure that can help to achieve implosion performance on the OMEGA laser that are hydrodynamically scalable to ignition at the National Ignition Facility (p. 158). An increased ablation pressure will allow a more-massive shell and a higher adiabat to achieve ignition-relevant velocities, areal densities, and hot-spot pressures. A target design that uses a Be ablator is shown to increase the hydrodynamic efficiency, resulting in a ~10% increase in the ablation pressure, compared to the standard CH ablator. Reducing the beam size is shown to recover all of the ablation pressure lost to cross-beam energy transfer (CBET), but the illumination uniformity reduces the integrated target performance. The hydrodynamic efficiency is measured for the current cryogenic design, multiple ablator material design, and various beam focal-spot sizes. In each case, an excellent agreement is observed with hydrodynamic simulations performed by *LILAC* when CBET and nonlocal heat transport models are included.
- R. Epstein, V. N. Goncharov, F. J. Marshall (LLE); R. Betti, R. Nora, and A. R. Christopherson (LLE and Fusion Science Center); and I. E. Golovkin and J. J. MacFarlane (Prism Computational Sciences) describe how x-ray spectral measurements can be used to infer pressure and fuel–shell mix in compressed isobaric hydrogen-implosion cores (p. 166). At high spectral energy, where the x-ray emission from an imploded hydrogen core is optically thin, the emissivity profile can be measured directly. This emissivity, which can be modeled accurately under hot-core conditions, is dependent almost entirely on the pressure when measured within a restricted spectral range matched to the temperature range anticipated for the emitting volume. In this way, the measured free-free emissivity profile becomes a direct measure of the hot-core pressure at the time of peak emission as well as a test of the isobaric assumption. The pressure and temperature dependences of the x-ray emissivity and the neutron-production rate explain a simple scaling of the total filtered x-ray emission as a constant power of the total neutron yield for implosions of targets of similar design over a broad range of shell-implosion isentropes. The hot-spot “fuel–shell” mix mass can be inferred by attributing the excess emission from less-stable, low-isentrope implosions (above the level expected from this neutron-yield scaling) to the higher emissivity of shell carbon mixed into the implosion central hot spot.

- C. Stoeckl, M. Bedzyk, G. Brent, R. Epstein, G. Fiksel, D. Guy, V. N. Goncharov, S. X. Hu, S. Ingraham, D. W. Jacobs-Perkins, R. K. Jungquist, F. J. Marshall, C. Mileham, P. M. Nilson, T. C. Sangster, M. J. Shoup III, and W. Theobald report on soft x-ray backlighting of cryogenic implosions on OMEGA using a narrowband crystal imaging system (p. 184). High-energy petawatt lasers such as OMEGA EP promise significantly improved backlighting capabilities by generating high x-ray intensities and short emission times. A narrowband x-ray imager with an astigmatism-corrected bent quartz crystal for the Si He α line was developed to record backlit images of cryogenic direct-drive implosions. A time-gated recording system minimized the self-emission of the imploding target. A fast target-insertion system capable of moving the backlighter target ~ 7 cm in ~ 100 ms was developed to avoid interference with the cryogenic shroud system. With backlighter laser energies of ~ 1.25 kJ at a 10-ps pulse duration, the radiographic images show a high signal-to-background ratio of $>100:1$ and a spatial resolution of the order of 10 μ m. The backlit images can be used to assess the symmetry of the implosions close to stagnation and the mix of ablator material into the dense shell.
- W. Theobald, A. A. Solodov, C. Stoeckl, K. S. Anderson, R. Epstein, G. Fiksel, V. Yu. Glebov, S. Ivancic, F. J. Marshall, G. McKiernan, C. Mileham, P. M. Nilson, T. C. Sangster, and A. Shvydky (LLE); F. N. Beg and L. C. Jarrott (University of California, San Diego); E. M. Giraldez, R. B. Stephens, and M. S. Wei (General Atomics); and H. Habara (Osaka University) report on picosecond time-resolved, monochromatic, 8-keV x-ray radiographic measurements of imploded cone-in-shell targets on OMEGA that provide, for the first time, a detailed quantitative study of the hydrodynamic evolution of non-symmetrically imploded high-density matter up to peak compression (p. 191). An excellent agreement with predictions from two-dimensional radiation-hydrodynamic simulations with the code *DRACO* is found. This work is an important step forward for fast ignition because it demonstrates that sufficient areal density can be compressed in nonspherical implosions to stop that part of the fast-electron spectrum (\sim mega-electron volt) that is relevant for fast ignition.
- S.-W. Bahk, I. A. Begishev, and J. D. Zuegel demonstrate precompensation of gain nonuniformity in a Nd:glass amplifier using a programmable beam-shaping system (p. 198). A programmable liquid crystal beam-shaping system was installed for a 200-mJ optical parametric chirped-pulse-amplification system front end and was applied to dramatically improve the beam uniformity in the subsequent amplifier. A highly nonuniform beam profile caused by gain inhomogeneity in the amplifier was precompensated by the beam-shaping system using significantly improved open-loop and closed-loop algorithms. The details of the improved algorithms are described. The issues of running a liquid crystal device with a high-energy, ultrashort-pulse laser, such as damage risk and temporal contrast degradation, are addressed.
- V. Yu. Glebov, C. J. Forrest, K. L. Marshall, M. Romanofsky, T. C. Sangster, M. J. Shoup III, and C. Stoeckl describe a new neutron time-of-flight (nTOF) detector installed on the OMEGA Laser System to measure fuel-areal-density cryogenic DT implosions (p. 208). The nTOF detector has a cylindrical thin-wall, stainless-steel, 8-in.-diam, 4-in.-thick cavity filled with an oxygenated liquid xylene scintillator. Four gated photomultiplier tubes (PMT's) with different gains are used to measure primary DT and D₂ neutrons, down-scattered neutrons in nT and nD kinematic edge regions, and to study tertiary neutrons in the same detector. The nTOF detector is located 13.4 m from target chamber center in a well-collimated line of sight. The design details of the nTOF detector, PMT optimization, and test results on OMEGA are presented.

Andrey Solodov
Editor

Magnetic Reconnection Between Colliding Magnetized, Laser-Produced Plasma Plumes

Throughout the universe, magnetic reconnection makes it possible for the magnetic field to change its topology and thereby allow an explosive release of stored energy.¹⁻³ Some vivid examples of magnetic reconnection are solar flares,⁴ sawtooth crashes and relaxation processes in tokamaks and reversed-field pinches,^{5,6} and magnetospheric substorms.^{4,7} Magnetic reconnection in high-energy-density (HED) plasma is of great interest because of the indication of the major role it plays in astrophysical phenomena such as accretion disks and stellar flares.⁸⁻¹⁰ The laboratory-based experimental study of magnetic reconnection in HED plasma is a relatively recent development. These experiments studied the reconnection of the self-generated (e.g., Biermann battery) magnetic fields between colliding laser-produced plasma plumes.¹¹⁻¹⁵ Magnetic-field destruction¹² has been observed, as well as plasma jets^{11,13-15} and electron energization.¹⁵

This article presents, for the first time, results of the reconnection of an externally applied magnetic field by counter-propagating, colliding HED plasmas. These experiments are based on new techniques that externally control the magnetization of ablated plasma plumes. This allows one to directly compare experiments with and without an external magnetic field. The results obtained here are completely different from recent experiments with zero external magnetic fields that are dominated by the collisionless interpenetration of two plasma streams and the generation of Weibel instability.¹⁶ The geometry of this externally magnetized plasma experiment makes it amenable to end-to-end simulation with particle-in-cell codes modeling the entire progression of the experiment, including plasma formation and the assembly of the current sheet. While previous results in HED plasmas could infer reconnection through destruction of the magnetic field,¹² this work is the first to observe clear stagnation of the counter-propagating magnetized ribbons and the formation of an extended current sheet. The current sheet stagnates at a width comparable to the ion skin depth and shows the formation of cellular structures that may indicate the formation of magnetic islands or plasmoids. Finally, the magnetic fields in the current sheet are observed to

suddenly and completely annihilate, an effect not yet captured in our two-dimensional (2-D) simulation.

The experiment was carried out on LLE's OMEGA EP Laser System.¹⁷ Figure 139.1 shows the experimental setup. Two counter-propagating plasma plumes were obtained by irradiating oppositely placed plastic (CH), $2 \times 6 \times 0.25\text{-mm}^3$ ablator targets with two 1.8-kJ, 2-ns laser beams (drive beams) at a wavelength of $0.351 \mu\text{m}$ and on-target laser intensities of $5 \times 10^{13} \text{ W/cm}^2$. The targets were separated by the width $2L = 4.25 \text{ mm}$ and the laser beam's incidence angle was $\theta = 74^\circ$, resulting in highly elliptical, $1 \times 3\text{-mm}^2$ focal spots. The highly elongated focal footprint shape conforms to a quasi-2-D geometry, making it suitable for comparison with 2-D simulations.

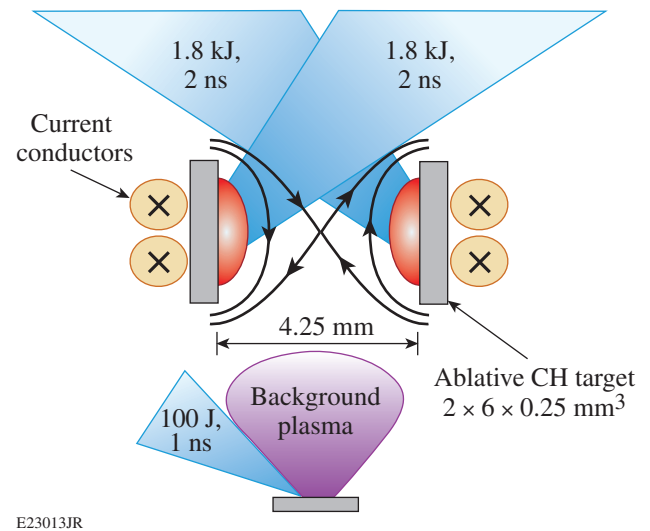


Figure 139.1 Experimental setup. Two counter-propagating plasma plumes were obtained by irradiating with two laser beams opposing plastic (CH) ablator targets. An external magnetic field was created by pulsing an electric current through conductors located directly behind each target. The region between the ablator targets was pre-filled by a tenuous background plasma created by a dedicated laser-ablator pair. A multi-MeV proton beam (not shown) generated with a high-intensity, short-pulse laser beam was used to probe the dynamics and topology of the magnetic field in the interaction region.

An external magnetic field, imposed perpendicular to the plasma flow, was created by current-carrying conductors placed directly behind each target and powered by MIFEDS (magneto-inertial fusion electrical discharge system).¹⁸ The current pulse had a duration of 1 μ s and the drive lasers were fired at the peak of the magnetic field. Two parallel currents (see Fig. 139.1) were used to impose a field with an x-type null point (x point) and field reversal between the colliding plasmas—a typical reconnection geometry.^{1,3} The magnetic-field strength B was monotonically increased from $B = 0$ at the midplane to $B = 8$ T at the targets. The vacuum magnetic flux ($\int B_z dx$ from the foil to the x point) available for reconnection is $\sim 8 \times 10^{-3}$ Tm. In the process of the plumes colliding and merging, the magnetic field is expected to be first compressed into a current sheet, accompanied by reconnection.

The x-point region between the ablaters was prefilled by a tenuous background plasma created by ablating a third target ($2 \times 2 \times 0.25$ mm³ and 7 mm from the x point) with a third laser pulse (100 J, 1 ns), fired 12 ns prior to the main drive beams to give the plume enough time to prefill the interaction volume. These laser and target parameters were chosen experimentally to obtain desirable background plasma parameters at the moment when the drive beams fired. The background plasma facilitates the reconnection by allowing the current through the x-point region. Experiments without a background plasma showed no reconnection.

The dynamics and topology of the magnetic field in the interaction region were probed with proton radiography.¹⁹ This diagnostic used an ultrafast proton beam generated with a high-intensity, short-pulse laser beam (1.053 μ m/800 J/10 ps) focused to a 25- μ m spot on a thin 20- μ m copper foil. The protons, accelerated by the target-normal sheath acceleration (TNSA) mechanism,²⁰ have a broad distribution of energies of the order of 10 MeV and higher. Protons are detected in a stack of radiochromic film (RCF) interleaved with aluminum foils of various thicknesses. The RCF detector is placed 80 mm from the interaction region, for a geometrical magnification of $M = 11$, with proton energies resolved in the film stack by their respective energy-dependent Bragg peaks. The temporal resolution of the detector is ~ 100 ps. While passing through the interaction region (Fig. 139.1), the protons are focused or defocused by magnetic fields in the magnetized plumes, leaving an intensity pattern at the detector. The temporal evolution of the magnetic-field structure was obtained over multiple shots by varying the timing of the proton beam with respect to the drive-laser beams.

A series of representative proton radiography images in Figs. 139.2(a)–139.2(d) illustrate four stages in the magnetic-field evolution: (a) the formation of magnetic “ribbons” and the sweeping up of background plasma and magnetic field, (b) the collision of magnetic ribbons, (c) reconnection, and (d) magnetic-field annihilation. The time stamps on each frame show the time when the proton beam fired relative to the drive beams. Distinctive features common to all the images are the two light-colored curved bands containing a high magnetic field, described here as “magnetic ribbons.” The direction of the vertical component of the magnetic field, upward on the right ribbon and downward on the left ribbon (see Fig. 139.1), is such that the diagnostic protons are deflected outward from each corresponding ribbon. The magnetic field in the ribbons is strong enough to completely deflect the protons from those regions, leaving a deficit of protons and reflected as white, unexposed film. A sharp, “caustic” proton boundary²¹ of very high fluence—a feature well-reproduced in our modeling—appears immediately on the outside of each ribbon, forming an important point of comparison between simulation and experiment.

During the plume expansion stage [Fig. 139.2(a)], the shape of the ribbons is topologically equivalent to the shape of the vacuum magnetic-field lines (Fig. 139.1). At $t = 2.37$ ns, each ribbon has traversed more than halfway to the midplane. The magnetic field in each ribbon has been strongly compressed above the vacuum field, as indicated by a low proton fluence in the ribbons. This stage is a clear manifestation of the initial magnetic field being swept up by the high-pressure plasma plumes, as would be expected by the high plasma pressure compared to the magnetic-field pressure. The degree of field compression by the pileup can be estimated by assuming that all of the initially available flux $\Phi \approx 8$ T mm is compressed into a ribbon with a thickness of $\delta \approx 0.3$ mm, resulting in a compressed field $B_{\text{comp}} \approx \Phi/\delta \approx 25$ T.

At $t = 3.12$ ns [Fig. 139.2(b)], the ribbons collide and flatten out. The magnetic field in the collision region is strongly compressed, expelling virtually all the fast protons. The ribbon width stagnates, indicating stagnation of the plasma flow. Based on the opposing signs of the incoming magnetic fields, the collision of the ribbons must produce a reconnecting current sheet.

Figure 139.2(c) shows the magnetic field at a late nonlinear phase of reconnection, demonstrating a clear evolution in the topology of the current sheet. The plasma elements that were previously connected by the magnetic field (e.g., B and C) are now disconnected. Conversely, plasma elements that were pre-

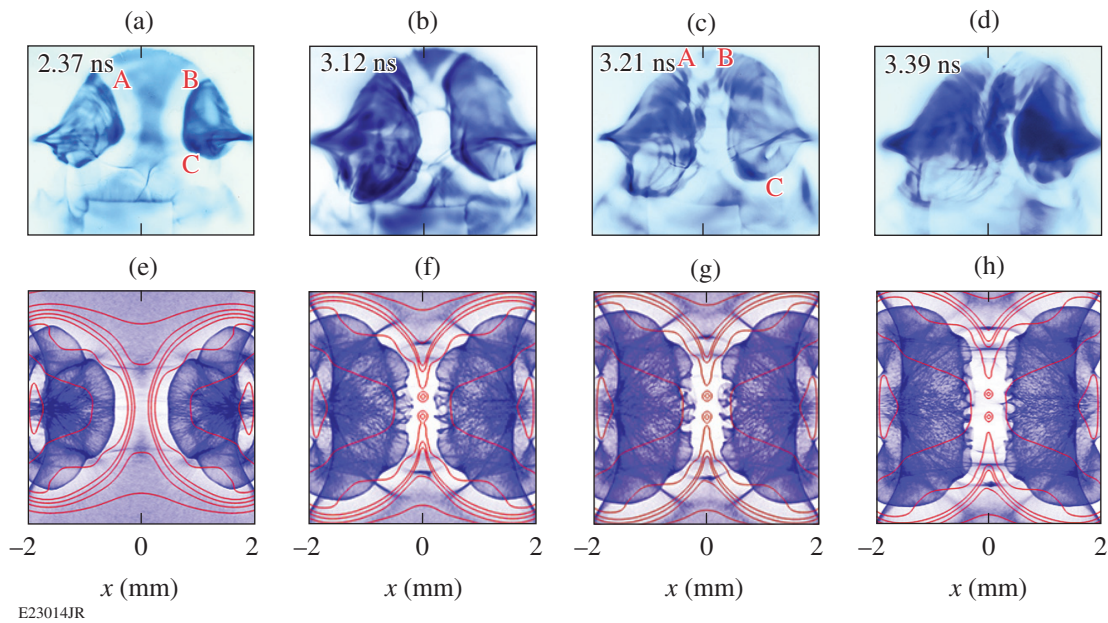


Figure 139.2

Proton radiographic images of the magnetic-field evolution. The ablator targets are situated at the left and right borders of each frame. Dark areas correspond to high proton fluence. The series illustrates four stages in the magnetic-field evolution: (a) formation of magnetic “ribbons” and the sweeping up of background plasma and magnetic field, (b) collision of magnetic ribbons, (c) reconnection, and (d) magnetic-field annihilation. The time stamps on each frame show the time when the proton beam fired relative to the drive beams. The horizontal and vertical scales are the same. [(e)–(h)] Results of simulated proton radiography at the corresponding times are shown in blue, with overlaid magnetic-field lines (red curves).

viously disconnected (e.g., A and B) are now connected by the newly formed outflow magnetic field (V-shaped ribbons at the top and bottom parts of the merged area) that disconnects from the central part of the current sheath and starts moving away. Furthermore, a small number of cellular structures appear, spanning the width of the current sheet. These structures can be plausibly interpreted as magnetic islands or plasmoid structures growing inside the current sheet.

Finally, Fig. 139.2(d) shows the beginning of the disruption of the current sheet and complete annihilation of the magnetic fields, as the protons are no longer defocused from the sheet. The onset of this process may be reflected in the two dark areas at the top of the current sheet in Fig. 139.2(c). The annihilation (and indeed the entire evolution of the ribbons) occurs on a significantly faster time scale than the resistive diffusion (~ 10 ns) through the smallest plasma structures ($\sim 100 \mu\text{m}$), so neither the reconnection nor disruption is due simply to resistive dissipation. (Here, the magnetic-diffusion coefficient $D_m = \eta/\mu_0$ was evaluated from the Spitzer resistivity η at $T_e = 200$ eV, a baseline prediction from simulations with the radiation–hydrodynamics code *DRACO*²² and likely an underestimate of the temperature.)

Figures 139.2(e)–139.2(h) show results of accompanying particle-in-cell (PIC) simulations, which agree with the experiment on a number of features of the colliding ribbons. The 2-D simulations, with the invariant direction parallel to the MIFEDS currents, were conducted with the code *PSC*^{23,24} to help with both design and analysis of the experiments. The code solves the full relativistic, electromagnetic Vlasov–Maxwell system and includes a collision operator implementing Fokker–Planck collisions.²⁴ The PIC model has long been used to simulate magnetic reconnection;^{23,24} in particular, it retains kinetic effects of the electrons in the current sheet, allowing for collisionless reconnection. The simulations provide an end-to-end model of the experiments, starting from the vacuum magnetic field and followed by plasma formation, which is modeled with particle source terms set to obtain profiles similar to that provided by *DRACO*.²² *DRACO* predicts plasma ablation densities near $6 \times 10^{26} \text{ m}^{-3}$ and background plasma densities near $2 \times 10^{24} \text{ m}^{-3}$. Time is calibrated between simulation and experiment by matching the location of the ribbons at 2.37 ns; this corresponds to a sound speed of 1.8×10^5 m/s, which is, in fact, quite close to nominal *DRACO* predictions of 2×10^5 m/s. The magnetic fields were initialized as the vacuum fields from the two

conductors. More-detailed results of these simulations will be reported separately.

Synthetic proton radiographic images are obtained using a proton ray-tracing model. Protons are initialized from a point source and projected through the simulation domain, where they receive an impulse by the line-integrated $v \times B$ force, and are finally projected to the detector. The line integration, since it is along the invariant direction of the simulations, is accounted for by simply multiplying by a characteristic length, taken as 4 mm. The final proton locations are binned to form a fluence image. In Figs. 139.2(e)–139.2(h), magnetic-field lines are shown as red curves, along with simulated proton fluence (blue) for direct comparison.

The simulations show similar formation and collision of magnetized ribbons, stagnation of the flows, and formation of an extended current sheet, which saturates at a width comparable to the ion skin depth. We find excellent agreement and reproduction of the formation of a caustic proton focusing feature on the back side of each ribbon. This feature is tracked in both experiment and simulation with excellent agreement and is shown in Fig. 139.3. The initial inflow speed, based on half the rate of change of the ribbon separation, is $\sim 1 \times 10^6$ m/s. The collision velocity decreases as the ribbons collide and eventually stagnates for $t > 3$ ns.

The reconnection in the simulation occurs in a very fast burst, yielding the magnetic islands already growing and visible in

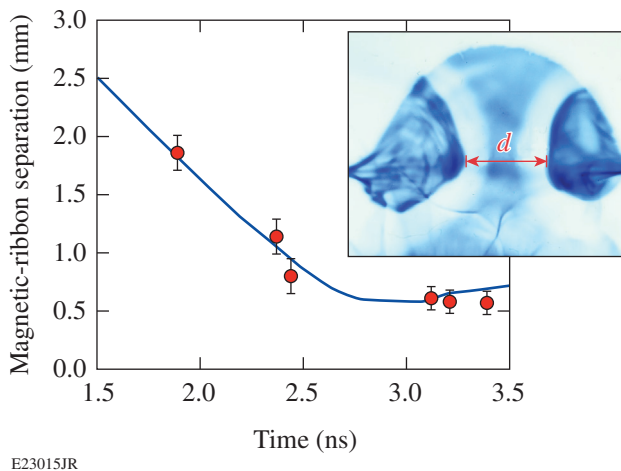


Figure 139.3 Measured time dependence of the separation d between the outer caustic boundaries of the magnetic ribbons (data points) compared with particle-in-cell (PIC) simulations (curve) showing inflow and stagnation of the flows.

the simulations at 3.12 ns. Several profiles of the electric fields constituting different components of the generalized Ohm's law are shown in Fig. 139.4. The peak electric field in the simulations, near 1.5×10^7 V/m, is comparable to “fastest-possible” reconnection rates inferred from reconnection inflows $v_{\text{ribbon}} = 1 \times 10^6$ m/s and B fields of the order of 25 T. Even accounting for flux pileup,²³ the simulated reconnection rates are extremely fast, close to 100% of the local Alfvénic rate $V_A^* B^*$, calculated based on the compressed magnetic fields and the plasma density in the current sheet. We find that the high compressibility of the current sheet, resulting from the supersonic inflows, drives this reconnection rate, which is significantly beyond what can be expected in steady-state reconnection.

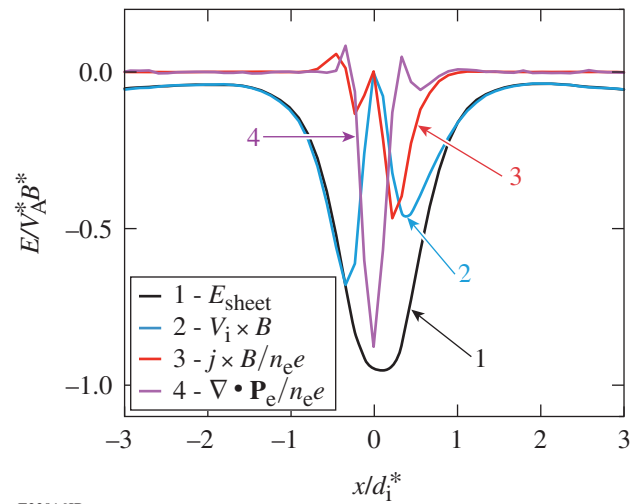


Figure 139.4 Generalized Ohm's law at the peak of reconnection. The (1) total electric field E_{sheet} in the current sheet is compared to (2) the magnetohydrodynamic (MHD) field $V_i \times B$, (3) the Hall field $j \times B/n_e e$, and (4) the electron pressure tensor $\nabla \cdot \mathbf{P}_e/n_e e$. The electric fields are shown in units of $V_A^* B^*$, which are the maximum values of Alfvén speed and the magnetic field across the compressed current sheet. The ion skin depth is d_1^* .

The reconnection phase is followed by a complete magnetic annihilation, which is currently still in disagreement between experiment and simulation. In the simulated proton radiograph, the overall structure of the current sheet persists *after the reconnection* for some time. This is due to a confluence of factors, including a small but finite amount of unreconnected magnetic field upstream and an incomplete outflow of magnetic flux out of the current sheet, but primarily the persistence of the magnetic islands in the current sheet (which have nowhere to go). Despite reconnection and island formation, a finite magnetic field remains in the current sheet and continues to appear in the simulated radiographs. In contrast, by 3.39 ns

in the experimental data, there is a disruption of this current sheet structure, such that protons are no longer deflected at all. It is likely that three-dimensional (3-D) effects not captured in the simulations are important for the fast disruption. Magnetic islands are special structures in 2-D and could exhibit new dynamics in 3-D, allowing for the complete disruption of the sheet current.

In summary, the magnetic reconnection of externally magnetized, colliding plumes of HED plasma has been demonstrated for the first time. The experimental results and numerical simulations show the formation and collision of magnetic ribbons, the pile-up of the magnetic flux, and reconnection of the magnetic field. The reconnection is fast, with a reconnection rate comparable to the Alfvén reconnection rate. The experimental results are generally in very good agreement with first-principles PIC simulations that model the experiments from end to end. Some features of the experiment, however, like the fast annihilation of the current sheet after the reconnection, are not displayed by the 2-D simulations and will be investigated in full-scale, 3-D simulations.

ACKNOWLEDGMENT

This work is supported by the U.S. Department of Energy under Contracts No. DE-NA0001944, DE-SC0007168, DE-SC0008655, and DE-SC0006670; the National Laser Users' Facility program; the University of Rochester; and the New York State Energy Research and Development Authority. The particle-in-cell simulations were conducted on the Jaguar and Titan supercomputers through the Innovative and Novel Computational Impact on Theory and Experiment (INCITE) program. This research used resources of the Oak Ridge Leadership Computing Facility located in the Oak Ridge National Laboratory, which is supported by the Office of Science of the U.S. Department of Energy under Contract No. DE-AC05-00OR22725.

REFERENCES

1. E. R. Priest and T. Forbes, *Magnetic Reconnection: MHD Theory and Applications* (Cambridge University Press, Cambridge, England, 2000).
2. D. Biskamp, *Magnetic Reconnection in Plasmas*, Cambridge Monographs on Plasma Physics (Cambridge University Press, Cambridge, England, 2000).
3. M. Yamada, R. M. Kulsrud, and H. Ji, *Rev. Mod. Phys.* **82**, 603 (2010).
4. A. Bhattacharjee, *Annu. Rev. Astron. Astrophys.* **42**, 365 (2004).
5. M. Yamada *et al.*, *Phys. Plasmas* **1**, 3269 (1994).
6. N. A. Crocker *et al.*, *Phys. Rev. Lett.* **90**, 035003 (2003).
7. A. Bhattacharjee, Z. W. Ma, and X. Wang, *Phys. Plasmas* **8**, 1829 (2001).

8. B. V. Somov *et al.*, *Adv. Spaciers Res.* **32**, 1087 (2003).
9. M. Machida and R. Matsumoto, *Astrophys. J.* **585**, 429 (2003).
10. J. Goodman and D. Uzdensky, *Astrophys. J.* **688**, 555 (2008).
11. P. M. Nilson, L. Willingale, M. C. Kaluza, C. Kamperidis, S. Minardi, M. S. Wei, P. Fernandes, M. Notley, S. Bandyopadhyay, M. Sherlock, R. J. Kingham, M. Tatarakis, Z. Najmudin, W. Rozmus, R. G. Evans, M. G. Haines, A. E. Dangor, and K. Krushelnick, *Phys. Rev. Lett.* **97**, 255001 (2006).
12. C. K. Li, F. H. Séguin, J. A. Frenje, J. R. Rygg, R. D. Petrasso, R. P. J. Town, O. L. Landen, J. P. Knauer, and V. A. Smalyuk, *Phys. Rev. Lett.* **99**, 055001 (2007).
13. P. M. Nilson, L. Willingale, M. C. Kaluza, C. Kamperidis, S. Minardi, M. S. Wei, P. Fernandes, M. Noley, S. Bandyopadhyay, M. Sherlock, R. J. Kingham, M. Tatarakis, Z. Najmudin, W. Rozmus, R. G. Evans, M. G. Haines, A. E. Dangor, and K. Krushelnick, *Phys. Plasmas* **15**, 092701 (2008).
14. J. Zhong *et al.*, *Nat. Phys.* **6**, 984 (2010).
15. Q.-L. Dong *et al.*, *Phys. Rev. Lett.* **108**, 215001 (2012).
16. W. Fox, G. Fiksel, A. Bhattacharjee, P. Y. Chang, K. Germaschewski, S. X. Hu, and P. M. Nilson, *Phys. Rev. Lett.* **111**, 225002 (2013).
17. L. J. Waxer, D. N. Maywar, J. H. Kelly, T. J. Kessler, B. E. Kruschwitz, S. J. Loucks, R. L. McCrory, D. D. Meyerhofer, S. F. B. Morse, C. Stoeckl, and J. D. Zuegel, *Opt. Photonics News* **16**, 30 (2005).
18. O. V. Gotchev, J. P. Knauer, P. Y. Chang, N. W. Jang, M. J. Shoup III, D. D. Meyerhofer, and R. Betti, *Rev. Sci. Instrum.* **80**, 043504 (2009).
19. M. Borghesi *et al.*, *Plasma Phys. Control. Fusion* **43**, A267 (2001).
20. M. Borghesi *et al.*, *Phys. Rev. Lett.* **92**, 055003 (2004).
21. N. L. Kugland, J. S. Ross, P. Y. Chang, R. P. Drake, G. Fiksel, D. H. Froula, S. H. Glenzer, G. Gregori, M. Grosskopf, C. Huntington, M. Koenig, Y. Kuramitsu, C. Kuranz, M. C. Levy, E. Liang, D. Martinez, J. Meinecke, F. Miniati, T. Morita, A. Pelka, C. Plechaty, R. Presura, A. Ravasio, B. A. Remington, B. Reville, D. D. Ryutov, Y. Sakawa, A. Spitkovsky, H. Takabe, and H. S. Park, *Phys. Plasmas* **20**, 056313 (2013).
22. P. B. Radha, V. N. Goncharov, T. J. B. Collins, J. A. Delettrez, Y. Elbaz, V. Yu. Glebov, R. L. Keck, D. E. Keller, J. P. Knauer, J. A. Marozas, F. J. Marshall, P. W. McKenty, D. D. Meyerhofer, S. P. Regan, T. C. Sangster, D. Shvarts, S. Skupsky, Y. Srebro, R. P. J. Town, and C. Stoeckl, *Phys. Plasmas* **12**, 032702 (2005).
23. W. Fox, A. Bhattacharjee, and K. Germaschewski, *Phys. Rev. Lett.* **106**, 215003 (2011).
24. W. Fox, A. Bhattacharjee, and K. Germaschewski, *Phys. Plasmas* **19**, 056309 (2012).

Implosion Dynamics in Direct-Drive Experiments

Introduction

Direct-drive inertial confinement fusion uses laser beams to implode a spherical shell.¹ The laser energy is absorbed near the critical surface of the target, transferred through the conduction zone to the ablation region, and converted into the kinetic energy of the shell through the rocket effect. Near peak compression, a fraction of the kinetic energy of the imploding shell is converted to the internal energy of the fuel. When the ion temperature of the central region (hot spot) and the areal density of the compressed fuel are sufficiently large, a burn wave originating from the alpha particles produced by the fusion of deuterium (D) and tritium (T) will propagate through the confined fuel in the shell (ignition).

The OMEGA Laser System² is used to study the physics of direct-drive fusion and could demonstrate a hydrodynamically equivalent implosion that, when scaled to the available energy at the National Ignition Facility (NIF, 1.5 MJ), would produce ignition.^{3,4} One-dimensional (1-D) hydrodynamic simulations performed using the code *LILAC*,⁵ including nonlocal thermal conduction⁶ and cross-beam energy transfer (CBET) models,^{7,8} show that a hydrodynamically equivalent ignition design on OMEGA requires a final implosion velocity $V_{\text{imp}} > 3.5 \times 10^7$ cm/s, an areal density $\rho R > 300$ mg/cm², and a final hot-spot pressure $P_{\text{hs}} > 100$ Gbar (Ref. 9). To achieve these conditions with the current ablation pressure on OMEGA, a target design with an in-flight aspect ratio (IFAR) of 30 is required, where the IFAR is a measure of the hydrodynamic stability of the implosion¹⁰ given by the ratio of the radius to the thickness of the shell at a convergence ratio of 1.5 (Fig. 139.5).

An extensive set of experiments on OMEGA has been used to study the implosion performance in targets made of an outer layer of deuterated plastic (CD) and an inner layer of cryogenic DT ice surrounding DT gas.^{9,11} In these experiments, a threshold was characterized in the shell adiabat and IFAR space, where below the IFAR threshold, the areal density calculated in 1-D simulations is recovered in the experiments. Simulations showed that a hydro-equivalent ignition design on OMEGA is above the threshold (Fig. 139.5).

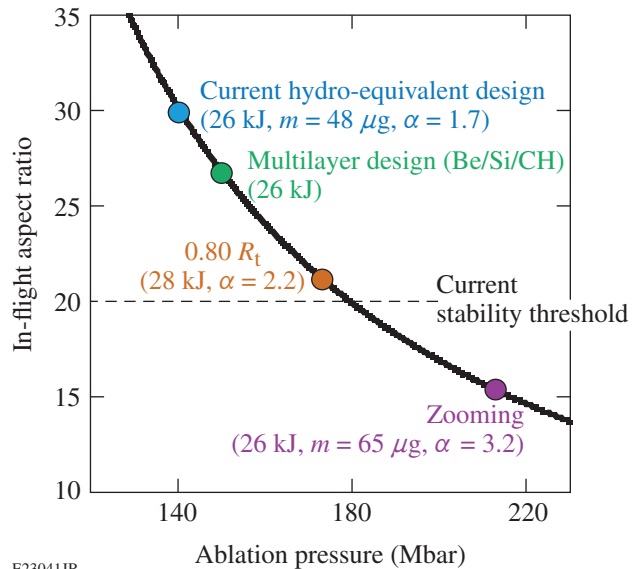


Figure 139.5

In-flight aspect ratio calculated at a convergence ratio of 1.5 as a function of ablation pressure (black curve) calculated at the end of the laser pulse for OMEGA direct-drive designs where the areal density ($\rho R = 300$ mg/cm²), implosion velocity ($V_{\text{imp}} = 3.7 \times 10^7$ cm/s), and hot-spot pressure ($P_{\text{hs}} = 180$ Mbar) are held constant. The designs used triple-picket laser pulses with a maximum intensity of 9×10^{14} W/cm². Simulations for the current cryogenic configuration (blue circle), a multilayer configuration (green circle), a configuration with a 20%-reduced beam size (orange circle), and a zooming configuration (purple circle) are shown. The current experimental stability threshold is indicated (dashed line).

Figure 139.5 shows a 1-D design curve generated by increasing the ablation pressure while maintaining a constant areal density ($\rho R = 300$ mg/cm²), implosion velocity ($V_{\text{imp}} = 3.7 \times 10^7$ cm/s), and hot-spot pressure ($P_{\text{hs}} = 180$ Gbar). Increasing the ablation pressure leads to a more-stable design (lower IFAR); when using higher ablation pressure, a thicker shell and larger adiabat can be used to maintain a constant implosion velocity, areal density, and hot-spot pressure. Figure 139.5 illustrates that increasing the ablation pressure from 140 Mbar (current design) to 180 Mbar is likely to achieve ignition hydro-equivalent implosions on OMEGA, assuming the current level of target nonuniformity seeds.

In this article, the transfer of laser energy to the kinetic energy of the shell (hydrodynamic efficiency) is studied for three different direct-drive-implosion experiments: cryogenic experiments,¹¹ ablator material experiments,¹² and reduced-beam-size experiments.¹³ Experimental measurements of both the laser absorption and the implosion velocity are compared with 1-D hydrodynamic simulations. In each case, excellent agreement is observed, indicating that the simulations accurately reproduce the hydrodynamic efficiency. Simulations showed that an $\sim 10\%$ increase in the ablation pressure was obtained for a Be ablator compared with a CH ablator. When the radius of the laser beams was reduced by 50%, nearly all of the ablation pressure lost to CBET was recovered and the ablation pressure was increased by $\sim 60\%$.

Results

The experiments discussed here were conducted on the OMEGA laser, where sixty 351-nm laser beams illuminated spherical shells. The hydrodynamic coupling was studied in cryogenic experiments, ablator material experiments, and reduced-beam-size experiments. In each case, the scattered-light power was measured to determine the absorption, while the shell trajectory, velocity, and neutron bang time were measured to quantify the transfer of the absorbed energy into the shell's kinetic energy. The experimental observables were compared with hydrodynamic simulations performed using the code *LILAC*,⁵ which includes nonlocal thermal transport⁶ and CBET⁸ models. The simulated trajectories were obtained by post-processing the 1-D hydrodynamic parameters with *Spect3D*¹⁴ to determine synthetic self-emission images. The simulations were used to determine the ablation pressure for the various cases and to assess the potential improvements in ignition hydro-equivalent OMEGA designs.

1. Cryogenic Experiments

The total laser energy in the cryogenic experiment was 26.6 kJ. The laser beams were smoothed by polarization smoothing (PS),¹⁵ smoothing by spectral dispersion (SSD),¹⁶ and distributed phase plates [SG4-DPP, fourth-order super-Gaussian with a 650- μm full width at half maximum (FWHM)].¹⁷ A laser pulse with three short pickets was used to set the implosion target on a moderate adiabat ($\alpha = 3.7$) (Ref. 18), followed by a 1.2-ns square pulse that accelerated a shell with an initial radius of 435 μm . The shell was made with a 7.4- μm CD ablator on top of a 52.2- μm -thick cryogenic DT ice layer.

The total unabsorbed laser energy was measured by five calorimeters located around the target chamber with an uncer-

tainty of 5%. The scattered-light power was measured at four locations by multiplexing the signal into a 1.5-m spectrometer with a high-dynamic-range streak camera. The system had a 100-ps (FWHM) temporal resolution.

Figure 139.6 compares the measured and simulated time-resolved unabsorbed laser light. The excellent agreement between them indicates that the CBET model accurately reproduces the laser power absorbed in the plasma; the simulation also shows that nearly half of the scattered light is a result of CBET. The small discrepancy observed around 1.6 ns could be caused by an error in the CBET calculation during the rise of the laser pulse, where the hydrodynamic conditions evolve rapidly.

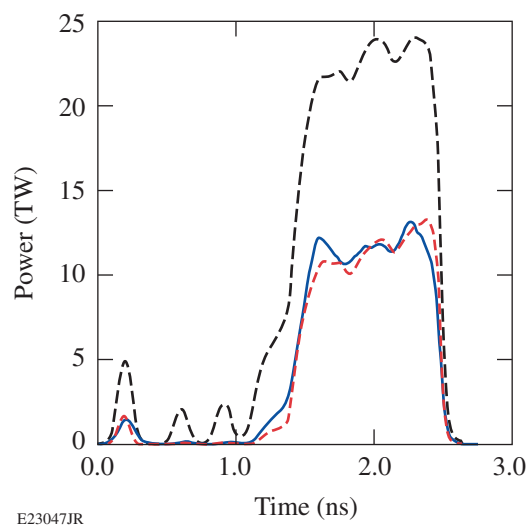
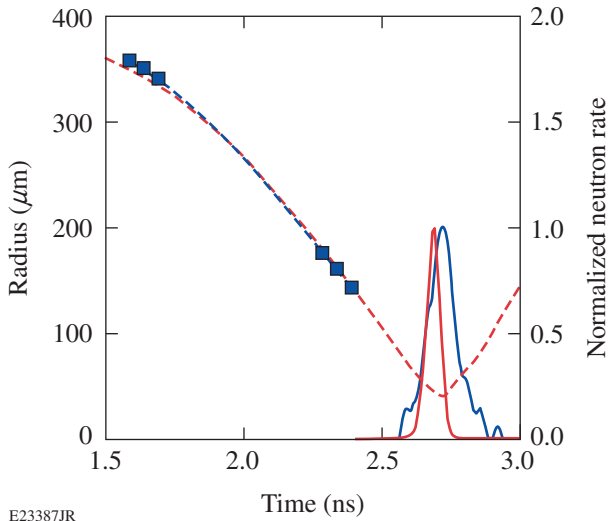


Figure 139.6 Comparison of the calculated (red dashed line) and measured (blue solid line) scattered-light power. The laser pulse is plotted (black dashed line).

Figure 139.7 shows excellent agreement between the measured and simulated shell trajectories. These results suggest that the nonlocal transport model accurately calculates this coupling since the transfer of the absorbed laser energy to the shell motion depends primarily on the thermal transport. A small discrepancy was obtained in the ablation-front position at early times when the simulated radius was $\sim 10 \mu\text{m}$ smaller than the measured radius. The early discrepancy may be explained by the small difference in laser absorption measured during the rise of the main pulse.

The agreement observed between the simulated and measured shell trajectory is consistent with the good agreement observed in the time of neutron production (Fig. 139.7). The total

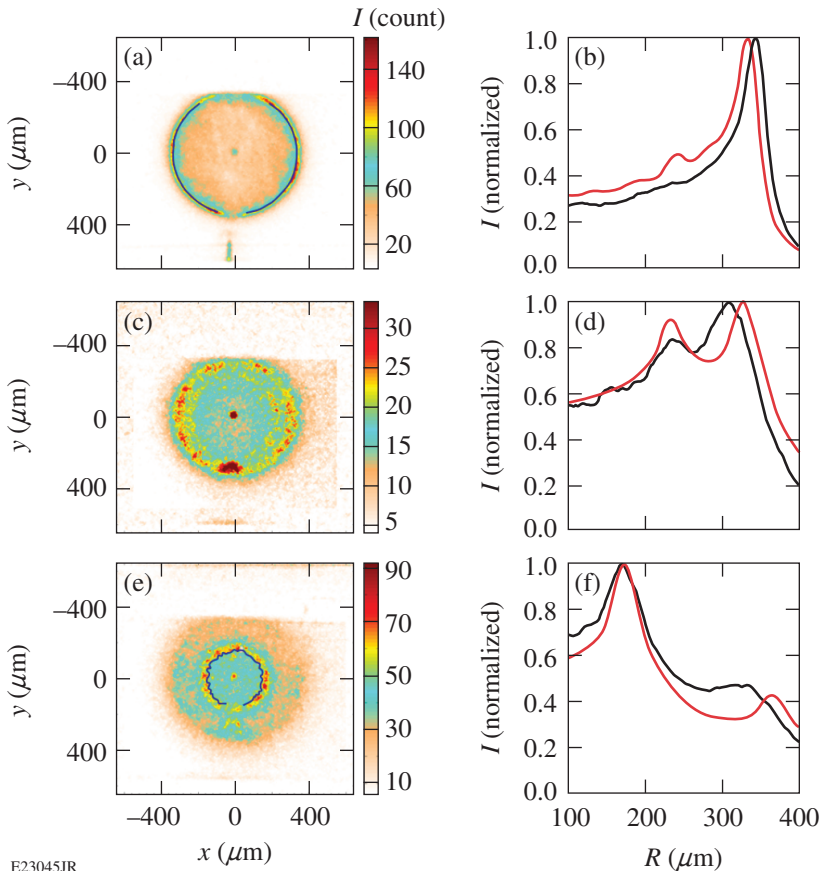


E23387JR

Figure 139.7 Comparison of the calculated (red dashed line) and measured (squares) shell trajectory and calculated (red solid line) and measured (blue solid line) normalized neutron-production rates obtained for the current cryogenic design. The third-order polynomial fit to the experimental data is shown (blue dashed line).

neutron production was $5\times$ lower in the experiment than in simulation (the neutron production is normalized in Fig. 139.7), likely related to shell perturbations that compromise the implosion.

The self-emission shadowgraphy technique¹⁹ was used to determine the shell trajectories. The soft x rays emitted by the imploding target were integrated over 40 ps and imaged with an array of pinholes onto a four-strip fast x-ray framing camera (XRFC).²⁰ The distinct peak in the emission-profile images resulted from the high density and temperature at the ablation surface and the large integration distance for the emission that reaches the XRFC (limb effect). In the cryogenic target experiments,⁹ the primarily DT shell is optically thin to the CD emission at early times [Figs. 139.8(a) and 139.8(b)] and the ablation front is determined from the peak of the emission.²¹ At late times [Figs. 139.8(e) and 139.8(f)], the shell is optically thick to the DT emission and the ablation front is determined from the position of the inner gradient. During the transition time when the CD is being ablated [Figs. 139.8(c) and 139.8(d)], the CD emission peak separates from the ablation surface and cannot be used to determine the ablation-front position. During this time, the ablation-front trajectory is inferred by fitting the



E23045JR

Figure 139.8 [(a),(c),(e)] Self-emission x-ray images from a cryogenic experiment; [(b),(d),(f)] comparison of the lineouts averaged over the entire experimental image (black line) with lineouts calculated from the simulations (red line) at [(a),(b)] $t = 1680$ ps, [(c),(d)] $t = 2145$ ps, and [(e),(f)] $t = 2325$ ps.

ablation-front position measured at early and late times with a third-order polynomial. A standard deviation of the peak (inner gradient) location around the image of $\sigma_{\text{abl}} = 2 \mu\text{m}$ ($\sigma_{\text{abl}} = 5 \mu\text{m}$) is obtained. These positions are averaged as $N = 2\pi/\theta_{\text{av}} \sim 60$ independent measurements (where each lineout is averaged over $\theta_{\text{av}} = 5^\circ$) to give a resulting accuracy for the averaged radius of $\sigma_{\text{abl}}/\sqrt{N} < 1 \mu\text{m}$ (Ref. 21).

The shell radii measured on two consecutive XRFC strips, 200 ps apart, were used to calculate time-averaged shell velocities. The relative timing between the XRFC strips was known to within 5 ps and the absolute timing to the laser pulse to within 30 ps (Ref. 12). The accuracy in the velocity (dV/V) was $\sim 4\%$ for a shell velocity of 200 km/s, given by

$$\frac{dV}{V} = \left[\frac{d(\Delta R)}{\Delta R} + \frac{d(\Delta t)}{\Delta t} \right]^{1/2},$$

where the error in the radius was $d(\Delta R)/\Delta R = 0.7/40 \mu\text{m} = 1.8\%$ and the error in the timing was $d(\Delta t)/\Delta t = 7/200 \text{ ps} = 3.5\%$.

2. Ablator Material Experiments

In the ablator experiments, the overlapped intensity was varied by changing the total energy on target from 18.5 kJ (low intensity, $I = 4.5 \times 10^{14} \text{ W/cm}^2$) to 23 kJ (high intensity, $I = 7.2 \times 10^{14} \text{ W/cm}^2$). The laser beams were smoothed by PS, SSD, and SG4-DPP. Three 100-ps-long pickets were used to set the target implosion onto a low adiabat followed by a 1.2-ns (high-intensity) and 1.6-ns (low-intensity) square pulse that drove the target to its final velocity. The three ablators had mass densities of 1.03 g/cm^3 (CH), 3.35 g/cm^3 (C), and 1.83 g/cm^3 (Be). Their thicknesses were varied to maintain the initial total ablator mass to be equivalent to a $27\text{-}\mu\text{m}$ -thick CH shell. The outer radius at low energy and at high energy was $440 \mu\text{m}$ and $445 \mu\text{m}$, respectively, and the total mass was $62 \pm 1 \mu\text{g}$ and $64 \pm 2 \mu\text{g}$, respectively.

Figure 139.9 shows the simulated and measured shell trajectories and scattered powers for three different ablator materials: beryllium ($\text{Be}, \langle A \rangle / \langle Z \rangle = 2.25$), high-density carbon ($\text{C}, \langle A \rangle / \langle Z \rangle = 2$), and glow-discharge polymer ($\text{CH}, \langle A \rangle / \langle Z \rangle = 1.85$). In C and Be ablators, multiple experi-

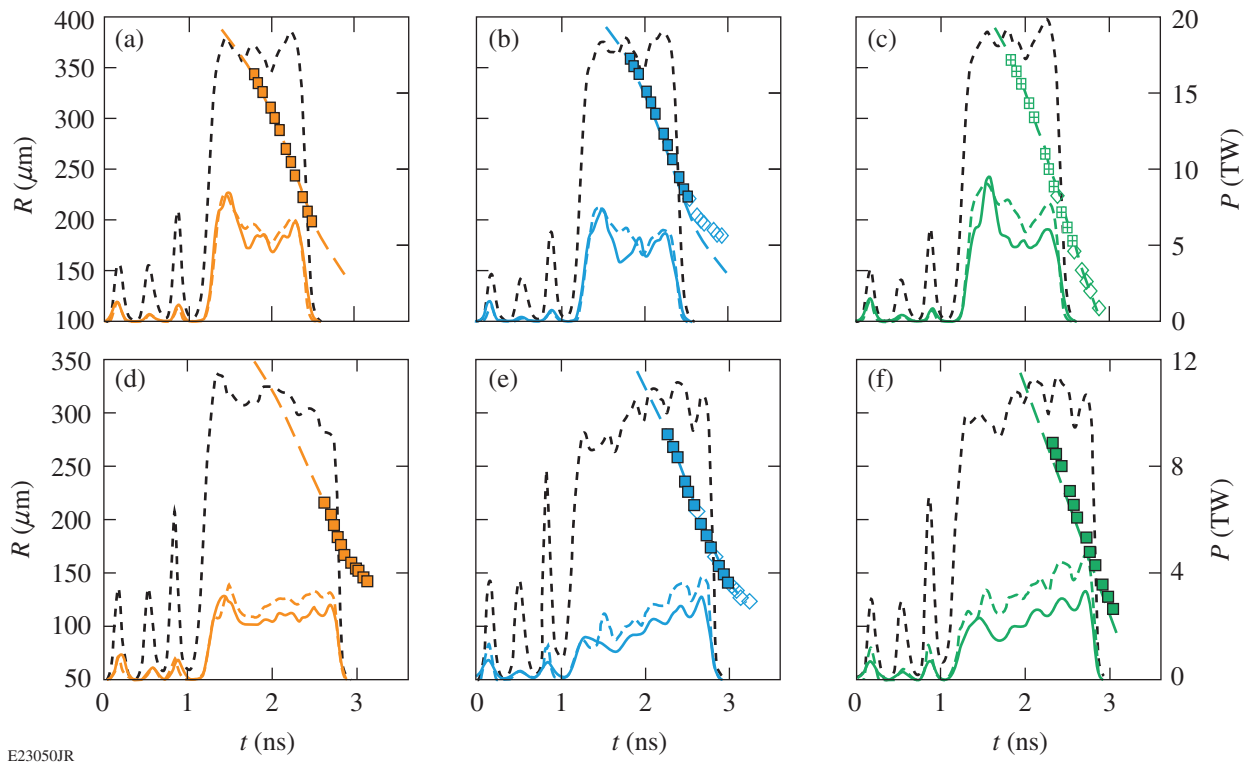


Figure 139.9

Comparison of the calculated (dashed lines) and measured (symbols) shell trajectories (the different symbols represent different shots) and of the calculated (dashed lines) and measured (solid line) scattered-light power. The results are presented for [(a),(d)] CH, [(b),(e)] C, and [(c),(f)] Be ablators at high and low laser power (black dashed lines, right axis).

ments were performed to demonstrate reproducibility of these results. The ability of the simulations to accurately reproduce both the measured trajectories and scattered powers suggests that the hydrodynamic efficiency is well modeled with *LILAC* for all three ablators at both high and low intensities.

Figures 139.10(a) and 139.10(b) show that the velocity of the shell at the end of the laser pulse is increased by 20% in the Be ablators at both low and high intensities compared to the CH ablators. Since the initial target mass was held constant, a higher velocity suggests a larger kinetic energy of the shell, but this is slightly reduced by a smaller final mass because of a higher mass-ablation rate. For the three ablators, the total laser absorption was similar at low intensity (~80%) and high intensity (~70%). This indicates that the increased velocity in Be ablators results from the transfer of the absorbed laser energy to the kinetic energy of the shell. Increasing $\langle A \rangle / \langle Z \rangle$ improves the coupling of the absorbed energy to the kinetic energy of the shell by increasing the mass density near the critical density (i.e., where the laser energy is absorbed).²²

Figure 139.10(c) compares the ablation pressure calculated during the implosion at a similar convergence ratio of 1.5 for the three ablators at low and high laser intensities. An ~10% increase is observed for the Be ablator compared to the C and CH ablators as a result of the increased $\langle A \rangle / \langle Z \rangle$. Simulations suggest that hydro-equivalent ignition designs for OMEGA that use a Be layer can increase the ablation pressure by ~7% compared with the standard CD/DT design, allowing the IFAR to be reduced to 27 (Fig. 139.5) (Ref. 9).

3. Reduced-Beam-Size Experiments

The reduced-beam-size experiments used laser beams smoothed by PS and DPP. Fifty-seven phase plates designed to produce elliptical spots were oriented with their minor axes aligned in the direction of the wedge dispersion of the PS crystal, producing a nearly round $R_b = 215\text{-}\mu\text{m}$ (95% encircled energy) laser spot at best focus. The ellipticities of these laser spots were measured to be less than 15%. Three round DPP's with a best-focus radius of $R_b = 210\ \mu\text{m}$ were used to complete the set. The radii of the laser spots were varied by defocusing the laser beams. A triple-picket laser pulse shape with a 1.6-ns square drive pulse and 18 kJ of total energy was used to set the shell on a low adiabat ($\alpha \approx 3$). The outer radius of the CH capsule was $R_t = 430\ \mu\text{m}$, with a wall thickness of $27\ \mu\text{m}$.

Figure 139.11(a) shows the measured shell trajectories when the radius of each laser-beam spot was scaled. The smaller beam spots resulted in a higher ablation pressure, which accelerated the target significantly faster. Even for a moderate reduction in beam size ($R_b/R_t = 1$ to $R_b/R_t = 0.9$), a significant increase in velocity was observed: 186 km/s to 194 km/s (~5% increase). Good agreement between the simulated and measured shell trajectories and scattered-light powers was observed for all focal-spot radii. The improved coupling was a result of (1) more-normal rays that deposit their energy closer to the ablation surface and (2) the reduction of CBET.¹³

Figure 139.11(b) shows the ablation pressure calculated from the simulations at a convergence ratio of 1.5. A 50% increase in

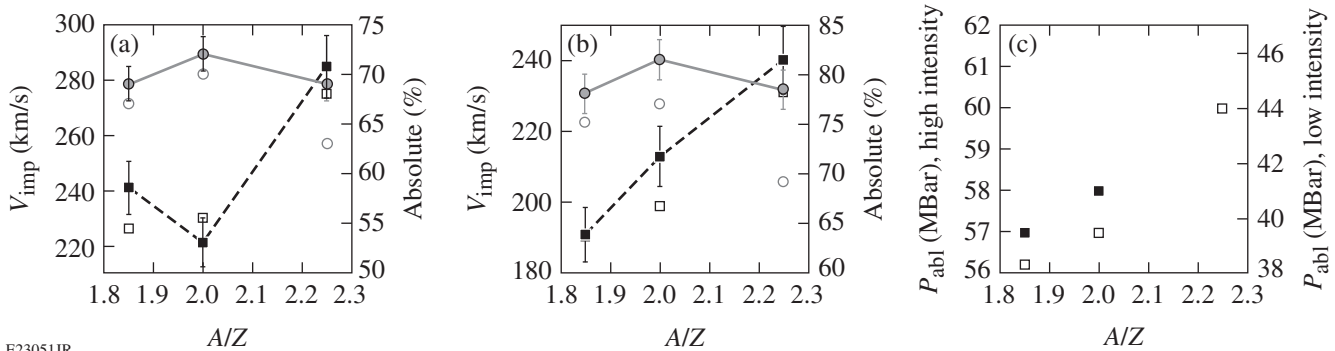
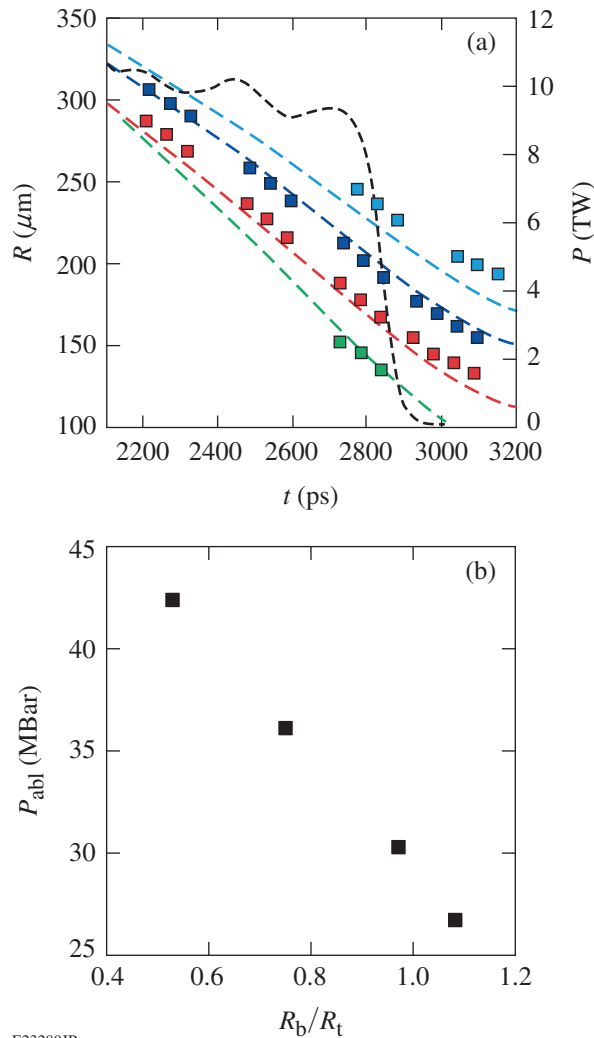


Figure 139.10

Comparison of the shell velocities measured at the end of the laser pulse (solid squares) and the total laser absorption determined from the measured scattered light (solid circles) for CH ($\langle A \rangle / \langle Z \rangle = 1.85$), C ($\langle A \rangle / \langle Z \rangle = 2$), and Be ($\langle A \rangle / \langle Z \rangle = 2.25$) ablators at (a) high and (b) low laser intensities; the corresponding calculated values are shown as open symbols. (c) Comparison of the simulated ablation pressure at a convergence ratio of 1.5 for CH ($\langle A \rangle / \langle Z \rangle = 1.85$), C ($\langle A \rangle / \langle Z \rangle = 2$), and Be ($\langle A \rangle / \langle Z \rangle = 2.25$) ablators at low (open squares) and high (solid squares) laser intensities.



E23280JR

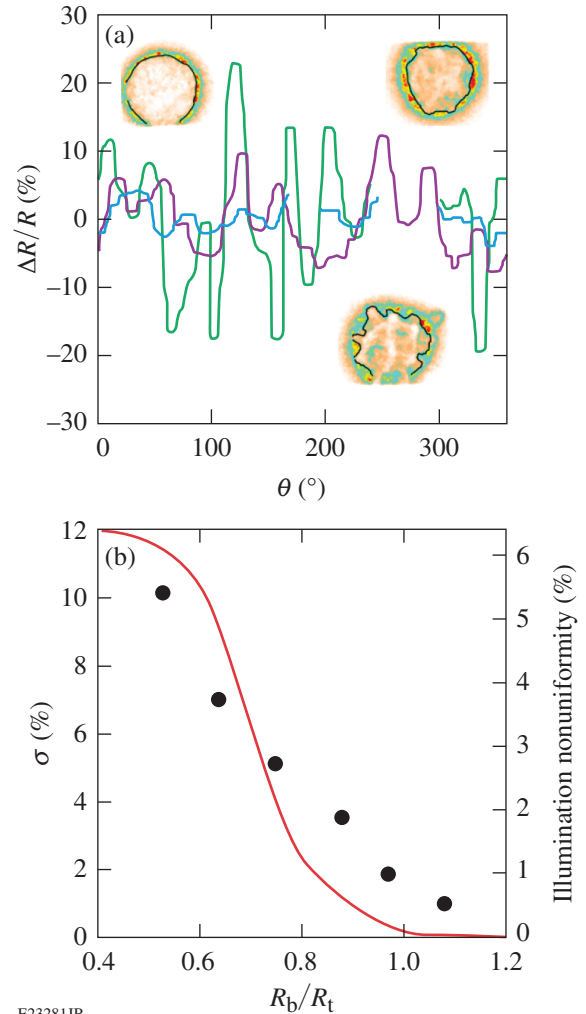
Figure 139.11

(a) Comparison of the measured (squares) and simulated (dashed lines) shell trajectories for $R_b/R_t = 0.5$ (green), $R_b/R_t = 0.9$ (red), $R_b/R_t = 1$ (blue), and $R_b/R_t = 1.1$ (light blue). A similar laser pulse was measured for each shot (black line, right axis). (b) The ablation pressure calculated at a convergence ratio of 1.5.

the ablation pressure was calculated when R_b/R_t was varied from 1.1 to 0.5.

Figure 139.12(a) shows the standard deviation in the variation of the position of the inner gradient around the image for various laser-beam diameters. When the laser-beam size is reduced, the standard deviation of the low-mode nonuniformities measured at the ablation surface increases from 1% to more than 10%. The structure of the perturbations grows at positions consistent with regions where the illumination is lower. The standard deviation of the low-mode perturbations measured from the XRFC images is compared to the standard

deviation of the low-mode nonuniformity of the absorbed laser power averaged over the entire laser pulse for different R_b/R_t [Fig. 139.12(b)]. When the size of the focal spot is reduced, the illumination nonuniformity increases and the shell perturbations compromise the target compression. Simulations suggest that the laser-beam diameters can be reduced to 80% of the target diameter before significant degradation in yield is observed.⁸ In this case, simulations indicate that the ablation pressure was increased by 24%, allowing for a hydro-equivalent



E23281JR

Figure 139.12

(a) Comparison of the low-mode shell perturbations measured for $R_b/R_t = 0.5$ (green line, bottom inset), $R_b/R_t = 0.75$ (purple line, top right inset), and $R_b/R_t = 1$ (blue line, top left inset) at an averaged radius of $175 \mu\text{m}$. (b) Comparison of the standard deviation of the shell perturbation obtained in experiments (left axis) with the standard deviation of the simulated nonuniformity in the absorbed laser power averaged over the entire laser pulse (red line, right axis).

ignition design on OMEGA with an IFAR of 22—close to the current stability threshold (Fig. 139.5).

To further reduce the beam size, a two-stage zooming scheme has been proposed where large beams are used during the pickets and small beams are used during the main drive when the conduction zone is large enough to smooth low-mode laser nonuniformity.^{23,24} By using $R_b/R_t = 0.6$ during the main drive, nearly all of the ablation pressure lost to CBET is recovered and a hydro-equivalent ignition design is well below the current stability threshold (Fig. 139.5).

Conclusions

Demonstrating hydro-equivalent ignition at the Omega Laser Facility is a first step toward direct-drive ignition on the NIF. Achieving hydro-equivalent ignition on OMEGA requires an implosion velocity $>3.5 \times 10^7$ cm/s, an areal density >300 mg/cm², and a hot-spot pressure above 100 Gbar. Currently, the best-performing implosions, which are driven to ignition-relevant velocities, do not reach hydro-equivalent areal densities, limiting the peak hot-spot pressure to ~ 40 Gbar (Ref. 9). One approach to recovering the hydro-equivalent areal density is to decrease the IFAR by using thicker shells. To drive the thicker shells to the relevant velocities, the hydrodynamic efficiency must be improved.

In this article, the hydrodynamic efficiency has been studied in three different direct-drive experiments. The coupling of the laser energy to the plasma (absorption) was determined by measuring the scattered-light power. The plasma energy transferred to the kinetic energy of the shell was studied by measuring the shell trajectory, the shell velocity, and the neutron burn history. These experimental observables were compared with 1-D hydrodynamic simulations (conducted by the code *LILAC*) that include CBET and nonlocal thermal-transport models. In each case, excellent agreement was observed, suggesting that the code was able to reproduce the hydrodynamic parameters of the imploding shell. For Be targets, the ablation pressure of the laser was shown to increase by $\sim 10\%$ compared with the C and standard CH ablaters. When the spot size of the laser was reduced by $\sim 50\%$, the ablation pressure was shown to increase by a factor of 1.6, but the increased illumination non-uniformity compromised the integrated target performance. In future experiments, three new designs will be tested: multilayer ablaters,⁹ beam diameters that are 80% of the target diameter, and two-stage zooming. Simulations indicate that the ablation pressure in hydro-equivalent designs will be increased by 7% for the first case, 24% for the second case, and 50% for the third case.

ACKNOWLEDGMENT

This material is based upon work supported by the Department of Energy National Nuclear Security Administration under Award Number DE-NA0001944, the University of Rochester, and the New York State Energy Research and Development Authority. The support of DOE does not constitute an endorsement by DOE of the views expressed in this article.

REFERENCES

1. J. Nuckolls *et al.*, *Nature* **239**, 139 (1972).
2. T. R. Boehly, D. L. Brown, R. S. Craxton, R. L. Keck, J. P. Knauer, J. H. Kelly, T. J. Kessler, S. A. Kumpan, S. J. Loucks, S. A. Letzring, F. J. Marshall, R. L. McCrory, S. F. B. Morse, W. Seka, J. M. Soures, and C. P. Verdon, *Opt. Commun.* **133**, 495 (1997).
3. J. Paisner *et al.*, *Laser Focus World* **30**, 75 (1994).
4. R. Nora, R. Betti, K. S. Anderson, A. Shvydky, A. Bose, K. M. Woo, A. R. Christopherson, J. A. Marozas, T. J. B. Collins, P. B. Radha, S. X. Hu, R. Epstein, F. J. Marshall, R. L. McCrory, T. C. Sangster, and D. D. Meyerhofer, *Phys. Plasmas* **21**, 056316 (2014).
5. J. Delettrez, *Can. J. Phys.* **64**, 932 (1986).
6. V. N. Goncharov, T. C. Sangster, P. B. Radha, R. Betti, T. R. Boehly, T. J. B. Collins, R. S. Craxton, J. A. Delettrez, R. Epstein, V. Yu. Glebov, S. X. Hu, I. V. Igumenshchev, J. P. Knauer, S. J. Loucks, J. A. Marozas, F. J. Marshall, R. L. McCrory, P. W. McKenty, D. D. Meyerhofer, S. P. Regan, W. Seka, S. Skupsky, V. A. Smalyuk, J. M. Soures, C. Stoeckl, D. Shvarts, J. A. Frenje, R. D. Petrasso, C. K. Li, F. Séguin, W. Manheimer, and D. G. Colombant, *Phys. Plasmas* **15**, 056310 (2008).
7. P. Michel, L. Divol, E. A. Williams, S. Weber, C. A. Thomas, D. A. Callahan, S. W. Haan, J. D. Salmonson, S. Dixit, D. E. Hinkel, M. J. Edwards, B. J. MacGowan, J. D. Lindl, S. H. Glenzer, and L. J. Suter, *Phys. Rev. Lett.* **102**, 025004 (2009).
8. I. V. Igumenshchev, W. Seka, D. H. Edgell, D. T. Michel, D. H. Froula, V. N. Goncharov, R. S. Craxton, L. Divol, R. Epstein, R. Follett, J. H. Kelly, T. Z. Kosc, A. V. Maximov, R. L. McCrory, D. D. Meyerhofer, P. Michel, J. F. Myatt, T. C. Sangster, A. Shvydky, S. Skupsky, and C. Stoeckl, *Phys. Plasmas* **19**, 056314 (2012).
9. V. N. Goncharov, T. C. Sangster, R. Betti, T. R. Boehly, M. J. Bonino, T. J. B. Collins, R. S. Craxton, J. A. Delettrez, D. H. Edgell, R. Epstein, R. K. Follett, C. J. Forrest, D. H. Froula, V. Yu. Glebov, D. R. Harding, R. J. Henchen, S. X. Hu, I. V. Igumenshchev, R. Janezic, J. H. Kelly, T. J. Kessler, T. Z. Kosc, S. J. Loucks, J. A. Marozas, F. J. Marshall, A. V. Maximov, R. L. McCrory, P. W. McKenty, D. D. Meyerhofer, D. T. Michel, J. F. Myatt, R. Nora, P. B. Radha, S. P. Regan, W. Seka, W. T. Shmayda, R. W. Short, A. Shvydky, S. Skupsky, C. Stoeckl, B. Yaakobi, J. A. Frenje, M. Gatu-Johnson, R. D. Petrasso, and D. T. Casey, *Phys. Plasmas* **21**, 056315 (2014).
10. P. B. Radha, C. Stoeckl, V. N. Goncharov, J. A. Delettrez, D. H. Edgell, J. A. Frenje, I. V. Igumenshchev, J. P. Knauer, J. A. Marozas, R. L. McCrory, D. D. Meyerhofer, R. D. Petrasso, S. P. Regan, T. C. Sangster, W. Seka, and S. Skupsky, *Phys. Plasmas* **18**, 012705 (2011).
11. T. C. Sangster, V. N. Goncharov, R. Betti, P. B. Radha, T. R. Boehly, D. T. Casey, T. J. B. Collins, R. S. Craxton, J. A. Delettrez, D. H.

- Edgell, R. Epstein, C. J. Forrest, J. A. Frenje, D. H. Froula, M. Gatu-Johnson, V. Yu. Glebov, D. R. Harding, M. Hohenberger, S. X. Hu, I. V. Igumenshchev, R. Janezic, J. H. Kelly, T. J. Kessler, C. Kingsley, T. Z. Kosc, J. P. Knauer, S. J. Loucks, J. A. Marozas, F. J. Marshall, A. V. Maximov, R. L. McCrory, P. W. McKenty, D. D. Meyerhofer, D. T. Michel, J. F. Myatt, R. D. Petrasso, S. P. Regan, W. Seka, W. T. Shmayda, R. W. Short, A. Shvydky, S. Skupsky, J. M. Soures, C. Stoeckl, W. Theobald, V. Versteeg, B. Yaakobi, and J. D. Zuegel, *Phys. Plasmas* **20**, 056317 (2013).
12. D. T. Michel, V. N. Goncharov, I. V. Igumenshchev, R. Epstein, and D. H. Froula, *Phys. Rev. Lett.* **111**, 245005 (2013).
 13. D. H. Froula, I. V. Igumenshchev, D. T. Michel, D. H. Edgell, R. Follett, V. Yu. Glebov, V. N. Goncharov, J. Kwiatkowski, F. J. Marshall, P. B. Radha, W. Seka, C. Sorce, S. Stagnitto, C. Stoeckl, and T. C. Sangster, *Phys. Rev. Lett.* **108**, 125003 (2012).
 14. J. J. MacFarlane *et al.*, *High Energy Density Phys.* **3**, 181 (2007).
 15. T. R. Boehly, V. A. Smalyuk, D. D. Meyerhofer, J. P. Knauer, D. K. Bradley, R. S. Craxton, M. J. Guardalben, S. Skupsky, and T. J. Kessler, *J. Appl. Phys.* **85**, 3444 (1999).
 16. S. Skupsky, R. W. Short, T. Kessler, R. S. Craxton, S. Letzring, and J. M. Soures, *J. Appl. Phys.* **66**, 3456 (1989).
 17. T. J. Kessler, Y. Lin, J. J. Armstrong, and B. Velazquez, in *Laser Coherence Control: Technology and Applications*, edited by H. T. Powell and T. J. Kessler (SPIE, Bellingham, WA, 1993), Vol. 1870, pp. 95–104.
 18. V. N. Goncharov, T. C. Sangster, T. R. Boehly, S. X. Hu, I. V. Igumenshchev, F. J. Marshall, R. L. McCrory, D. D. Meyerhofer, P. B. Radha, W. Seka, S. Skupsky, C. Stoeckl, D. T. Casey, J. A. Frenje, and R. D. Petrasso, *Phys. Rev. Lett.* **104**, 165001 (2010).
 19. D. T. Michel, C. Sorce, R. Epstein, N. Whiting, I. V. Igumenshchev, R. Jungquist, and D. H. Froula, *Rev. Sci. Instrum.* **83**, 10E530 (2012).
 20. D. K. Bradley *et al.*, *Rev. Sci. Instrum.* **66**, 716 (1995).
 21. A. K. Davis, D. T. Michel, S. X. Hu, R. S. Craxton, R. Epstein, V. N. Goncharov, I. V. Igumenshchev, T. C. Sangster, and D. H. Froula, *Rev. Sci. Instrum.* **85**, 11D616 (2014).
 22. W. M. Manheimer, D. G. Colombant, and J. H. Gardner, *Phys. Fluids* **25**, 1644 (1982).
 23. D. H. Froula, T. J. Kessler, I. V. Igumenshchev, R. Betti, V. N. Goncharov, H. Huang, S. X. Hu, E. Hill, J. H. Kelly, D. D. Meyerhofer, A. Shvydky, and J. D. Zuegel, *Phys. Plasmas* **20**, 082704 (2013).
 24. I. V. Igumenshchev, D. H. Froula, D. H. Edgell, V. N. Goncharov, T. J. Kessler, F. J. Marshall, R. L. McCrory, P. W. McKenty, D. D. Meyerhofer, D. T. Michel, T. C. Sangster, W. Seka, and S. Skupsky, *Phys. Rev. Lett.* **110**, 145001 (2013).

X-Ray Continuum as a Measure of Pressure and Fuel–Shell Mix in Compressed Isobaric Hydrogen Implosion Cores

Introduction

Measurements of continuum x-ray emission from the central hot spots of inertial confinement fusion (ICF)¹ implosions at stagnation can be directly related to hot-spot conditions using the relatively simple dependence of continuum spectral emission rates on temperature and density or pressure. Since thermonuclear ignition and high energy gain are the goals of ICF,^{2,3} one would naturally look to neutron yield as the primary measure of implosion performance. The benchmarks of progress toward ignition, or toward implosion performance that scales to ignition with higher drive energy,⁴ however, are specified in terms of core conditions at peak compression.⁵ Short of ignition, neutron yield and x-ray emission measurements can be used in similar ways to infer hot-spot conditions. The current strategy is to achieve high-temperature central hot spots within fuel shells compressed at low entropy to high areal densities. A key measure of near-ignition performance in ICF, through the Lawson criterion,⁶ is the hot-spot pressure.⁷ Consequently, a direct relationship between the hot-spot pressure and the measured hot-spot x-ray continuum emissivity, based as little as possible on prior assumptions about hot-spot temperature profiles, normalization to simulations, etc., would be very important.

At a sufficiently high spectral energy, typically $h\nu > 3$ keV for cryogenic implosions on the 60-beam OMEGA Laser System,⁸ the imploded cores are optically thin and the x-ray measurements are a direct measure of the emissivity, free of absorption and other transport effects. With instrument spectral responses narrowed to energies matched to the anticipated temperature of the hot spot, as will be described below, the free-free (FF) emissivity⁹ of hot-spot hydrogen scales as the square of the hot-spot pressure and is nearly independent of the temperature. The simple pressure dependence of the emissivity, the isobaric state of the hot spot at stagnation,^{10,11} and the known temperature–density scaling of the neutron-production rate explain a simple scaling behavior of the x-ray yield as a constant power of the neutron yield over a factor-of-10 range in neutron yield in an ensemble of similar targets imploded with a variety of laser pulses over a broad range of shell isentropes.

This is a quantitative prediction based on our understanding of isobaric hot spots that has been confirmed with measured x-ray and neutron yields. In an unstable implosion, a trace (above ~ 10 ng) amount of shell material mixed into the hot spot can increase the x-ray emission measurably because of the much higher emissivity per atom of carbon, without affecting the neutron yield significantly. Using the x-ray yield expected from the neutron-yield scaling as a point of reference, the excess x-ray emission and the known FF and free-bound (FB) emissivity⁹ of carbon provide a measure of this “fuel–shell” mix mass. This mix-mass estimate is similar in some respects to recent measurements of mix mass in National Ignition Facility (NIF)¹² implosions based on the ratio of the x-ray and neutron yields.¹³

The pressure profile within an imploded core at the time of peak emission can be obtained from the emissivity profile of the object, and the emissivity profile can be obtained from its projection recorded on an image plane by an imaging device. The fundamental quantity of radiation is the specific intensity $I(\vec{x}, \hat{\Omega}, \nu)$, which is the amount of radiation energy per unit of time arriving at position \vec{x} in space, per unit of area within an infinitesimal area element at this point, oriented normal to the propagation direction given by the unit normal vector $\hat{\Omega}$, per unit spectral range within an infinitesimal interval of frequency, centered at the frequency ν , and traveling within an infinitesimal cone of solid angle, per steradian, centered on the direction $\hat{\Omega}$. We will write it as I_ν for short. The time-independent equation of transfer governing the change dI_ν in the specific intensity of radiation propagating an infinitesimal distance ds along the direction $\hat{\Omega}$ is

$$\frac{dI_\nu}{ds} = \frac{\epsilon_\nu}{4\pi} - \kappa_\nu I_\nu, \quad (1)$$

where the interaction of radiation and matter is described entirely in terms of the plasma emissivity ϵ_ν and the opacity κ_ν of the matter.¹⁴ The emissivity specifies the energy per unit of time that is emitted per unit of volume isotropically into all directions within an infinitesimal interval of frequency centered at the frequency ν . The opacity is the fraction of the specific intensity absorbed per unit distance of propagation.

We assume that all radiation of interest propagates at the speed of light c without refraction or dispersion and that any photon scattering involving a change of frequency or direction is accounted for effectively by a combination of absorption and emission included in ϵ_ν together with κ_ν .

In the optically thin limit, there is only emission and no attenuation, and the solution to the equation of transfer is the path integral

$$I_\nu(\vec{x}) = \int_{-\infty}^{\vec{x}} \frac{\epsilon_\nu(\vec{r})}{4\pi} d\vec{s}. \quad (2)$$

The integration variable \vec{s} is a point along a straight-line photon path arriving at a point \vec{x} on the image plane and \vec{r} is the position of that point on the path relative to an arbitrary fixed point of reference within the emitting object. The integration path is a straight line arriving at the observer position from arbitrarily far away, indicated symbolically as “ $-\infty$,” but only points along the path within the emission source contribute to the integral. The imaging device selects from the set of all paths $\hat{\Omega}$ ending at any one \vec{x} so that the image represents a useful projection of the emissivity profile. For the purposes of this discussion, we assume that the imaging device records an orthographic projection of the source, such that the direction $\hat{\Omega}$ of all paths is the same. In spherical geometry, Eq. (2) gives the specific intensity as an Abel transform¹⁵ of the emissivity profile. For example, a spherically symmetric emissivity distribution $\epsilon_\nu(r)$ produces the specific intensity

$$I_\nu(x) = \frac{1}{2\pi} \int_x^\infty \frac{\epsilon_\nu(r)r}{\sqrt{r^2 - x^2}} dr, \quad (3)$$

and the emissivity distribution can be recovered from the inverse Abel transform of the imaged intensity,

$$\epsilon_\nu(r) = -4 \int_r^\infty \frac{dI_\nu(x)}{dx} \frac{dx}{\sqrt{x^2 - r^2}}. \quad (4)$$

The point $x = 0$ on the image plane is the projection of the center of the radial emissivity distribution at $r = 0$, and we assume that all geometrical and optical effects of an actual camera, such as magnification, etc., have already been taken into account.

If the emissivity is a known function of pressure alone, the radial pressure profile of a spherical hot spot can be inferred

from the emissivity profile extracted from the imaged intensity using Eq. (4). If, in addition, the hot spot is isobaric, the pressure is constant throughout the hot spot out to its outer radius R and the emissivity will be constant within this radius; we find using Eq. (4) that the intensity profile of its image is elliptical:

$$I_\nu(x) = \frac{\epsilon_\nu(0)}{2\pi} \sqrt{R^2 - x^2}. \quad (5)$$

The integral of the specific intensity given by Eq. (2) over the image plane gives the total emitted power per unit solid angle at the image plane:

$$\int I_\nu(\vec{x}) d^2\vec{x} = \iint_{-\infty}^{\infty} \frac{\epsilon_\nu(\vec{r})}{4\pi} d\vec{s} d^2\vec{x} = \frac{1}{4\pi} \int \epsilon_\nu(\vec{r}) d^3\vec{r}. \quad (6)$$

Assuming the hot spot radiates isotropically, the total spectral power is obtained by applying a factor of 4π . In the case of the flat emissivity profile of an isobaric core, this gives

$$P_\nu = \frac{4\pi}{3} R^3 \epsilon_\nu(0). \quad (7)$$

The isobaric sphere, then, possesses a remarkable simplicity: All quantities pertaining to emission can be described in terms of a single radius and a single emissivity that depends on one parameter—the pressure. In the following sections, departures of the emissivity from pure pressure dependence, hot spots that are not strictly isobaric, “fuel-shell mix,” and other complications will be considered.

Pressure Dependence of X-Ray Emission from Isobaric Hot Spots

The emissivity of an imploded hydrogen hot spot of a cryogenic implosion is almost entirely the result of FF emission from hydrogen. The expression for the FF emissivity of a hot plasma of fully stripped ions at photon frequency ν , temperature T , electron and ion densities n_e and n_i , respectively, and average nuclear charge squared $\langle Z^2 \rangle$ is

$$\epsilon_\nu^{\text{FF}} = \frac{32}{3} \sqrt{\frac{\pi}{3}} \alpha^3 \chi_H a_0^3 \langle Z^2 \rangle n_e n_i \left(\frac{\chi_H}{kT} \right)^{1/2} g_{\text{FF}} e^{-h\nu/kT}, \quad (8)$$

where α is the fine-structure constant, $\alpha \cong 1/137$, a_0 is the Bohr radius, and χ_H is the K-shell ionization energy of hydrogen.⁹ The units of this expression are energy per volume, per steradian, per time, and per frequency. Throughout this article, $T = T_e$ is the electron temperature. Since the hot-spot hydrogen

almost completely ionized, $\langle Z^2 \rangle = 1$ but the Z dependence in Eq. (8) will be kept, anticipating the discussion below of the contamination of the hot spot by carbon as the result of fuel-shell mix. As will be shown in **Enhanced X-Ray Emission as a Measure of Fuel-Shell Mix** (p. 176), the FB contribution to hydrogen emissivity is negligible under hot-spot conditions.

This emissivity is written in a form first obtained in a semiclassical treatment by Kramers.¹⁶ The correction factor g_{FF} accounts for quantum-mechanical effects in FF absorption and emission and also in other absorption and emission processes introduced by Gaunt.¹⁷ The same Gaunt factor applies to both emission and absorption, a result of the microscopic reversibility of these processes.¹⁸ Many versions of the Gaunt factor have been provided over many years by many authors who, to cite just a few, include correct isolated-ion quantum wave functions,¹⁹ relativistic effects,²⁰ collective effects,²¹ and high-density effects such as electron degeneracy²² and strong plasma coupling.^{23,24} A particularly simple and accurate Gaunt factor for hydrogen has been provided by Kulsrud:²⁵

$$g_{\text{FF}} = \frac{\sqrt{3}}{\pi} \ln \left[\frac{(\beta^2 + u)^{1/2} + \beta}{(\beta^2 + u)^{1/2} - \beta} \right], \quad (9)$$

where $u = hv/kT$ and β^2 is an average energy parameter

$$\beta^2 = \left\langle \frac{E}{kT} \right\rangle, \quad (10)$$

representing an effective average initial electron energy E . Rather than averaging the FF scattering cross section over the Maxwell distribution of initial electron momenta, Kulsrud provides the Gaunt factor for a single average initial electron momentum. He finds that the value $\beta = 0.87$ provides a good fit to a more-accurate quantum result of Sommerfeld based on the Born approximation.²⁵ We verify that Eq. (9) is a good approximation to the standard results of Karzas and Latter¹⁹ (KL) in the high-temperature limit $kT \gg \chi_{\text{H}}$, which is the relevant regime for implosion cores at peak conditions. We also verify that the asymptotic expression

$$g_{\text{FF}} \approx \frac{2\sqrt{3}}{\pi} \frac{\beta}{u^{1/2}} \quad (11)$$

is a useful approximation to Eq. (9) at high photon energies $hv > kT$. This is consistent with the sensitive range of the filtered

gated monochromatic x-ray imager (GMXI) camera²⁶ ($hv \sim 5$ keV), described below, and the expected core temperatures ($kT \sim 2$ keV). This is also well into the optically thin spectral range where emission is directly related to the hot-spot emissivity. Using Eq. (11) in Eq. (8) provides an emissivity expression with accurate temperature and photon-energy scaling that will be used in a later discussion of the interpretation of measured energy-integrated core emission.

Some brief textbook summaries of FF and FB emission and absorption dismiss the Gaunt factor as a constant correction of order unity,³ which for our purposes would be a poor approximation. Equation (11) provides a convenient simplification and ensures correct asymptotic scaling behavior. This asymptotic expression for the Kulsrud Gaunt factor is plotted in Fig. 139.13 along with the result of the full expression, Eq. (9), and KL values.¹⁹ The Kulsrud Gaunt factor depends only on $u = hv/kT$, while the KL results also depend on the parameter $\gamma^2 = Z^2 \chi_{\text{H}}/kT$. Here, we simply plot the KL values for hydrogen ($Z = 1$) at temperatures 2 keV and 6 keV to show that the departure of the KL from the Kulsrud values is small and that their temperature dependence at constant $u = hv/kT$

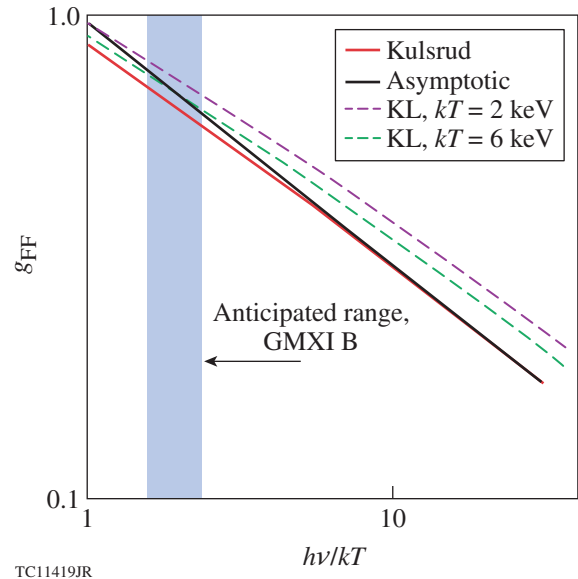


Figure 139.13 Plot of the Kulsrud²⁵ approximation to the hydrogen free-free (FF) Gaunt factor versus $u = hv/kT$ (red line) given by Eq. (9) and its asymptotic approximation given by Eq. (11) (black line). Karzas-Latter (KL) values for $kT = 2$ and 6 keV are shown for comparison. The relevant range of u for the anticipated core conditions and instrumentation (GMXI B) is indicated by the blue shading. The asymptotic behavior of the Kulsrud approximation agrees with that of the KL values.¹⁹

can be cautiously disregarded for the purposes of this discussion. The plot range is extended over an order of magnitude to show that the asymptotic behavior of the Kulsrud expression is correct. The relevant range of $h\nu/kT$ for our chosen imaging instrument, the GMXI, with a response function denoted here and in Fig. 139.13 as “B,” is indicated by the blue-shaded strip. Here, the agreement among the four results is particularly close. The KL and Kulsrud formulations do not consider the effects of relativistic electron motion or the effects of degeneracy and strong coupling on the energy levels of the ions and on the free-electron energy distribution. These effects will not be significant under hot-spot emission conditions, although the latter two effects must be considered in the surrounding, relatively cold compressed shell, particularly earlier in the implosion.²⁴ Evaluating the numerical coefficient in Eq. (11) gives $g_{\text{H,FF}} \approx 0.959 u^{-0.5}$, which is very close to $g_{\text{H,FF}} = 0.966 u^{-0.41}$, a numerical fit to the KL hydrogen FF result near $h\nu \approx 5.39$ keV and $h\nu_0/kT \approx 2$, anticipating the conditions where Eq. (11) will be applied.

Let us specialize to fully ionized hydrogen, where $\langle Z^2 \rangle = 1$ and $n_e = n_i$. We then insert the Kulsrud Gaunt factor given by Eq. (11) into Eq. (8) and obtain

$$\varepsilon_{\nu}^{\text{FF}} = \frac{64}{3\sqrt{\pi}} \beta \alpha^3 \chi_{\text{H}} a_0^3 n_i^2 \left(\frac{\chi_{\text{H}}}{kT} \right)^{1/2} \left(\frac{kT}{h\nu} \right)^{1/2} e^{-h\nu/kT}. \quad (12)$$

Using the ideal gas equation of state $P = (n_e + n_i) kT$ to replace density with pressure, we obtain

$$\varepsilon_{\nu}^{\text{FF}} = \frac{16}{3\sqrt{\pi}} \beta \alpha^3 \chi_{\text{H}} a_0^3 \left(\frac{P}{kT} \right)^2 \left(\frac{\chi_{\text{H}}}{h\nu} \right)^{1/2} e^{-h\nu/kT}. \quad (13)$$

This ideal gas equation of state is an approximation to the more general expression $P = k(n_e T_e + n_i T_i)$, recognizing that the ion temperature T_i can exceed the electron temperature during the convergence of shocks that forms the hot spot. During peak compression, however, the two temperatures equilibrate rapidly, so $T_i = T_e$ —a useful approximation that has been standard in recent discussions of hot-spot dynamics—can be applied here with caution. We will show that this emissivity is almost exclusively a function of pressure when measured with an appropriate spectral response.

Three spectral-response channels of the GMXI²⁶ x-ray camera are shown in Fig. 139.14. These response functions are nearly Gaussian in shape with spectral widths of approxi-

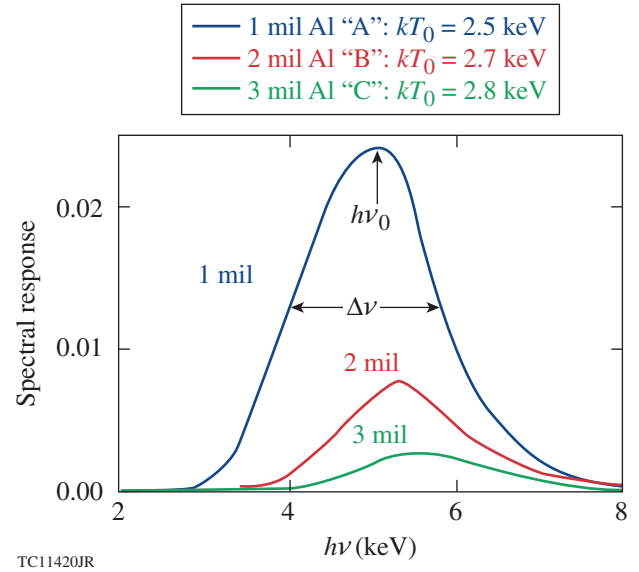


Figure 139.14

Plot of the GMXI²⁶ camera spectral-response functions $F(\nu)$ for three of its channels. These channels differ by the thicknesses of the Al filter layers in their respective filter packages. The emissivity of a source, integrated over one of these response functions, will be exclusively dependent on the pressure of the source when the source temperatures fall within a narrow range near the ideal source temperature kT_0 indicated for that channel.

mately $\Delta h\nu \approx 1$ keV centered at energies near $h\nu_0 \approx 5$ keV. The three channels, denoted A, B, and C, differ in the 1-, 2-, and 3-mil thicknesses of Al in their respective filter packages. These response functions are approximated adequately for our purposes by a Gaussian function

$$F(\nu) = F_0 e^{-(\nu - \nu_0)^2 / (\Delta\nu)^2} \quad (14)$$

with a transmission width $\Delta\nu$ centered at ν_0 . With a response function of the form of Eq. (14), the frequency-integrated emissivity expression obtained using the emissivity given by Eq. (13) is

$$E_{\nu_0, \Delta\nu} = \frac{16}{3\sqrt{\pi}} \alpha^3 \chi_{\text{H}} a_0^3 \beta \left(\frac{P}{kT} \right)^2 \left(\frac{\chi_{\text{H}}}{kT} \right)^{1/2} \times F_0 \int_0^{\infty} \left(\frac{kT}{h\nu} \right)^{1/2} e^{-(\nu - \nu_0)^2 / (\Delta\nu)^2} e^{-h\nu/kT} d\nu. \quad (15)$$

For the anticipated small values of the parameters $\Delta\nu/\nu_0$ and $h\Delta\nu/kT$, we use the leading-order approximation

$$\begin{aligned} & \left(\frac{h}{kT}\right)^{1/2} \int_0^{\infty} e^{-(\nu-\nu_0)^2/(\Delta\nu)^2} e^{-h\nu/kT} \frac{d\nu}{\nu^{1/2}} \\ & \simeq \sqrt{\pi} \frac{\Delta\nu}{\nu_0} \left(\frac{h\nu_0}{kT}\right)^{1/2} e^{-h\nu_0/kT}, \end{aligned} \quad (16)$$

and we write

$$E_{\nu_0, \Delta\nu} = \frac{16}{3} \alpha^3 \chi_H a_0^3 \beta F_0 \Delta\nu \left(\frac{P}{kT}\right)^2 \left(\frac{\chi_H}{h\nu_0}\right)^{1/2} e^{-h\nu_0/kT}. \quad (17)$$

Near any given temperature, the temperature dependence of Eq. (17) can be treated as a power law $y \sim x^\eta$ fit to the actual temperature dependence of the form

$$y = \frac{e^{-1/x}}{x^\eta}, \quad (18)$$

where $x = kT/h\nu_0$. The exponent η near a particular value of x is

$$\eta = \frac{x}{y} \frac{dy}{dx} = \frac{1 - \eta x}{x}. \quad (19)$$

Solving for $\eta = 0$ gives $x = 1/\eta$. The temperature dependence of Eq. (17) is the $n = 2$ case, which gives

$$kT_0 = \frac{h\nu_0}{2} \quad (20)$$

as the condition for stationary maximum integrated emissivity with respect to temperature. So while Eq. (17) is explicitly temperature dependent, it can be regarded as independent of temperature within a limited range of temperature centered at kT_0 . If the KL fit given above were used rather than the asymptotic Kulsrud expression, Eq. (18) would be replaced by $y = e^{-1/x}/x^{2.09}$, displacing the stationary point of the emissivity to $kT_0 = h\nu_0/2.09$, which is almost the same as Eq. (20) for the purposes of this discussion. The applicable range of temperature is easy to determine directly from Eq. (17) for a desired tolerance. For example, the integrated emissivity will be within 90% of its maximum (representing a $\pm 5\%$ minimum-to-maximum variation) at $kT_0 = 2.65$ keV over the temperature range $1.95 \text{ keV} < kT < 3.73 \text{ keV}$ for the GMXI B response function with the $h\nu_0 = 5.30$ -keV center energy. This temperature range is representative of cryogenic ICF implosion hot spots.

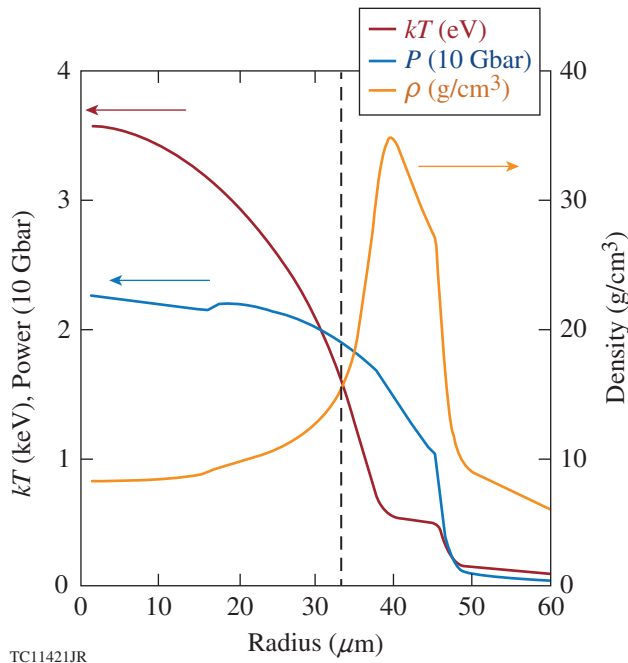
What we now have in Eq. (17) is an expression for emissivity that is a function of pressure alone, as long as the spectral response of the detector is appropriately matched to the source

temperature range. A nominal temperature value or profile must be provided to evaluate Eq. (17), but if the source-instrument matching condition given by Eq. (20) is satisfied closely enough, the emissivity can be treated as a function of pressure alone. If the source temperature profile does deviate from satisfying Eq. (20) to a degree that the emissivity temperature dependence at fixed pressure cannot be ignored, Eq. (17) is still valid, but temperature profile input must then resemble the actual temperature profile closely enough to avoid throwing off the relationship between the emissivity and the pressure profiles. A temperature profile from a simulation may suffice.

Inferring Hot-Spot Pressure from X-Ray Emission Measurements

The expression for Abel inversion given by Eq. (4) and the emissivity expression in terms of pressure given by Eq. (17) allow the pressure profile to be inferred from the imaged specific intensity $I_{\nu_0}(x)$. This will be demonstrated using a simulated image of OMEGA cryogenic implosion shot 68791 (Ref. 27). The implosion is simulated with the one-dimensional (1-D) radiation-hydrodynamics code *LILAC*,²⁸ and the images are calculated using the post-processor *Spect3D*.²⁹ The temperature, density, and pressure profiles of this implosion at 1.94 ns—the time of stagnation and peak neutron production—are shown in Fig. 139.15. A GMXI image of the emission from this configuration simulated with *Spect3D*, using the spectral response function B with 2-mil Al filtering shown in Fig. 139.14, is shown as the red solid line in Fig. 139.16. *Spect3D* uses the actual response functions specified for the GMXI [not the Gaussian approximation used in deriving Eq. (17)] and Gaunt factors based on the KL model extended to include the effects of electron degeneracy.²⁰ *Spect3D* calculates a full solution of the equivalent of Eq. (1), taking into account all emission and absorption effects within the entire imploded configuration.

The simulated imploded configuration in Fig. 139.15 is substantially isobaric at $P \approx 22$ Gbar out to the radius indicated by the vertical dashed line at $34 \mu\text{m}$. In the simulated instantaneous image at this time shown in Fig. 139.16 and in the plot of the simulated time-integrated image in Fig. 139.17, this distance represents the radius of the 17% intensity contour of the instantaneous image, which has been suggested as one criterion to use in measuring the size of a hot spot from its image.³⁰ This criterion appears to coincide with other criteria that are more physically significant, although, unfortunately, not as directly measurable, such as the inner half-peak density point of the imploding mass distribution in Fig. 139.15 or the half-emissivity radius seen in Figs. 139.16 and 139.17. The

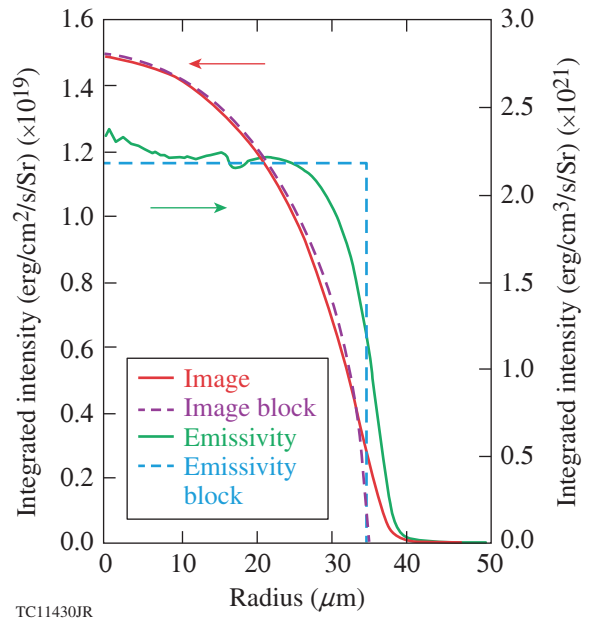


TC11421JR

Figure 139.15
 Simulated OMEGA cryo shot 68791 (Ref. 27) profiles at 1.94 ns, the time of peak neutron production. The hot spot ($kT > 1.5$ keV) appears to be substantially isobaric at $P \approx 22$ Gbar out to the radius indicated by the vertical dashed line at $34 \mu\text{m}$. In the simulated instantaneous image at this time, this distance represents the radius of the 17% intensity contour,³⁰ which is also shown for reference on the image plots in Figs. 139.16–139.18.

temperature range within this so-defined hot spot is roughly $1.5 \text{ keV} < kT < 3.5 \text{ keV}$, which extends only slightly below the temperature range given above for a $\pm 5\%$ accuracy limit on Eq. (17) with a nominal temperature of $kT_0 = 2.65 \text{ keV}$. Therefore, the flat emissivity profile in Fig. 139.16 should track the flat pressure profile in Fig. 139.15, even as the temperature varies. This is indeed the case, as will be shown below.

The solid red curve in Fig. 139.16 is the simulated instantaneous radial intensity distribution of the image obtained using the B response function including the 2-mil Al filter layer of OMEGA cryogenic implosion shot 68791 at 1.94 ns—the time of stagnation and peak neutron production shown in Fig. 139.15. The solid green curve is the emissivity profile obtained from the inverse Abel transform of this image using Eq. (4). The image is almost indistinguishable from the dashed purple quarter-ellipse, which is exactly what Eq. (5) predicts for the image of a constant emissivity profile extending out to $R = 34 \mu\text{m}$, shown in Fig. 139.16 as the dashed blue profile. The relative deviations of the simulated image from the elliptical image are very small, in contrast with the larger relative deviations of the simulated emissivity from a flat profile. This



TC11430JR

Figure 139.16
 The filtered simulated GMXI image of the simulated implosion core of OMEGA shot 68791 at 1.94 ns—the time of peak neutron production. The red solid line (image) is the B-channel integrated intensity distribution of the simulated image. The green solid line (emissivity) is the emissivity profile obtained from the inverse Abel transform of the simulated image. The image is almost indistinguishable from the purple dashed line (image block), which is the image of a constant emissivity profile (emissivity block) extending out to $R = 34 \mu\text{m}$.

is understood as the smoothing effect of the integration in Eq. (2) on the emissivity profile.

Figure 139.17 is virtually identical to Fig. 139.16 in every respect, other than a relative factor of about 110 ps, which can be taken as the emission time scale. This simulated image intensity has been integrated over a 300-ps time window centered at 1.96 ns, long enough to include both the x-ray and neutron emission times. Again, as was the case with the results shown in Fig. 139.16, the image deviates very little from the elliptical shape, while the emissivity deviates more visibly from a flat profile near the outer radius of the hot spot.

The pressure profile of an imploded hot spot can be inferred using Eq. (17) from the emissivity profile obtained by Abel inversion of the simulated image using Eq. (4). As discussed in the previous section, this inferred pressure is insensitive to the assumed temperature profile if the camera response is centered at $h\nu_0 = 2kT_0$, where the hot-spot temperatures are within a limited range of T_0 . Exactly how closely the emissivity profile follows the pressure profile will depend on how far the range of the hot-spot temperature deviates from T_0 , as has been

described above. In principle, any nominal T value or radial $T(r)$ profile can be used with Eq. (17). For example, this nominal temperature can be the ideal temperature T_0 matched to the instrument response, or it can be the logarithmic slope of the hard end of the continuum spectrum, if it has been measured. Ignoring the Gaunt factor in Eq. (8) leaves one with the simple $\epsilon_v^{FF} \sim e^{-h\nu/kT}$ frequency dependence. The additional factor $(kT/h\nu)^{1/2}$ in Eq. (12) bends the logarithmic slope slightly,

$$-\frac{d \ln(\epsilon_v^{FF})}{dh\nu} = \frac{1}{kT_{\text{inferred}}} = \frac{1}{kT} + \frac{1}{2h\nu}, \quad (21)$$

but the fractional error in the temperature inferred from measuring the spectral logarithmic slope $\delta T/T \approx kT/2h\nu$ can be minimized by measuring as high in spectral energy as possible. Using Eq. (17) with a radially dependent simulated temperature profile could provide more-accurate results than a constant nominal temperature.

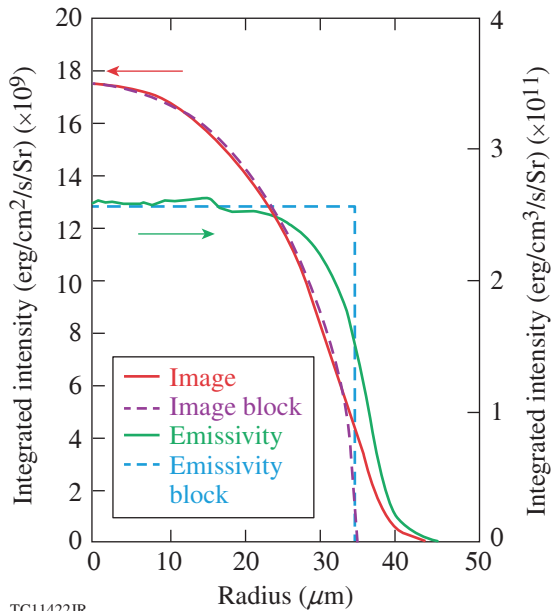


Figure 139.17
The filtered simulated GMXI image of the simulated implosion core of OMEGA shot 68791 integrated over a 300-ps time window centered at 1.96 ns. This interval includes the times of stagnation, peak neutron production, and peak x-ray intensity. All plotted quantities in this figure are time integrated. The red solid line (image) is the intensity distribution of the simulated image. The green solid line (emissivity) is the emissivity profile obtained from the inverse Abel transform of the image. Out to near $R = 34 \mu\text{m}$, the image is almost indistinguishable from the purple dashed line (image block), which is the image of a constant emissivity profile (emissivity block).

Using Eq. (17) to infer a pressure profile from an emissivity profile is demonstrated in Fig. 139.18 for the case of shot 68791 shown in Fig. 139.16. Pressure profiles inferred from the simulated GMXI B-channel image of the simulated implosion core of OMEGA shot 68791 are shown in Fig. 139.16 at 1.94 ns—the time of peak neutron production. The pressure profiles were obtained using Eq. (17) from the emissivity profile obtained from the simulated image by Abel inversion. The pressure profile plotted as the red solid line was obtained assuming the ideal $kT_0 = 2.65 \text{ keV}$ nominal temperature based on the

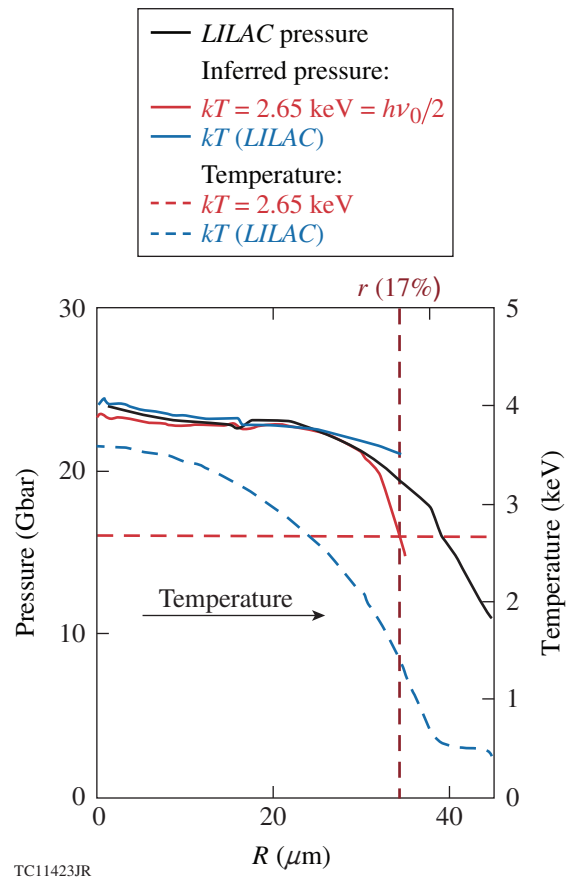


Figure 139.18
Pressure profiles inferred from the simulated GMXI image shown in Fig. 139.16 of the simulated implosion core of OMEGA shot 68791 at 1.94 ns—the time of peak neutron production. The pressure profiles were obtained using Eq. (17) from the emissivity profile obtained from the simulated image by Abel inversion. The pressure profile plotted as the red solid line was obtained assuming the ideal $kT_0 = 2.65 \text{ keV}$ nominal temperature based on the GMXI response centered at 5.30 keV (red dashed line), and the pressure profile plotted as the blue solid line was obtained by assuming the radius-dependent temperature profile from the LILAC hydrodynamic simulation (blue dashed line). The vertical dashed line indicates the 17% intensity contour radius—the nominal outer radius of the hot spot.

GMXI response centered at 5.30 keV (red dashed line), and the pressure profile plotted as the blue solid line was obtained by assuming the radius-dependent temperature profile from the *LILAC* hydrodynamic simulation (blue dashed line). The vertical dashed line indicates the 17% intensity (half-emissivity) contour radius—the nominal outer radius of the hot spot. Even with these two very different assumed temperature profiles, the two inferred pressure profiles agree with the simulated pressure profile very well, up to within a short distance of the edge of the hot spot.

Scaling Relationships of the X-Ray Yield of an Isobaric Hot Spot at Stagnation

The energy-integrated emissivity of an isobaric hot spot tracks its flat pressure profile nearly all the way to its outer radius R , provided that the source temperature profile does not deviate too far from the T_0 set by the condition $h\nu_0 = 2kT_0$, where $h\nu_0$ is the center of the instrument-response function. If the emissivity per volume is reasonably uniform over the entire hot spot, as is the case in the example shown in Fig. 139.16, the hot spot will produce a total filtered radiated energy or photon yield of

$$Y_{\nu_0} = 4\pi \left(\frac{4\pi}{3} R^3 \right) \Delta t E_{\nu_0}, \quad (22)$$

where the leading factor of 4π represents integration of the isotropic emissivity over the full sphere of the solid angle. If the gate time or exposure time Δt exceeds the lifetime of the hot spot, the total effective emission time Δt must be inferred from another measurement, such as the neutron yield Y_n , assuming that both the neutron and photon emission are limited by the same hot-spot lifetime. With a radius R obtained from the GMXI image and a relatively weak temperature dependence, a useful estimate of the hot-spot pressure can be obtained from Eqs. (17) and (22). This was done for a sizable ensemble of cryogenic implosion simulation results.²⁷ The inferred pressures are compared in Fig. 139.19 with the simulated central peak pressures. The simulated photon yield was the time-integrated B-channel emission, the emission time in Eq. (22) is the quotient of the simulated neutron yield divided by the peak neutron-production rate, and the image size is the 17%-intensity contour of the simulated GMXI image. The ensemble of implosions includes shell adiabat parameters over the range $1.5 < \alpha_{\text{shell}} < 3.5$ and neutron yields over the range $1.3 \times 10^{13} < Y_n < 1.3 \times 10^{14}$. The close agreement between the pressures inferred from the simulated images and the simulated pressure values is convincing, although not entirely expected,

in light of the combined systematic inaccuracy that might result from equating the photon and neutron emission lifetimes, using the reasonable but not unique choice of the 17% contour as the hot-spot radius, and from assuming that the emissivity of the entire hot spot is determined by the central pressure at stagnation alone. This effectively confirms that the agreement between the simulated and inferred central pressures in Fig. 139.18 is obtained for every implosion in this ensemble.

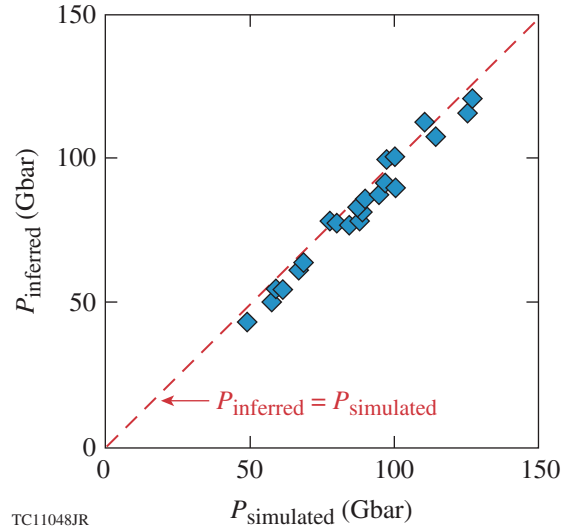


Figure 139.19 The hot-spot pressure inferred from *LILAC/Spect3D* simulated images shown in very good agreement with the simulated peak central pressure. Equations (17) and (22) give accurate hot-spot pressures from simulated images for an ensemble of cryogenic simulations representing a broad range of shell adiabat parameters and neutron yields.

A few interesting new expressions for the scaling of the photon yield with various parameters of the implosion can be obtained from Eqs. (17) and (22). First, we write

$$M_{\text{Sh}} \frac{R}{(\Delta t)^2} = 4\pi R^2 P, \quad (23)$$

saying that the imploding thin unablated shocked shell of mass M_{Sh} surrounding the hot spot of radius R experiences an outward acceleration $R/(\Delta t)^2$ at stagnation, where Δt is the scale time of the bounce of shell, by the force of the hot-spot pressure P acting on the inner surface of the shell.¹¹

Next, we can write the adiabatic scaling of the hot-spot pressure with respect to the hot-spot volume $V = 4\pi R^3/3$ as

$$P \propto \alpha_{\text{HS}} V^{-5/3}, \quad (24)$$

where α_{HS} , a hot-spot “adiabat” parameter, distinguishes among the hot spots of different implosions. The stagnating hot-spot material is not adiabatic in the usual sense where the pressure would scale with the hot-spot density as $P \propto \alpha_{HS} \rho^{-5/3}$ because of heat flow out of and material flow into the hot spot. The hot-spot volume, however, can be treated as an adiabatic enclosure because the heat conduction out of the hot spot is exactly compensated by the heat of the material ablated off the inner surface of the shell back into the hot spot at the hot-spot boundary.¹¹ Together, Eqs. (23) and (24) give the volume–time product

$$V\Delta t \propto \frac{(\alpha_{HS} M_{Sh})^{1/2}}{P} \tag{25}$$

needed in Eq. (22). Applying Eq. (17), subject to the conditions given above for temperature-independent emissivity, we obtain the expression

$$Y_{\nu_0} \propto (\alpha_{HS} M_{Sh})^{1/2} P, \tag{26}$$

which predicts that the photon yield will scale in direct proportion to the hot-spot pressure for an ensemble of similar cryogenic implosions. This linear scaling is verified in Fig. 139.20 for the same set of simulations used to obtain the results shown

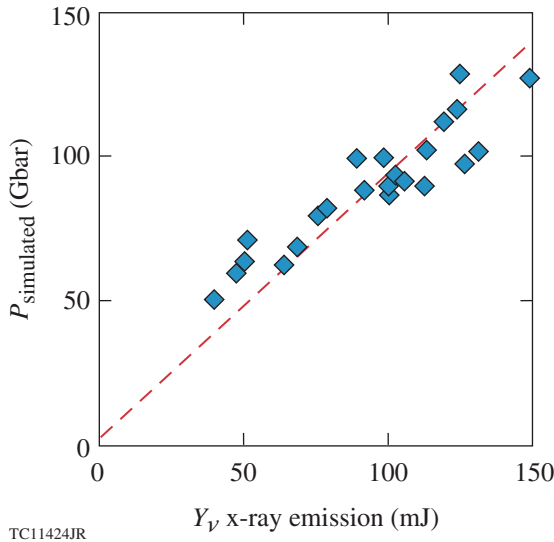


Figure 139.20 The hot-spot pressure simulated by *LILAC* shown following the predicted linear scaling with the photon yield. The hot-spot pressure is predicted to vary in direct proportion to the x-ray yield for an ensemble of similar cryogenic implosions with shell adiabat parameters and neutron yields that vary over a wide range.

in Fig. 139.19, although with more scatter. This additional scatter may reflect the simplification of the hot-spot dynamics by Eq. (23) and the simplification of the hot-spot energy balance by Eq. (24) or by the variations in the product $\alpha_{HS} M_{Sh}$ over the ensemble. Accounting for all the details of Fig. 139.20 is beyond the scope of this article, but for now, Fig. 139.20 suffices to add validity to the scaling arguments that have been made.

The sample of 1-D OMEGA cryogenic implosion simulations illustrated in Figs. 139.19 and 139.20 displays a curious scaling of the simulated photon yield with the neutron yield, $Y_{\nu_0} \propto Y_n^{0.57}$, shown in Fig. 139.21 (Ref. 27). The value of the scaling index, as well as the fact that the photon and neutron yields appear to fall along a single curve, can be explained in terms of the dynamics of isobaric implosion cores at stagnation. We begin again with the photon yield given by Eqs. (17) and (22), this time keeping track of the precise temperature scaling of the photon- and neutron-production rates. We allow that the scaling index η of the temperature dependence of Eqs. (18) and (19), as in

$$y = \frac{e^{-1/x}}{x^2} \propto x^\eta, \tag{27}$$

may deviate from $\eta = 0$. We expect that η will be small since our instrumentation and emission source place us near $h\nu_0 =$

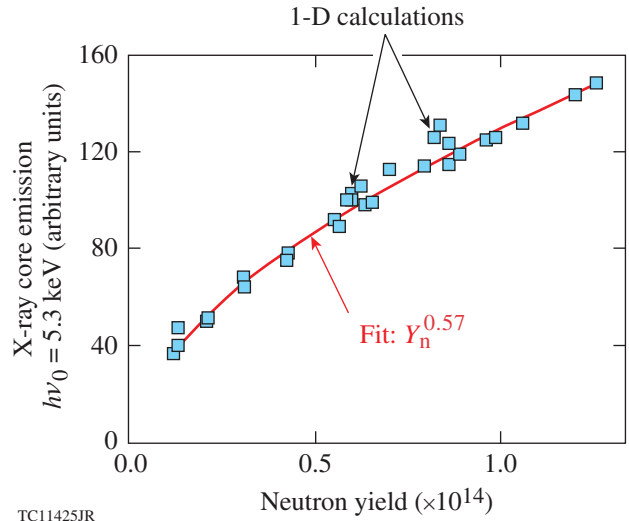


Figure 139.21 Photon/neutron-yield scaling in cryogenic implosion simulations.²⁷ The x-ray yields of an ensemble of cryogenic implosion simulations have been found to scale with the 0.57 power of their respective neutron yields over a broad range of shell adiabats and neutron yields.

$2kT_0$, but the scaling calculation below does not require this. We apply Eqs. (17), (22), and (27) and obtain

$$Y_{\nu_0} \propto P^2 T^\eta V \Delta t. \quad (28)$$

The neutron yield can be written using the deuterium-tritium (DT) reaction rate

$$\langle \sigma v \rangle \propto T^{4+\varepsilon}, \quad (29)$$

where we obtain the small deviations $|\varepsilon| \ll 1$ from a fixed temperature scaling using the reaction rate by Bosch and Hale.³¹ The neutron yield is written as the volume and time integral

$$Y_n = \iint n_D n_T \langle \sigma v \rangle dV dt \propto P^2 T^{2+\varepsilon} V \Delta t. \quad (30)$$

The neutron-production rate is a function of the ion temperature, so combining Eq. (29) with the ideal gas equation of state to form Eq. (30) is another application of the $T_e = T_i$ equilibrium assumption made earlier. While the x-ray emissivity can be approximated fairly well as uniform over the volume of an isobaric hot spot, the neutron production varies as an additional two powers of temperature and, as a result, will be more center peaked and possibly shorter in duration. Nevertheless, we proceed assuming that the usual approximation—that the source volumes and emission times of the neutrons and photons are the same—is valid to within constant factors that drop out of scaling relationships, and we apply Eqs. (24), (25), (28), and (30) to obtain

$$Y_{\nu_0} \propto \left(\frac{M_{Sh}^{2/9} M_{HS}^{10/9}}{\alpha_{HS}^{4/9}} \right)^p Y_n^q, \quad (31)$$

where

$$p = \frac{1 + (\varepsilon - \eta)/2}{1 + 2\varepsilon/9} \quad (32)$$

and

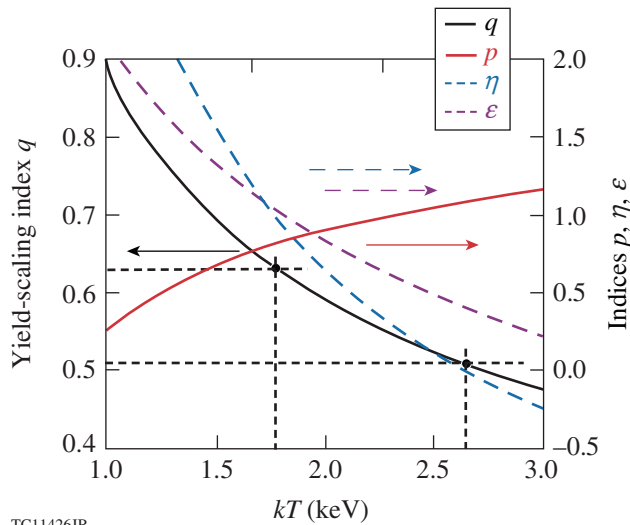
$$q = \frac{5 + 2\eta}{9 + 2\varepsilon}. \quad (33)$$

For the nominal values $\eta = \varepsilon = 0$, this gives $q = 0.56$ for the neutron-yield scaling exponent, which is very close to the value obtained from the simulation ensemble, as shown in Fig. 139.21. In Eq. (31), the three constant stagnation parameters α_{HS} , M_{Sh} , and the hot-spot mass $M_{HS} \sim R^3 P/T$ combine in a product where the scaling relative to each other is fixed. We have chosen to write Eq. (31) with this three-parameter product scaled such

that $p = 1$ for the nominal values $\eta = \varepsilon = 0$. The effects of variations of α_{HS} , M_{Sh} , and M_{HS} throughout the simulation ensemble and the effects of the temperature-dependent scaling corrections η and ε will be considered below, but for now the successful derivation of the value of the scaling exponent q is clearly an encouraging validation of the scaling calculations so far.

The alignment of the simulated data points in Fig. 139.21 along a single curve does make sense in light of Eq. (31). The neutron yield varies over the ensemble by an order of magnitude, and the scatter about the curve, attributable to variations in α_{HS} , M_{Sh} , and M_{HS} , is relatively small. Extracting precise values of these three parameters from simulations depends on the time resolution of the simulation output as well as on somewhat arbitrary definitions, but it is clear that the net effect of their variations is much less than the ranges of the neutron and photon yields. It is interesting to note that the temperature-dependent scaling corrections pertain only to the microphysics of photon and neutron production, not the design or dynamics of the implosion capsules. Were this yield-yield plot generated with simulations or measurements of a different ensemble of isobaric implosions with target masses scaled up by significant factor, for example, Eqs. (31)–(33) predict that the overall proportionality constant would change with the mass and hot-spot adiabat parameter, the yield-scaling exponent would be the same for the same spectral response and source temperatures.

The result $q = 0.56$ quoted above is obtained only with the nominal values $\eta = \varepsilon = 0$. Their actual values are plotted as functions of temperature in Fig. 139.22 as blue and purple dashed curves, respectively, where they are read off the right-hand scale. The q value obtained from Eq. (33) is plotted on the same graph as the black curve and is read off the left-hand scale. The left-hand scale is only a fifth the numerical length of the right-hand scale, indicating that q is a relatively insensitive function of temperature because of its opposite sensitivities to ε and η in Eq. (33). The range $q = 0.57 \pm 0.06$ is obtained, in reasonably good agreement with the value $q = 0.57$ in Fig. 139.21, for the broad range of temperature $kT = 2.21 \pm 0.43$ keV. Even though the yield-scaling exponent is relatively insensitive to variations in the hot-spot temperature, it may have diagnostic value through its temperature dependence. The red curve representing the scaling index p is to be read off the right-hand scale and is a relatively insensitive function of temperature within the 0.86-keV range indicated by the pair of vertical dashed lines. If the fit to KL results for the FF Gaunt factor described above were used in place of Eq. (11), the effect would be to reduce η by 0.09, which would reduce the predicted q values by 3.6% overall.



TC11426JR

Figure 139.22

Yield-scaling indices as functions of temperature. The yield-scaling indices p and q are functions of temperature through the temperature-dependent scaling indices η and ε of the photon- and neutron-production rates, respectively. The q curve shows that the $q = 0.57$ value from Fig. 139.21 is at the center of the range $q = 0.57 \pm 0.06$, corresponding to the temperature range $kT = 2.21 \pm 0.43$ keV.

Equation (31) with its scaling index given by Eq. (32) accounts for the yield-scaling behavior shown in Fig. 139.21 because the scaling parameter agrees with the fit to the simulation ensemble and because the scaled product $M_{\text{Sh}}^{2/9} M_{\text{HS}}^{10/9} \alpha_{\text{HS}}^{-4/9}$ of stagnation parameters has negligible correlations with both the photon and neutron yields. The simulation ensemble was constructed to follow a long series of cryogenic implosion experiments as closely as possible; the experiments were not designed to control this product. If this product did have a significant correlation with either the photon or neutron yields, then Eq. (32) would not agree with the yield scaling exhibited by the simulation ensemble. For example, a slightly modified version of Eq. (31) can be derived by using the scaling expression

$$M_{\text{HS}} \sim M_{\text{Sh}}^{1/7} P^{4/7} R^{16/7} \quad (34)$$

for the hot-spot mass given by Zhou and Betti³² to remove M_{HS} from the calculation. This gives the results

$$Y_{\nu_0} \propto (M_{\text{Sh}}^{4/11})^{p'} Y_{\text{n}}^{q'}, \quad (35)$$

where

$$p' = \frac{1 + (\varepsilon - \eta)/2}{1 + 2\varepsilon/11} \quad (36)$$

and

$$q' = \frac{7 + 2\eta}{11 + 2\varepsilon}. \quad (37)$$

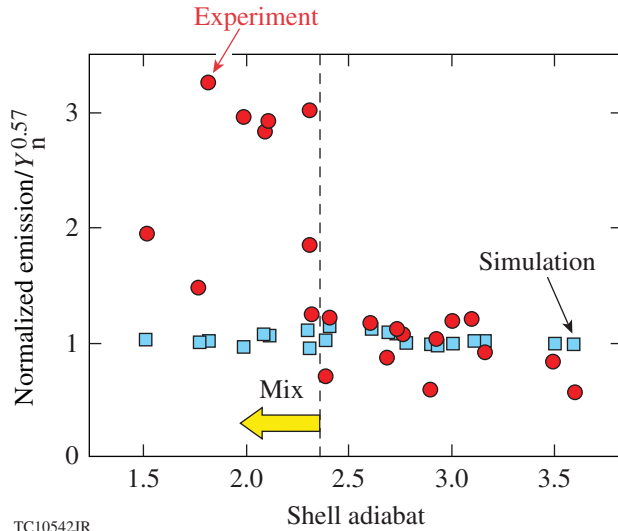
These results are only a slight departure from Eqs. (31)–(33). The yield-scaling parameter q' does not agree as well as q with the fit to the ensemble, but, remarkably, the only stagnation parameter appearing is M_{Sh} , or, in other words, the normalized photon yield

$$Y_{\nu_0} / Y_{\text{n}}^{q'} \sim M_{\text{Sh}}^{4p'/11}$$

is a function of the shell mass alone. Both Eqs. (31) and (35) are correct expressions, but if Eq. (33) agrees more with the simulation ensemble than Eq. (37), it is because M_{Sh} has a less negligible correlation with the photon and neutron yields. Another reason to regard Eqs. (35)–(37) with more caution than Eqs. (31)–(33) is that introducing Eq. (34) brings additional approximations into the calculation that were made to evaluate thermal transport in evolving inner-shell density and temperature profiles,¹¹ although these same approximations were made in establishing the hot-spot adiabatic behavior expressed as Eq. (24); the hot-spot pressure varies adiabatically with respect to the hot-spot volume during the approach to stagnation.

Enhanced X-Ray Emission as a Measure of Fuel-Shell Mix

The yield-scaling results in Fig. 139.21 were obtained from LILAC²⁸ 1-D hydrodynamic simulations, which exhibit no unstable hydrodynamic behavior. Implosions with shell adiabat parameters in the lower end of the range $1.5 < \alpha_{\text{shell}} < 3.5$ have thinner shells that are more susceptible to the Rayleigh-Taylor instability³³ during the deceleration phase of the implosion. Breakup of the unstable shell would leave some amount of the shell carbon mixed into the hot spot at the time of stagnation. Since carbon is much more emissive than hydrogen, very small concentrations of carbon can significantly increase the x-ray emission. Since the photon and neutron yields in Fig. 139.21 exhibit a $Y_{\nu_0} \propto Y_{\text{n}}^{0.57}$ behavior, the normalized yield quotient $Y_{\nu_0} / Y_{\text{n}}^{0.57}$ forms a constant normalized photon yield when plotted as a function of any quantity, such as the shell adiabat parameter, as shown by the blue squares in Fig. 139.23. The same quantity derived from actual measured yields is plotted as red circles. These values are generally constant, in agreement with the 1-D simulated results, for shell adiabat parameter values above the $\alpha_{\text{shell}} \approx 2.3$ value, but they show a distinct excess photon yield below this point. This has been attributed to the expected contamination of the hot spot by shell carbon. We extend this analysis to infer the mass of shell material mixed into the hot spot from measurements of this excess emission.



TC10542JR

Figure 139.23

Excess photon yield as a measure of fuel-shell mix. The normalized yield quotient $Y_{\nu_0}/Y_n^{0.57}$ is nearly constant for the simulated implosions, according to the results plotted here and in Fig. 139.21. This quotient is plotted versus the shell adiabat parameter here as blue squares. The same quotient calculated from measured yields is plotted as red circles. These measurements conform to the 0.57 power scaling for higher shell adiabat parameters $\alpha_{\text{shell}} > 2.3$. As unstable shells break up during the deceleration phase of the implosion, carbon can be mixed into the hot spot from the shell, which accounts for the excess x-ray emission above the amount expected from the yield scaling. This twofold to threefold enhancement can be attributed to masses of 125 to 250 ng of shell CH mixed uniformly into the hot spot. (Figure from Ref. 27.)

Using the FF emission of hydrogen as a pressure diagnostic assumes a pure hydrogen core. Any mix of non-hydrogen into the hot spot will raise the per-ion emissivity of the hot spot. The twofold-to-threefold enhancement of the hot-spot emission shown in Fig. 139.23 for low-adiabat implosions can be interpreted in terms of contamination of the hot spot by shell carbon. The emission from a carbon-contaminated hot spot will have a strong contribution from radiative recombination, which is FB emission, the time inverse of photoionization or bound-free (BF) absorption. The carbon emission will have comparable FF and FB contributions with much stronger total emission per ion than hydrogen.

Following a conventional approach, we discuss the combined FF and FB emissivity in parallel by considering their respective absorption cross sections. The Kramers photon absorption cross sections are

$$\sigma_{\text{FF}}(\nu) = \frac{256\pi^{5/2}}{3\sqrt{3}} \alpha a_0^5 n_e Z^2 \left(\frac{\chi_{\text{H}}}{kT}\right)^{1/2} \left(\frac{\chi_{\text{H}}}{h\nu}\right)^3 g_{\text{FF}} \quad (38)$$

for FF absorption by an ion of total charge Z and

$$\sigma_{\text{BF}}(\nu) = \begin{cases} \frac{64\pi}{3\sqrt{3}} \alpha a_0^2 \frac{Z^4}{p^5} \left(\frac{\chi_{\text{H}}}{h\nu}\right)^3 g_{\text{BF}}; & h\nu < \chi_p \\ 0; & h\nu > \chi_p \end{cases} \quad (39)$$

for BF absorption by the photoionization of the single electron bound to a nucleus of charge Z in principal quantum level p (Ref. 9). We keep the explicit dependence of $\sigma_{\text{BF}}(\nu)$ on p for now, but only the ground-state $p = 1$ photoionization contribution will be significant. The Gaunt factors g_{FF} and g_{BF} account for departures from the Kramers semi-classical approximation. Based on the micro-reversibility of each process, the Gaunt factor for emission also applies to absorption. The ionization-edge cutoff energy χ_p of the BF cross section is the ionization energy of the bound electron in the p shell. This can be expressed using the Bohr formula $\chi_p = Z^2 \chi_{\text{H}}/p^2 - \Delta\chi$. We mention continuum lowering³⁴ $\Delta\chi$ only for completeness, showing only its effect on χ . Since x-ray measurements are made far above this $h\nu = \chi_p$ cutoff, we will not consider it further. Further discussion beyond the scope of this article should consider continuum lowering and other high-density effects in more detail.

The hot-spot plasma is accurately described as nearly completely ionized, with the fully ionized atoms accounting for essentially all the FF and FB emission and with only a trace of the H-like species remaining to provide BF absorption. We neglect excited states and consider only the density $n_{i,1}$ of ground-state ($p = 1$) H-like ions and the density $n_{i,2}$ of the fully stripped species, so that $n_{i,1} + n_{i,2} = n_i$, where n_i is the total ion density of element i . Certainly for hydrogen and carbon, $n_{i,1}$ will be very small, and all other ionization species can be neglected. The hot spot is dense enough to maintain collision-dominated, detailed-balance local thermodynamic equilibrium (LTE) ionization-species population ratios given by the Saha equation⁹

$$\frac{n_{i,2} n_e}{n_{i,1}} = \frac{2}{a_0^3} \frac{g_2}{g_1} \left(\frac{kT}{4\pi\chi_{\text{H}}}\right)^{3/2} e^{-\chi_i/kT}, \quad (40)$$

where g_1 and g_2 are the statistical weights of the bound and stripped states, respectively. The statistical weights for H-like and stripped ions are $g_1 = 2p^2$ and $g_2 = 1$, respectively.

The FF opacity κ_{ν}^{FF} for the fully ionized species with nuclear charge Z ,

$$\kappa_{\nu}^{\text{FF}} = \frac{256\pi^{5/2}}{3\sqrt{3}} \alpha a_0^5 n_e n_{i,2} Z^2 g_{i,\text{FF}} \times \left(\frac{\chi_{\text{H}}}{kT}\right)^{1/2} \left(\frac{\chi_{\text{H}}}{h\nu}\right)^3 (1 - e^{-h\nu/kT}), \quad (41)$$

accounts for the entire FF contribution from that element since lower degrees of ion ionization contribute less, in proportion to their fractional populations. We can be more precise now by stipulating that the Gaunt factor $g_{i,\text{FF}}$ pertains to the fully stripped species of element i . The correction for stimulated emission is included. Considering a mixture of elements i , using $n_2 \approx n_i$, we have

$$\sum_i n_i Z_i^2 g_{i,\text{FF}} = n_i \langle Z^2 g_{Z,\text{FF}} \rangle,$$

where n_i is the total ion density, and

$$\kappa_{\nu}^{\text{FF}} = \frac{256\pi^{5/2}}{3\sqrt{3}} \alpha a_0^5 n_i n_e \langle Z^2 g_{\text{FF}} \rangle \times \left(\frac{\chi_{\text{H}}}{kT}\right)^{1/2} \left(\frac{\chi_{\text{H}}}{h\nu}\right)^3 (1 - e^{-h\nu/kT}). \quad (42)$$

The BF opacity for a single element is written in similar terms. Here, only the H-like species population $n_{i,1}$ is relevant in the fully ionized limit, giving simply

$$\kappa_{\nu}^{\text{BF}} = n_{i,1} \frac{64\pi}{3\sqrt{3}} \alpha a_0^2 \frac{Z^4}{p^5} \left(\frac{\chi_{\text{H}}}{h\nu}\right)^3 \times (1 - e^{-h\nu/kT}) g_{i,\text{BF}} \quad (43)$$

for the spectral range above the ionization edge. The BF opacity written in this way has strong hidden temperature and density dependence through $n_{i,1}$. The more-stationary product $n_{i,2}n_e$ is substituted using the Saha equation [Eq. (40)] to obtain

$$\kappa_{\nu}^{\text{BF}} = \frac{256\pi^{5/2}}{3\sqrt{3}} \alpha a_0^5 n_2 n_e \left(\frac{\chi_{\text{H}}}{h\nu}\right)^{3/2} \frac{g_1}{g_2} \frac{Z^4}{p^5} \left(\frac{\chi_{\text{H}}}{h\nu}\right)^3 \times (1 - e^{-h\nu/kT}) e^{(\chi - \Delta\chi)/kT} g_{i,\text{FF}}. \quad (44)$$

Again, considering a mixture of elements i , using $n_{i,2} \approx n_i$, we can write

$$\sum_i n_i Z_i^4 e^{(\chi - \Delta\chi)/kT} g_{i,\text{BF}} = n_i \langle Z^4 e^{(\chi - \Delta\chi)/kT} g_{\text{BF}} \rangle, \quad (45)$$

giving

$$\kappa_{\nu}^{\text{BF}} = \frac{256\pi^{5/2}}{3\sqrt{3}} \alpha a_0^5 n_i n_e \left(\frac{\chi_{\text{H}}}{kT}\right)^{3/2} \frac{g_1}{g_2} \frac{1}{p^5} \left(\frac{\chi_{\text{H}}}{h\nu}\right)^3 \times \langle Z^4 e^{(\chi - \Delta\chi)/kT} g_{Z,\text{BF}} \rangle (1 - e^{-h\nu/kT}). \quad (46)$$

Applying the appropriate values for g_1 , g_2 , and p given above for the H-like species, we have

$$\kappa_{\nu}^{\text{BF}} = \frac{512\pi^{5/2}}{3\sqrt{3}} \alpha a_0^5 n_i n_e \left(\frac{\chi_{\text{H}}}{kT}\right)^{3/2} \left(\frac{\chi_{\text{H}}}{h\nu}\right)^3 \times \langle Z^4 e^{(\chi - \Delta\chi)/kT} g_{Z,\text{BF}} \rangle (1 - e^{-h\nu/kT}). \quad (47)$$

In LTE, the Kirchhoff relationship¹⁴ $\epsilon_{\nu} = \kappa_{\nu} B_{\nu}(T)$ is the statistical detailed-balance relationship between emissivity and opacity, or between any one absorption process and its time-inverse emission process. Therefore,

$$\frac{\epsilon_{\nu}^{\text{BF}}}{\epsilon_{\nu}^{\text{FF}}} = \frac{\kappa_{\nu}^{\text{BF}}}{\kappa_{\nu}^{\text{FF}}} \quad (48)$$

and, applying Eqs. (42) and (47),

$$\frac{\epsilon_{\nu}^{\text{BF}}}{\epsilon_{\nu}^{\text{FF}}} = \left(\frac{2\chi_{\text{H}}}{kT}\right) \frac{\langle Z^4 e^{(\chi - \Delta\chi)/kT} g_{\text{BF}} \rangle}{\langle Z^2 g_{\text{FF}} \rangle}. \quad (49)$$

This ratio is independent of density, except at higher densities where continuum lowering $\Delta\chi \sim n_i^{1/3}$ becomes important. To gauge the relative importance of the participating processes, we set aside the Gaunt factors temporarily and write

$$\langle Z^4 e^{(\chi - \Delta\chi)/kT} g_{\text{BF}} \rangle \approx \langle Z^4 \rangle, \quad (50)$$

which is a valid simplification at very high temperatures, $kT \gg \chi \geq \chi_H$, and

$$\langle Z^2 g_{\text{FF}} \rangle \approx \langle Z^2 \rangle. \quad (51)$$

It is easy to see from Eqs. (49)–(51) that we have been correct in neglecting FB emission in hydrogen, relative to FF emission, but that the $\langle Z^4 \rangle / \langle Z^2 \rangle$ charge scaling of the FB-to-FF ratio predicts significant FB emission from mid- Z contaminants, in addition to their FF emission, even if they are present in trace amounts relative to hydrogen.

It may appear paradoxical that the BF-to-FF ratio given by Eq. (49) is independent of density, considering that BF absorption is initiated by a two-body (photon–ion) interaction, implying that its opacity is linear in density, while FF absorption is initiated by a three-body (photon–electron–ion) interaction, implying that its opacity is second order in density. In general, the ratio of densities in the BF-to-FF opacity ratio is density dependent, but since we are working in the near-complete ionization regime where all the bound-electron species are H-like, the Saha equation [Eq. (40)] removes this density dependence.

The Planck function in the Kirchhoff relationship can be written as

$$B_\nu(T) = \frac{\chi_H \alpha^2 \left(\frac{h\nu}{\chi_H}\right)^3}{8\pi^2 a_0^2} \frac{1}{e^{h\nu/kT} - 1}. \quad (52)$$

The individual emissivity contributions are then

$$\epsilon_\nu^{\text{FF}} = \frac{32}{3} \sqrt{\frac{\pi}{3}} \alpha^3 \chi_H a_0^3 n_i n_e \langle Z^2 g_{\text{FF}} \rangle \left(\frac{\chi_H}{kT}\right)^{1/2} e^{-h\nu/kT}, \quad (53)$$

repeating Eq. (8), and

$$\epsilon_\nu^{\text{BF}} = \frac{64}{3} \sqrt{\frac{\pi}{3}} \alpha^3 \chi_H a_0^3 n_i n_e \left(\frac{\chi_H}{kT}\right)^{1/2} \times \langle Z^4 e^{(\chi - \Delta\chi)/kT} g_{\text{BF}} \rangle e^{-h\nu/kT}, \quad (54)$$

with a total emissivity

$$\begin{aligned} \epsilon_\nu = & \frac{32}{3} \sqrt{\frac{\pi}{3}} \alpha^3 \chi_H a_0^3 n_i n_e \left(\frac{\chi_H}{kT}\right)^{1/2} \\ & \times \left[\langle Z^2 g_{\text{FF}} \rangle + 2 \left(\frac{\chi_H}{kT}\right) \langle Z^4 e^{(\chi - \Delta\chi)/kT} g_{\text{BF}} \rangle \right] \\ & \times e^{-h\nu/kT}. \end{aligned} \quad (55)$$

This expression can be evaluated to obtain the enhancement of the photon yield resulting from the increase in both $\langle Z^2 g_{\text{FF}} \rangle$ and $\langle Z^4 e^{(\chi - \Delta\chi)/kT} g_{\text{BF}} \rangle$ from CH shell–mix contamination. The CH mix does not affect the neutron yield, except possibly through increased radiative cooling since the $n_D n_T$ product of fuel ion densities product in Eq. (30) is only minutely affected by a trace contamination.

As was noted above, the Kulsrud Gaunt factor for hydrogen differs only slightly from the more reliable KL values for hydrogen in our relevant temperature range, but it is not applicable to carbon under ICF hot-spot conditions or to FB emission. Power-law fits to KL results have been obtained near $h\nu_0 \approx 5.39$ keV and $h\nu_0/kT \approx 2$ for the Gaunt factors needed to evaluate Eq. (55) (Ref. 19). These are

$$\begin{aligned} g_{\text{H,FF}} & \approx 0.966 (h\nu/kT)^{-0.41}, \\ g_{\text{H,FB}} & \approx 0.299 (h\nu/5.39 \text{ keV})^{-0.43}, \\ g_{\text{C,FF}} & \approx 1.28 (h\nu/kT)^{-0.23}, \\ g_{\text{C,FB}} & \approx 0.926 (h\nu/5.39 \text{ keV})^{-0.141}. \end{aligned} \quad (56)$$

The FF Gaunt factors depend on temperature because the FF absorption cross section is an average over the Maxwell–Boltzmann distribution of initial free-electron states. The FB Gaunt factors, on the other hand, do not depend on temperature because all properties of the single-electron bound states are attributes of the ion, not the free-electron plasma. We find that adding a fraction $f_{\text{CH}} = 2.4\%$ by atom of CH to a pure hydrogen core, as in the uniform mix of shell polymer into the hot spot, doubles the emissivity at $h\nu_0 \approx 5.39$ keV. This represents a mix mass of $\Delta M_{\text{CH}} = 125$ ng in the chosen example above where the hot-spot mass is $M_{\text{HS}} = 2.1$ μg , which happens to be the mean hot-spot mass of the entire ensemble of simulations considered above. The standard deviation of hot-spot masses in this ensemble is only 17%, so the emission-doubling mix

mass is roughly the same for all the implosions. The measured emission enhancements of the low-adiabat implosions plotted in Fig. 139.23 range over factors from 2 to 3, which correspond to a range of mix mass from 125 ng to 250 ng. The enhancement factor corresponding to a 2.4%-by-atom contamination level is shown plotted as the black curve in Fig. 139.24 as a function of temperature. Within the range of plausible hot-spot temperatures indicated by the blue-shaded region, $2 \text{ keV} < kT < 3 \text{ keV}$, the enhancement factor is a weak function of temperature, primarily the result of the temperature dependences of the relevant Gaunt factors listed in Eq. (56). The yield-ratio scaling index q , plotted as the red curve, varies with temperature in the contaminated core, as it does in the pure hydrogen core in Fig. 139.22, although much less so, because the Gaunt factors for the FB emission, which counts for very roughly half the emission in Fig. 139.24 and none of the emission in Fig. 139.22, do not depend on temperature. The black and red horizontal dashed lines show the enhancement factor (unity) and the index value (0.56) expected for zero contamination.

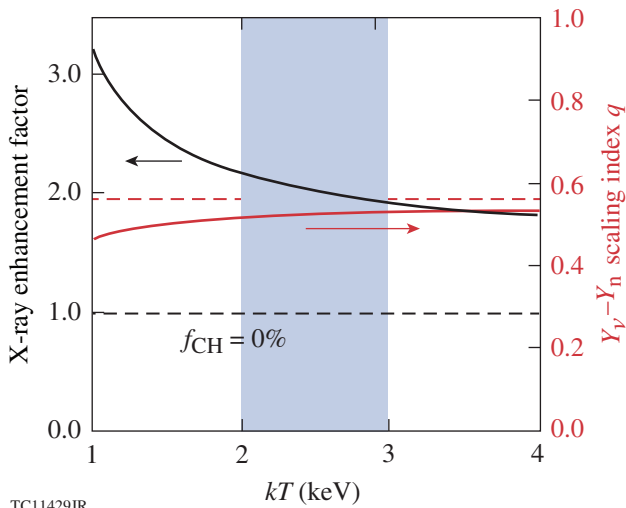


Figure 139.24

Photon-yield enhancement resulting from a contamination of the hot spot, as a function of temperature. The photon emissivity of a hot spot is expected to double when contaminated at a level of 2.4% by atoms of the CH shell material. This enhancement factor varies with hot-spot temperature, as shown by the black curve and the left-hand scale. The blue shading emphasizes the range of temperature from 2 to 3 keV—the plausible range of hot-spot temperatures. The red curve and right-hand scale show the scaling index q of the yield quotient Y_{ν_0}/Y_n^q as a function of temperature. The black and red horizontal dashed lines show the enhancement factor (unity) and the index value (0.56), respectively, expected for zero contamination.

A set of similar mix-mass measurements has been reported for cryogenic implosions on the NIF based on the ratio of the x-ray and neutron yields.¹³ To describe this technique in terms

of the discussion above, we write Eq. (28) once again, but with the mix effect included, as in Eq. (55),

$$Y_{\nu_0} \propto P^2 \frac{e^{-h\nu/kT}}{T^{2-\eta}} \left(\frac{\chi_H}{kT} \right)^{1/2} (1 + \langle Z \rangle) \times \left[\langle Z^2 g_{FF} \rangle + 2 \left(\frac{\chi_H}{kT} \right) \langle Z^4 e^{(\chi - \Delta\chi)/kT} g_{BF} \rangle \right] V \Delta t. \quad (57)$$

Our discussion parallels the discussion in Ref. 13 to some extent, although the mix-mass estimates presented in Ref. 13 are based ultimately on emissivity values obtained from detailed atomic calculations, rather than the Kramers–Gaunt formulation underlying Eq. (57). The ratio of the photon to neutron yield can be constructed from Eq. (30) and Eq. (57) with the result being

$$\frac{Y_{\nu_0}}{Y_n} \propto \frac{e^{-h\nu/kT}}{T^{4+\varepsilon-\eta}} \left(\frac{\chi_H}{kT} \right)^{1/2} (1 + \langle Z \rangle) \times \left[\langle Z^2 g_{FF} \rangle + 2 \left(\frac{\chi_H}{kT} \right) \langle Z^4 e^{(\chi - \Delta\chi)/kT} g_{BF} \rangle \right] \quad (58)$$

to within fixed constants. This is the quantity that was measured in the NIF experiments. In forming this ratio, the pressure factors, the hot-spot volumes, and the emission times cancel. It was assumed here as well that the temperature and neutron emission rate were spatially uniform, the electron and ion temperatures were equal, and the photon and neutron emission volumes and times were equal. Since OMEGA and non-igniting NIF implosions stagnate in comparable temperature ranges, we can examine this yield ratio in an approximate fashion by allowing $\eta = \varepsilon = 0$, and applying the Kulsrud limit $g_{FF} \propto T^{0.5}$ for both hydrogen and carbon and the same temperature independence for g_{BF} , which is a better approximation near $h\nu_0 = 10.85 \text{ keV}$ used in the NIF measurements than near $h\nu_0 = 5.30 \text{ keV}$ used in the OMEGA experiments. This gives

$$\frac{Y_{\nu_0}}{Y_n} \propto \frac{e^{-h\nu/kT}}{T^4} (1 + \langle Z \rangle) \left[\langle Z^2 \rangle + 2 \left(\frac{\chi_H}{kT} \right) \frac{g_{BF}}{g_{FF}} \langle Z^4 \rangle \right]. \quad (59)$$

The argument supporting the mix-mass estimates based on measurements of this yield ratio in the NIF experiments is that, according to an equation very much like Eq. (59), the yield ratio

is related directly to the charge averages and consequently to the mix atomic fractions:

$$\langle Z^n \rangle = 1 + (6^n - 1) \frac{f_{\text{CH}}}{2}. \quad (60)$$

Since the hydrogen and carbon are nearly fully ionized, the ion charges are effectively fixed, and everything else is a weak function of temperature.¹³ Based on the condition given by Eq. (19) for $n = 4$, the leading factor of Eq. (59) is independent of temperature for a range of temperatures centered at $kT_0 = h\nu_0/4$ or $kT_0 = 2.71$ keV, which is almost exactly the center of the range of temperatures, $1.7 \text{ keV} < kT < 3.9 \text{ keV}$ given in Ref. 13 as the range of applicable source temperatures. These NIF mix-mass measurements are another example of how taking x-ray measurements at an appropriate spectral energy simplifies their analysis in a very important way.

The contamination fractions measured on OMEGA at the level of $f_{\text{CH}} = 2.4\%$ to 4.8% are similar to the range of mix fractions measured on the NIF.¹³ Given the obvious dissimilarities between NIF indirect-drive implosions driven by two orders of magnitude more laser energy than the OMEGA direct-drive implosions, the similar mix fractions become an interesting point of comparison for future consideration. A few remarks will suffice for now. We note that the NIF capsules are roughly twice the diameter of the OMEGA capsules.³⁵ Assuming naively that all characteristic lengths and times of an implosion scale in direct proportion to the initial capsule radius, i.e., if the experiments on the two platforms were self-similar versions of each other, then the material composition profiles should be self-similar as well. Comparable mix fractions would result from shell perturbation amplitudes growing to comparable fractions of the capsule radius. For spherical-harmonic perturbation modes of the same harmonic order, the perturbation wavelengths scale with radius. The saturation amplitude, which is the point where linear perturbation growth transitions to nonlinear growth and, perhaps, turbulent mix, occurs at a specific ratio of amplitude to wavelength.³⁶ Since both the wavelengths and the amplitudes scale in direct proportion to the capsule radius, the transition to turbulence should be self-similar in both series of implosions. No doubt, this self-similarity does not apply to all aspects of an implosion.⁴ If mix is regarded as a surface phenomenon, comparable mix masses per volume indicate roughly twice the mix mass per shell area in the NIF capsules than in the OMEGA targets since the former have roughly twice the volume-to-surface-area ratio as the latter. These tentative remarks do not identify which series of implosions was more unstable or which of the two mix fractions is larger, relative to

expected performance, but it is clear that mix measurements are now possible and experimental progress in addressing these and other questions can be expected in the future.

Conclusions

The scaling behavior of the x-ray emissivity of hydrogen hot spots in ICF implosions has been examined. Using the pressure- and temperature-dependence of x-ray continuum emission, we have shown that the pressure can be inferred from the emissivity measured within a specific spectral energy range without requiring accurate prior knowledge of the source temperature. This is significant because the pressure is the single most important parameter that characterizes an isobaric hot spot; it is a key measure of the scaled-equivalent ignition performance of an implosion; and it is an example of how quantities can be measured in direct or advantageous ways with spectral responses that have been optimized to the task.

The scaling relationship between the photon and neutron yields of OMEGA cryogenic implosions that has been observed in simulation results and used to isolate excess x-ray emission from low-adiabat implosions has been explained. We have brought together x-ray emission and neutron yield scaling results to produce the first estimates of the fuel-shell mix mass in OMEGA implosions. The scaling properties of both the x-ray emissivity at the chosen spectral energy and the neutron yield allow one to normalize the x-ray emission with respect to the scaled neutron yield so that excess normalized emission becomes a measure of the CH polymer mass from the shell that has mixed into the hot spot during the implosion, up to the time of stagnation. It is a matter of some interest that this neutron-photon scaling, which has gone unexplained in the past, is now understood. It is of particular interest to the progress of cryogenic implosion research on the OMEGA Laser System that we have estimates of the mix mass. In a number of important respects, this approach to mix-mass estimation is similar to that of the x-ray continuum-based mix-mass measurements on the NIF. It is interesting that both sets of measurements describe similar levels of mix contamination, the implications of which will be interesting to consider in the future.

ACKNOWLEDGMENT

This material is based upon work supported by the Department of Energy National Nuclear Security Administration under Award Number DE-NA0001944, the University of Rochester, the New York State Energy Research and Development Authority, and the Office of Fusion Energy Sciences Number DE-FG02-04ER54786. The support of DOE does not constitute an endorsement by DOE of the views expressed in this article.

REFERENCES

1. J. Nuckolls *et al.*, *Nature* **239**, 139 (1972).
2. J. D. Lindl, *Phys. Plasmas* **2**, 3933 (1995); J. D. Lindl *et al.*, *Phys. Plasmas* **11**, 339 (2004).
3. S. Atzeni and J. Meyer-ter-Vehn, *The Physics of Inertial Fusion: Beam Plasma Interaction, Hydrodynamics, Hot Dense Matter*, International Series of Monographs on Physics (Clarendon Press, Oxford, 2004).
4. R. Nora, R. Betti, K. S. Anderson, A. Shvydky, A. Bose, K. M. Woo, A. R. Christopherson, J. A. Marozas, T. J. B. Collins, P. B. Radha, S. X. Hu, R. Epstein, F. J. Marshall, R. L. McCrory, T. C. Sangster, and D. D. Meyerhofer, *Phys. Plasmas* **21**, 056316 (2014).
5. V. N. Goncharov, T. C. Sangster, R. Betti, T. R. Boehly, M. J. Bonino, T. J. B. Collins, R. S. Craxton, J. A. Delettrez, D. H. Edgell, R. Epstein, R. K. Follet, C. J. Forrest, D. H. Froula, V. Yu. Glebov, D. R. Harding, R. J. Henchen, S. X. Hu, I. V. Igumenshchev, R. Janezic, J. H. Kelly, T. J. Kessler, T. Z. Kosc, S. J. Loucks, J. A. Marozas, F. J. Marshall, A. V. Maximov, R. L. McCrory, P. W. McKenty, D. D. Meyerhofer, D. T. Michel, J. F. Myatt, R. Nora, P. B. Radha, S. P. Regan, W. Seka, W. T. Shmayda, R. W. Short, A. Shvydky, S. Skupsky, C. Stoeckl, B. Yaakobi, J. A. Frenje, M. Gatu-Johnson, R. D. Petrasso, and D. T. Casey, *Phys. Plasmas* **21**, 056315 (2014).
6. J. D. Lawson, *Proc. Phys. Soc. Lond. B* **70**, 6 (1957).
7. R. Betti, P. Y. Chang, B. K. Spears, K. S. Anderson, J. Edwards, M. Fatenejad, J. D. Lindl, R. L. McCrory, R. Nora, and D. Shvarts, *Phys. Plasmas* **17**, 058102 (2010).
8. T. R. Boehly, D. L. Brown, R. S. Craxton, R. L. Keck, J. P. Knauer, J. H. Kelly, T. J. Kessler, S. A. Kumpan, S. J. Loucks, S. A. Letzring, F. J. Marshall, R. L. McCrory, S. F. B. Morse, W. Seka, J. M. Soares, and C. P. Verdon, *Opt. Commun.* **133**, 495 (1997).
9. H. R. Griem, *Principles of Plasma Spectroscopy* (Cambridge University Press, Cambridge, England, 1997).
10. S. Yu. Gus'kov, O. N. Krokhin, and V. B. Rozanov, *Nucl. Fusion* **16**, 957 (1976).
11. R. Betti, M. Umansky, V. Lobatchev, V. N. Goncharov, and R. L. McCrory, *Phys. Plasmas* **8**, 5257 (2001).
12. W. J. Hogan, E. I. Moses, B. E. Warner, M. S. Sorem, and J. M. Soares, *Nucl. Fusion* **41**, 567 (2001); G. H. Miller, E. I. Moses, and C. R. Wuest, *Opt. Eng.* **43**, 2841 (2004).
13. T. Ma, P. K. Patel, N. Izumi, P. T. Springer, M. H. Key, L. J. Atherton, L. R. Benedetti, D. K. Bradley, D. A. Callahan, P. M. Celliers, C. J. Cerjan, D. S. Clark, E. L. Dewald, S. N. Dixit, T. Döppner, D. H. Edgell, R. Epstein, S. Glenn, G. Grim, S. W. Haan, B. A. Hammel, D. Hicks, W. W. Hsing, O. S. Jones, S. F. Khan, J. D. Kirkenny, J. L. Kline, G. A. Kyrala, O. L. Landen, S. Le Pape, B. J. MacGowan, A. J. Mackinnon, A. G. MacPhee, N. B. Meezan, J. D. Moody, A. Pak, T. Parham, H.-S. Park, J. E. Ralph, S. P. Regan, B. A. Remington, H. F. Robey, J. S. Ross, B. K. Spears, V. Smalyuk, L. J. Suter, R. Tommasini, R. P. Town, S. V. Weber, J. D. Lindl, M. J. Edwards, S. H. Glenzer, and E. I. Moses, *Phys. Rev. Lett.* **111**, 085004 (2013).
14. S. Chandrasekhar, *Radiative Transfer* (Dover Publications, New York, 1960).
15. R. N. Bracewell, *The Fourier Transform and Its Applications*, 3rd ed. (McGraw-Hill, Boston, 2000).
16. H. A. Kramers, *Philos. Mag.* **46**, 836 (1923).
17. J. A. Gaunt, *Proc. R. Soc. Lond. A* **126**, 654 (1930).
18. A. Messiah, *Quantum Mechanics*, Vol. II (North-Holland, Amsterdam, 1966), p. 644.
19. W. J. Karzas and R. Latter, *Astrophys. J. Suppl. Ser.* **6**, 167 (1961).
20. M. Nakagawa, Y. Kohyama, and N. Itoh, *Astrophys. J. Suppl. Ser.* **63**, 661 (1987).
21. F. Perrot, *Laser Part. Beams* **14**, 731 (1996); V. N. Tsytovich *et al.*, *J. Quant. Spectrosc. Radiat. Transf.* **57**, 241 (1997).
22. A. N. Cox, in *Stars and Stellar Systems*, edited by L. H. Aller and D. B. McLaughlin, *Stellar Structure*, Vol. VIII, edited by G. P. Kuiper and B. M. Middlehurst (The University of Chicago Press, Chicago, 1965), pp. 195–268.
23. B. F. Rozsnyai, *Phys. Rev. A* **43**, 3035 (1991); S. Mazevet *et al.*, *Astron. Astrophys.* **405**, L5 (2003).
24. S. X. Hu, L. A. Collins, T. R. Boehly, J. D. Kress, V. N. Goncharov, and S. Skupsky, *Phys. Rev. E* **89**, 043105 (2014).
25. R. M. Kulsrud, *Astrophys. J.* **119**, 386 (1954).
26. F. J. Marshall and J. A. Oertel, *Rev. Sci. Instrum.* **68**, 735 (1997).
27. T. C. Sangster, V. N. Goncharov, R. Betti, P. B. Radha, T. R. Boehly, D. T. Casey, T. J. B. Collins, R. S. Craxton, J. A. Delettrez, D. H. Edgell, R. Epstein, C. J. Forrest, J. A. Frenje, D. H. Froula, M. Gatu-Johnson, V. Yu. Glebov, D. R. Harding, M. Hohenberger, S. X. Hu, I. V. Igumenshchev, R. Janezic, J. H. Kelly, T. J. Kessler, C. Kingsley, T. Z. Kosc, J. P. Knauer, S. J. Loucks, J. A. Marozas, F. J. Marshall, A. V. Maximov, R. L. McCrory, P. W. McKenty, D. D. Meyerhofer, D. T. Michel, J. F. Myatt, R. D. Petrasso, S. P. Regan, W. Seka, W. T. Shmayda, R. W. Short, A. Shvydky, S. Skupsky, J. M. Soares, C. Stoeckl, W. Theobald, V. Versteeg, B. Yaakobi, and J. D. Zuegel, *Phys. Plasmas* **20**, 056317 (2013).
28. Delettrez, R. Epstein, M. C. Richardson, P. A. Jaanimagi, and B. L. Henke, *Phys. Rev. A* **36**, 3926 (1987).
29. J. J. MacFarlane *et al.*, *High Energy Density Phys.* **3**, 181 (2007); Prism Computational Sciences, Inc., Madison, WI 53711.

30. G. A. Kyrala *et al.*, *Rev. Sci. Instrum.* **81**, 10E316 (2010); M. A. Barrios, S. P. Regan, L. J. Suter, S. Glenn, L. R. Benedetti, D. K. Bradley, G. W. Collins, R. Epstein, B. A. Hammel, G. A. Kyrala, N. Izumi, T. Ma, H. Scott, and V. A. Smalyuk, *Phys. Plasmas* **20**, 072706 (2013).
31. H.-S. Bosch and G. M. Hale, *Nucl. Fusion* **32**, 611 (1992).
32. C. D. Zhou and R. Betti, *Phys. Plasmas* **14**, 072703 (2007).
33. Lord Rayleigh, *Proc. London Math Soc.* **XIV**, 170 (1883); G. Taylor, *Proc. R. Soc. London Ser. A* **201**, 192 (1950); S. Chandrasekhar, in *Hydrodynamic and Hydromagnetic Stability*, International Series of Monographs on Physics (Clarendon Press, Oxford, 1961), Sec. 10.
34. J. C. Stewart and K. D. Pyatt, Jr., *Astrophys. J.* **144**, 1203 (1966).
35. S. W. Haan, J. D. Lindl, D. A. Callahan, D. S. Clark, J. D. Salmonson, B. A. Hammel, L. J. Atherton, R. C. Cook, M. J. Edwards, S. Glenzer, A. V. Hamza, S. P. Hatchett, M. C. Herrmann, D. E. Hinkel, D. D. Ho, H. Huang, O. S. Jones, J. Kline, G. Kyrala, O. L. Landen, B. J. MacGowan, M. M. Marinak, D. D. Meyerhofer, J. L. Milovich, K. A. Moreno, E. I. Moses, D. H. Munro, A. Nikroo, R. E. Olson, K. Peterson, S. M. Pollaine, J. E. Ralph, H. F. Robey, B. K. Spears, P. T. Springer, L. J. Suter, C. A. Thomas, R. P. Town, R. Vesey, S. V. Weber, H. L. Wilkens, and D. C. Wilson, *Phys. Plasmas* **18**, 051001 (2011).
36. S. W. Haan, *Phys. Fluids B* **3**, 2349 (1991).

Soft X-Ray Backlighting of Cryogenic Implosions Using a Narrowband Crystal Imaging System

Introduction

Backlighting is a powerful technique used to observe the flow of dense and relatively cold material in high-energy-density-plasma experiments. This technique has been used successfully in both direct-¹ and indirect-drive² inertial confinement fusion implosion experiments to measure the velocity and uniformity of the imploding shell. High-performance, direct-drive cryogenic deuterium–tritium (DT) implosions³ are a challenging backlighting configuration because of the low opacity of the DT shell, the high shell velocity, the small size of the stagnating shell, and the very bright self-emission of the hot core. A relatively low backlighter photon energy of <2 keV is required to obtain an observable contrast of the backlit images. At a maximum speed of up to $400 \mu\text{m/ns}$, backlighting with a nano-second laser pulse and a conventional x-ray framing camera⁴ with an ~ 40 -ps temporal resolution would lead to an ~ 20 - μm motion blurring of the order of the shell's in-flight thickness. For high-performance DT implosions on OMEGA,⁵ the size of the hot spot is typically $\sim 20 \mu\text{m}$, the temperature >3 keV, and the emission time of the order of 100 ps (Ref. 6), which generates extremely bright self-emission.

A crystal imaging system with a backlighter driven by a short-pulse, high-energy petawatt (HEPW) laser such as OMEGA EP⁷ is well suited for backlighting cryogenic DT implosions because of its narrow spectral width, high-throughput, high spatial resolution of the imager, and short emission time and high brightness of the backlighter. Early proof-of-principle experiments on OMEGA using a crystal imaging system and a backlighter driven by the OMEGA EP short pulse⁸ laser were performed using room-temperature CH targets. These experiments showed encouraging results with the backlighter intensity within a factor of 2 of the time-integrated core emission and a signal-to-background ratio of >10 . The initial data indicated that significant improvements were required in the setup to be able to backlight cryogenic DT targets. The images showed significant astigmatism, which must be reduced. The self-emission of a DT cryo target is orders of magnitude larger compared to a CH target because of the much lower opacity, which requires a time-gated detection

system. The backlighter target must be close to the primary target (~ 5 mm) to achieve the required brightness, which is not compatible with the cryogenic shroud setup on OMEGA.⁹

This article describes the setup of a crystal imaging system for cryogenic DT implosions on OMEGA based on the design presented in Ref. 8. Three major improvements have been implemented: (1) the x-ray reflecting crystal has been mounted on an aspheric substrate to reduce the astigmatism; (2) a time-gated detector has been implemented to record the image; and (3) a fast target-insertion system has been built to insert the backlighter target close to the implosion target within 100 ms after the cryogenic shroud has been removed. The backlighter target material was changed from Si-coated Al foils to pure Si wafers, and the CH filters were replaced with Be filters to increase the brightness of the backlighter and the transmission of the imaging system.

Setup of the Crystal Imaging System

The cryogenic backlighting system uses the Si He_α line at ~ 1.865 keV (0.664 nm) from a Si backlighter driven by the OMEGA EP laser (see Fig. 139.25). The backlighter target is a $500\text{-}\mu\text{m-sq} \times 10\text{-}\mu\text{m}$ -thick silicon wafer placed 5 mm from the primary target. A 25-mm-diam quartz crystal, cut

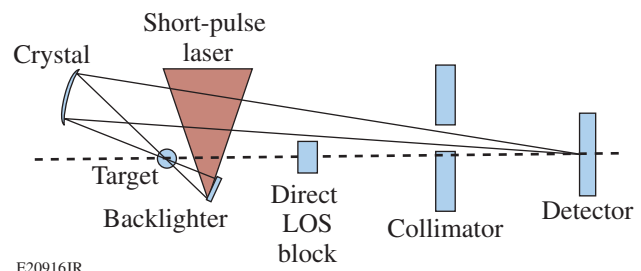


Figure 139.25

Schematic of the spherical crystal imager backlighting setup (not to scale). The short-pulse laser illuminates a backlighter foil behind the primary target, which is heated by 60 beams from the OMEGA laser (not shown). A direct line-of-sight (LOS) block and a collimator protect the detector from background x rays emitted by the backlighter and primary targets.

along the 1011 planes with a $2d$ spacing of 0.6687 nm, is set up so that the x rays from the backlighter are incident on the crystal at 83.9° from the surface—the Bragg angle for the Si He $_{\alpha}$ line. The crystal is bonded by INRAD¹⁰ to a substrate with a 500-mm major radius of curvature by optical contact. It is placed 267 mm from the implosion target. The image is recorded on a detector located ~ 3.65 m from the target at a magnification of $\sim 15\times$. A direct line-of-sight (LOS) block and a collimator are used to protect the detector from background x rays emitted by the backlighter and the primary targets. A 12.5- μm -thick Be foil is used as a blast shield in front of the crystal, and a second 12.5- μm -thick Be foil acts as a light-tight filter in front of the detector. The Be foil in front of the crystal is backed with a stainless-steel mesh to increase its mechanical stability. This system is described in more detail in Ref. 8.

1. Astigmatism-Corrected Crystal Substrates

An aspheric substrate was designed to reduce the optical aberrations of the imager seen in the previous experiments,⁸ which are predominantly astigmatism. The deviation from a spherical surface was described in polynomial form (only the five leading terms are shown):

$$z = \frac{x^2 + y^2}{r} \frac{1}{1 + \sqrt{1 - \frac{x^2 + y^2}{r^2}}} + y^2 A_{2,2} + x^2 A_{2,0} + x^2 y A_{3,1} + y^3 A_{3,3} + x^4 A_{4,0}.$$

A ray-tracing software (*FRED*)¹¹ was used to optimize the coefficients for the smallest spot size. The ray-tracing software was set up to use the rocking curve of the crystal as an additional constraint. The width of the rocking curve was set to be $2\times$ the vendor specification of 12 arcsec. The optimized coefficients are listed in Table 139.I. The calculated point-spread func-

Table 139.I: Polynomial coefficients for the optimized aspherical substrate.

i	j	A_{ij}	Polynomial
2	0	8.682×10^{-8}	X^2
2	2	1.140×10^{-5}	Y^2
3	1	-1.545×10^{-7}	X^2Y
3	3	-1.131×10^{-7}	Y^3
4	0	5.372×10^{-10}	X^4

tion (PSF) for this design has a full width at half maximum (FWHM) of $\sim 0.5 \mu\text{m}$ in the horizontal direction and $\sim 2 \mu\text{m}$ in the vertical direction (see Fig. 139.26). While it is theoretically possible to calculate a surface prescription that produces a spot with submicron spatial resolution on axis, the polynomial was truncated to stay within the capabilities of the manufacturing process. The substrate was manufactured by QED Technologies¹² to a figure error of 25-nm peak-to-valley and 2-nm root mean square (rms).

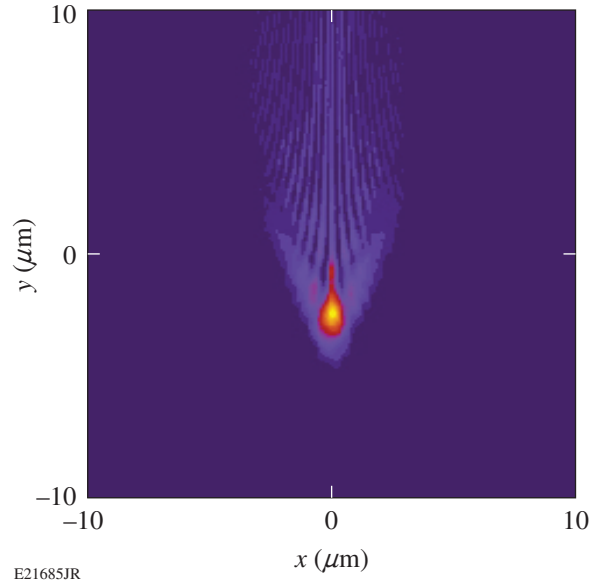


Figure 139.26 Point-spread function (PSF) of the imaging system with an optimized substrate as calculated by *FRED*.

2. Time-Gated Detector

To reduce the impact of the self-emission of the hot core of the cryo DT implosion, the time-integrated image-plate (IP) detector described in Ref. 8 was replaced by the head of an x-ray framing camera (XRFC)⁴ (see Fig. 139.27). The XRFC head was attached at the back of a ten-inch manipulator (TIM-4) with an adapter flange. Slots were cut in the collimator holder to pump out the volume where the microchannel plate (MCP) of the XRFC head operates. A vacuum gauge was used to interlock the high-voltage system of the XRFC head to prevent discharges. The Be filter used to block the UV light from the laser was mounted behind the collimator. The XRFC head was run with a single-strip MCP detector, fed by a 300- to 500-ps-long high-voltage pulse. The image is recorded on film. The spatial resolution of the XRFC recording system is typically ~ 20 lp/mm (Ref. 13).

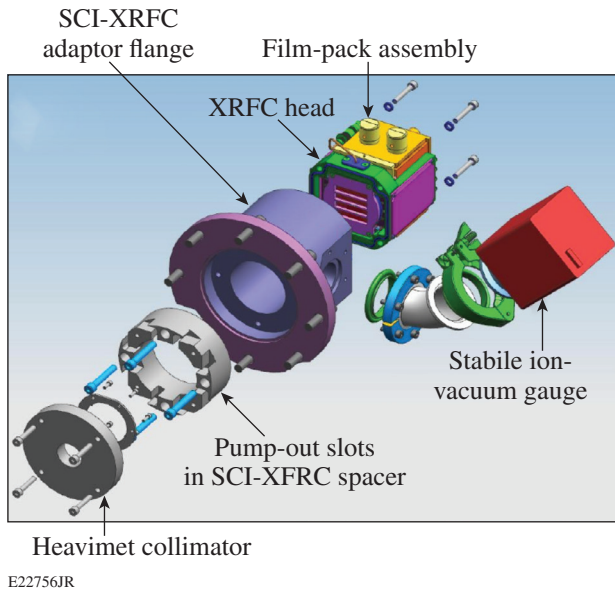


Figure 139.27
CAD model of the x-ray framing-camera setup. SCI-XRFC: spherical crystal imaging x-ray framing camera.

3. Fast Target Inserter

Given the available energy of the short-pulse laser system, the backlighter target must be positioned close to the cryo target to maximize the brightness of the backlighter emission. Previous experiments⁸ have shown that with a distance of 5 mm for the backlighter target, adequate brightness and backlighter uniformity can be achieved. Unfortunately, this backlighter location is inside the cryogenic shroud system, which protects the cryogenic DT target, being held at a temperature of <20 K,

from ambient thermal radiation.⁹ It is impossible to mount the backlighter target on the same support structure as the cryo target since it would distort the uniformity of the isotherms inside the layering sphere, which is essential for obtaining high-quality DT ice layers. A fast target positioner (FASTPOS) was designed to insert the backlighter target after the cryogenic shroud was removed, immediately before the target shot. The timing of the shroud removal leaves an ~100-ms window to insert the backlighter. Given the shroud diameter of ~100 mm and a clearance requirement of ~25 mm around the shroud for the fast retraction operation, a travel distance of ~80 mm is required [see Fig. 139.28(a)].

The design of FASTPOS is based on a commercially available linear actuator from LINMOT¹⁴ [see Fig. 139.28(b)]. This motor is capable of a peak force of ~70 N, providing an acceleration of >10 g, with a moving mass of ~120 g. This actuator was set up in a mounting system with aluminum extensions for the slider, polymer bushings to provide a radial constraint, and a pin-in-slot system to provide a rotational constraint. A Micro-E optical encoder provides high-resolution feedback for a closed-loop control system. Special care was taken to provide a low-resistance ground path for the return current generated by the short-pulse laser interacting with the backlighter target. Extensive tests have shown that the FASTPOS system can insert targets over a distance of ~80 mm, with a final positioning accuracy of <50 μm in ~70 ms. It is very resilient to the electromagnetic interference caused by the short-pulse laser. The instrument performed well and without issues even at the highest laser energies of 1.25 kJ.

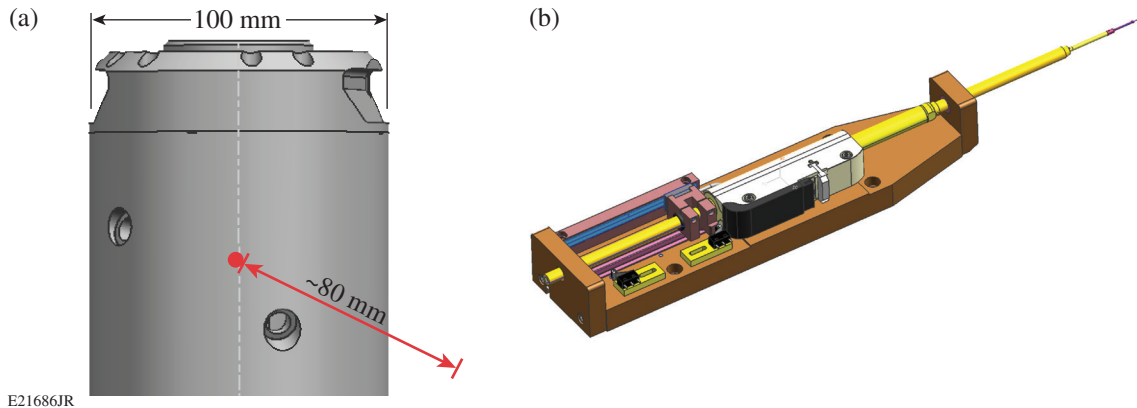


Figure 139.28
(a) Illustration of the path of the backlighter target starting outside the cryo shroud to ~5 mm from the cryo target; (b) CAD drawing of the setup of the fast target positioner (FASTPOS).

Experimental Data

The first experiments with the aberration-corrected cryo-compatible Si He $_{\alpha}$ spherical crystal imaging (SCI) system were performed using both room-temperature plastic (CH) shells and DT cryogenic targets. Both targets had an 860- μm outer diameter. The CH shells had 27- μm -thick walls, roughly mass equivalent to the cryo DT targets, which had an ~ 7.5 - μm CD outer shell and an ~ 60 - μm -thick DT ice layer. The targets were imploded using ~ 20 kJ of UV (351-nm) laser light with an ~ 2 - to 3-ns-long highly shaped laser pulse.³ The backlighter target was made out of a 10- μm -thick Si wafer. The OMEGA EP short-pulse laser illuminated the backlighter foils at an $\sim 45^\circ$ angle of incidence and focused to an ~ 350 - μm focal spot, corresponding to an average intensity of $\sim 1 \times 10^{17}$ W/cm² at 1.25-kJ energy and a 10-ps pulse duration. The OMEGA EP short-pulse laser was fired at various delays of 2 to 3 ns after the start of the OMEGA UV pulse.

1. Gated Imager

A backlit image of (a) a time-integrated cryo DT implosion recorded on an image plate and (b) a time-gated self-emission image recorded on the XRFC are compared in Fig. 139.29. Both images show the emission of the SiC stalk at the bottom of the image that holds the shell. The stalk is irradiated by some of the laser energy that drives the target and emits the same Si He $_{\alpha}$ radiation as the backlighter. The time-integrated image shows an extremely bright emission peak from the implosion core and a very faint record of the backlighter emission. The core emission saturated the detector and is significantly more than 10 \times brighter than the backlighter. The time-gated image was recorded without a backlighter using an ~ 500 -ps-long electri-

cal gate pulse. The gate pulse was timed to avoid the emission of the core. The image is dominated by the emission from the shell as it is heated by the UV laser. It shows only a very faint signal from the core in the center of the shell, demonstrating the very high extinction ratio of the gated recording system.

2. Performance of the Crystal Imager

Figure 139.30(a) shows a time-gated backlit image from an implosion experiment with a mass-equivalent CH target taken between the end of the drive laser pulse and the start of the self-emission at peak compression. The gate of the XRFC was set to ~ 300 ps. The emission from the SiC stalk is seen at the bottom of the image. A “shadow” from the highly opaque compressed CH shell is seen in front of the emission from the Si backlighter. Since the gate time was set to start after the end of the laser pulse, no signal from the shell self-emission is visible.

A “cusp”-like feature in the absorption at the bottom of the shadow shows the effect of the stalk and the glue, with which it is attached to the shell, on the implosion dynamics. A second faint absorption feature close to the top of the target image is most likely caused by a piece of debris on the outer shell. This image shows the high optical quality of the improved imaging system; the astigmatism seen in previous experiments is fully corrected. A vertical lineout [Fig. 139.30(b)] is used for a detailed comparison between the measured signal and post-processed one-dimensional (1-D) simulation. The measurements compare very favorably with the simulation in the parts of the shell not influenced by the stalk (top of the target, right side in lineout), showing that the resolution of the imager is good enough to capture the dominant features of the implosion. The

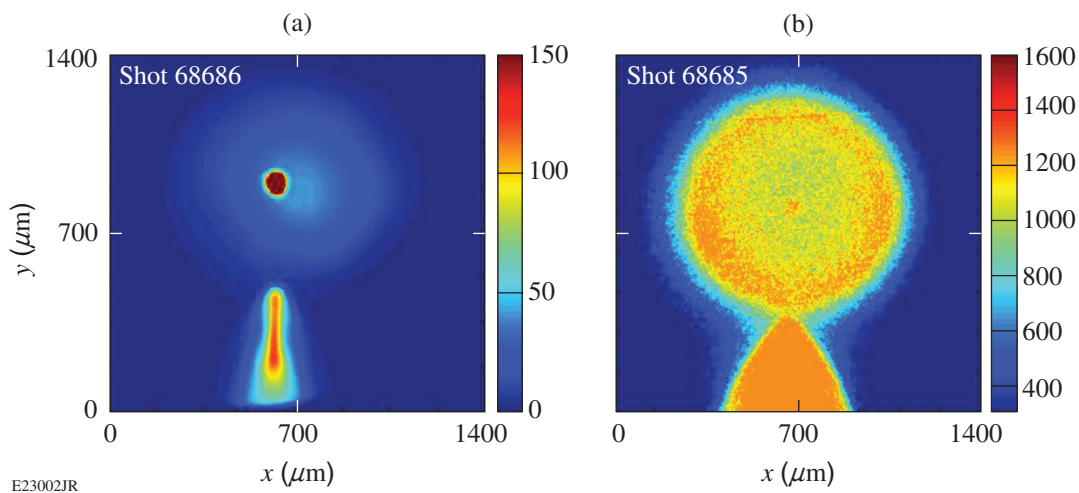
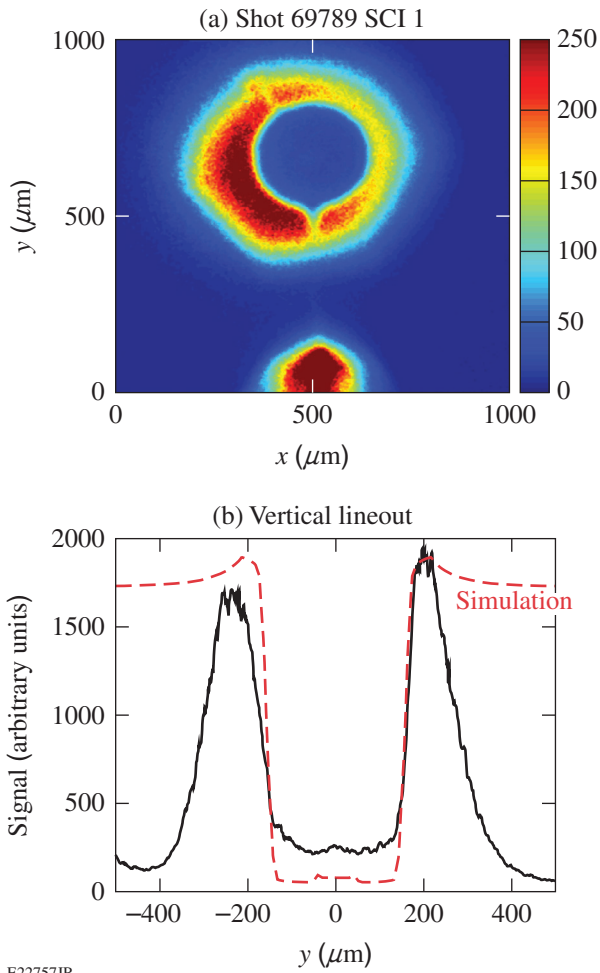


Figure 139.29

(a) Time-integrated image of a backlit DT cryo implosion recorded on an image plate; (b) time-gated image of the self-emission from a DT cryo implosion.



E22757JR

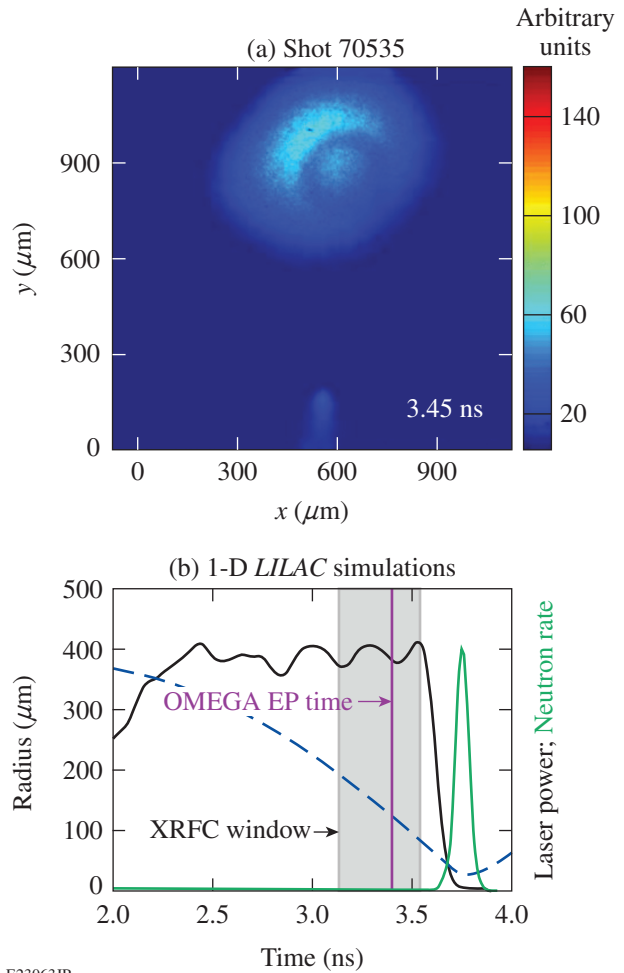
Figure 139.30 (a) Time-gated backlit image from a mass-equivalent CH implosion experiment; (b) vertical lineout through the backlit image.

effect of the stalk is clearly visible in the lineout. More-involved two- (2-D) or three-dimensional (3-D) simulations are required for a detailed analysis of the stalk and debris effects. Shots with a static resolution target in place of the primary target and only the backlighter pulse indicate that the spatial resolution of the imager is $\sim 10 \mu\text{m}$ at 10% modulation, which is significantly more than the expected resolution of a few microns.

3. Backlit Cryogenic Targets

As expected, the images from cryogenic DT targets show significantly less contrast compared to the mass-equivalent CH targets [see Fig. 139.31(a)]. A 300-ps gate was used in these experiments to minimize the contribution from self-emission. The gate was timed to start ~ 500 ps before the time of peak core emission [see Fig. 139.31(b)]. The OMEGA EP short-pulse laser was fired ~ 100 ps before the end of the gate at a time when the shell assembly was compressed to a radius of

$\sim 120 \mu\text{m}$. The image shows a faint record of the self-emission of the SiC stalk at the bottom of the target. The shadowgraph of the imploded shell is slightly offset from the center of the backlighter, illustrating the difficulties in aligning the crystal, primary target, and backlighter on a common line of sight. No indication of the self-emission from the shell is seen in the image, showing that the brightness of the backlighter and the narrow spectral acceptance of the imaging system are sufficient to suppress this background source. No bright emission from the core is seen in the center of the absorption feature, demonstrating again that the extinction of the gated imager is good enough to obtain high-quality data.



E23063JR

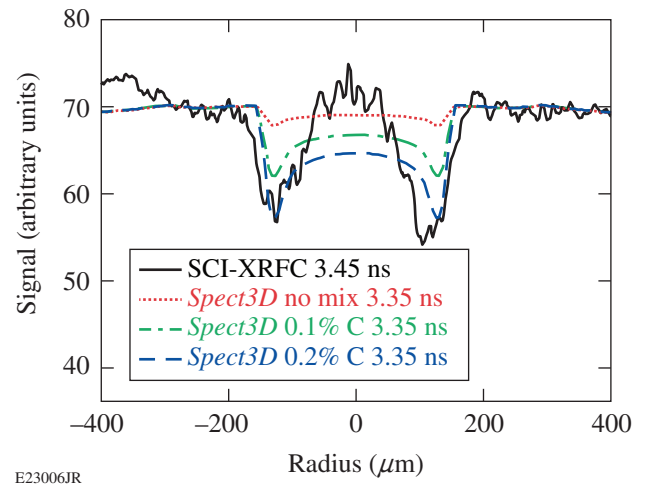
Figure 139.31 (a) Time-gated image of a backlit DT cryogenic implosion. (b) Temporal evolution of the shell radius center (blue) compared to the temporal history of the laser power and neutron-production rate from 1-D *LILAC* simulations for the shot shown in (a). The exposure timing of the XRFC is indicated by the gray-shaded area; the arrival time of the OMEGA EP short-pulse laser is indicated by the purple vertical line.

Image Analysis and Interpretation

To measure the absorption in the compressed shell and quantitatively compare the signal recorded by the crystal imager with simulations, the data must be corrected for the backlighter shape. A simple first-order physical model was constructed to describe the shape of the backlighter by assuming a constant brightness source [see Fig. 139.32(a)]. This source was convolved with a Gaussian PSF, representing the spatial resolution of the imaging system at a 5-mm defocus [Fig. 139.32(b)]. The brightness and extent of the source and the width of the PSF were varied to obtain a best fit to the shape of the measured signal outside the area affected by the absorption of the target. This simple model fits the measured data quite well [see Fig. 139.32(c)].

Figure 139.33 shows a lineout through the image of shot 70535 corrected for the backlighter shape. For comparison, the result from a 1-D *LILAC*¹⁵ hydrocode simulation, post-processed with the radiation transport code *Spect3D*,¹⁶ is plotted (red dotted line). The backlighter timing had to be shifted by ~ 100 ps earlier to match the measured size of the absorption feature, indicating that the implosion is slightly delayed compared to the simulations.⁶ The measured absorption is seen to be much higher than the absorption calculated from the simulations. One possible explanation for this discrepancy is the Rayleigh–Taylor mixing of carbon from the outer CD shell into the DT ice during the shell acceleration. Adding a small amount of carbon uniformly into the shell in the *Spect3D* post-processor¹⁶ [0.1% C (green dashed–dotted line), 0.2% C (blue dashed line)] significantly increases the absorption in the model and brings the simulation much closer to the experimental data, especially in the areas of highest absorption corresponding to the dense shell. In the center of the image the calculated absorption with carbon mixing is higher than observed. This could either be caused by a small amount of self-emission, which is not fully

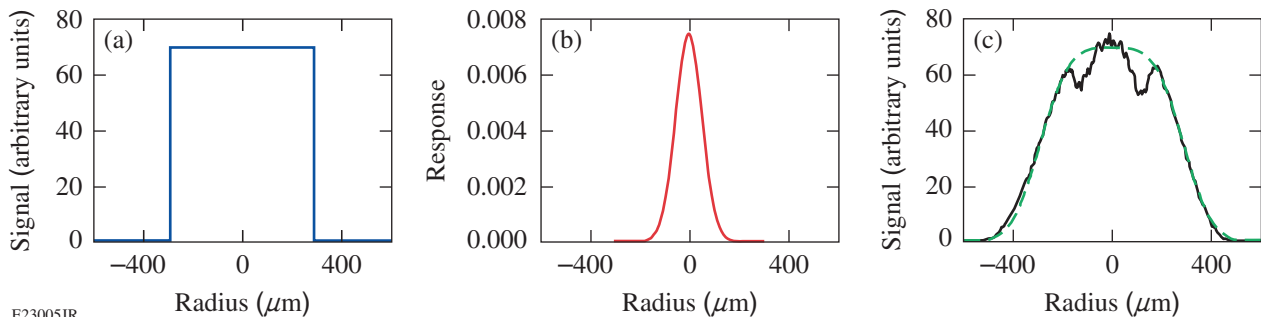
suppressed by the gating, or be indicative of 3-D effects, like the presence of the nonlinear phase of the Rayleigh–Taylor instability, where large bubbles of the light material (DT) separate thin spikes of the heavy material (carbon). An imaging system with limited resolution looking radially (center of the image) will mostly observe the low absorption of the DT bubbles. At the position of the dense shell, the line of sight of the imager will be predominantly perpendicular to the bubbles and spikes; consequently, the absorption will be influenced more by the high opacity of the carbon spikes. Another possible explanation of the higher-than-predicted absorption could be uncertainties in the opacity models. Further experiments are necessary to separate these issues and more fully understand the measured data.



E23006JR

Figure 139.33

Lineout through the backlit image of shot 70535 corrected for the shape of the backlighter emission (black solid line) compared to *Spect3D* post-processed 1-D *LILAC* simulations with varying levels of carbon mixed into the DT shell.



E23005JR

Figure 139.32

(A) A uniform source distribution is convolved with (b) a Gaussian PSF (c) to fit (green line) the measured shape (black line) of the backlighter lineout.

Summary and Outlook

A crystal imaging system capable of backlighting cryogenic implosions using the Si He α line at ~ 1.865 keV has been developed on the OMEGA Laser System. Three major improvements were implemented on the previous setup used for proof-of-principle experiments with room-temperature CH targets:⁸ (1) The Bragg crystal was bonded to an aspherically shaped substrate, significantly reducing the optical aberrations. (2) A time-gated detector was set up using the head of an XRFC. The background from the very bright emission of the implosion core prominently seen in previous time-integrated experiments was almost completely eliminated. (3) A fast target-insertion system was set up, capable of inserting the backlighter target ~ 80 mm in < 100 ms, which made it possible to perform experiments with a backlighter very close to the cryogenic target (~ 5 mm) without any modification to the cryogenic layering system, which could have compromised the quality of the DT ice layer.

High-quality backlit images were recorded with this system on cryogenic DT implosions. A simple procedure to correct for the shape of the backlighter based on a physical model of the imager was developed and applied to lineouts from the images. The corrected lineout shows significantly more absorption than a post-processed 1-D hydro simulation of the experiment, which could be an indication of carbon mixing deep into the DT ice layer during the acceleration phase of the implosion.

The resolution of the imaging system is adequate to resolve the spatial structures seen in cryogenic implosions ~ 200 ps before peak compression, but it might be a limiting factor closer to peak compression, where the spatial scales are compressed by a factor of ~ 3 . The discrepancy between measured and calculated resolution will be studied in offline experiments to explore the causes and potential remedies for this issue.

The description of the backlighter shape could be improved with a higher-order physical model, like the one based on a Taylor expansion,² or a decomposition in sinusoidal modes.

ACKNOWLEDGMENT

This material is based upon work supported by the Department of Energy National Nuclear Security Administration under Award Number DE-NA0001944, the University of Rochester, and the New York State Energy Research and Development Authority. The support of DOE does not constitute an endorsement by DOE of the views expressed in this article.

REFERENCES

1. P. B. Radha, F. J. Marshall, J. A. Marozas, A. Shvydki, I. Gabalski, T. R. Boehly, T. J. B. Collins, R. S. Craxton, D. H. Edgell, R. Epstein,

- J. A. Frenje, D. H. Froula, V. N. Goncharov, M. Hohenberger, R. L. McCrory, P. W. McKenty, D. D. Meyerhofer, R. D. Petrasso, T. C. Sangster, and S. Skupsky, *Phys. Plasmas* **20**, 056306 (2013).
2. D. G. Hicks *et al.*, *Phys. Plasmas* **17**, 102703 (2010).
3. T. C. Sangster, V. N. Goncharov, R. Betti, T. R. Boehly, D. T. Casey, T. J. B. Collins, R. S. Craxton, J. A. Delettrez, D. H. Edgell, R. Epstein, K. A. Fletcher, J. A. Frenje, V. Yu. Glebov, D. R. Harding, S. X. Hu, I. V. Igumenshchev, J. P. Knauer, S. J. Loucks, C. K. Li, J. A. Marozas, F. J. Marshall, R. L. McCrory, P. W. McKenty, D. D. Meyerhofer, P. M. Nilson, S. P. Padalino, R. D. Petrasso, P. B. Radha, S. P. Regan, F. H. Seguin, W. Seka, R. W. Short, D. Shvarts, S. Skupsky, V. A. Smalyuk, J. M. Soures, C. Stoeckl, W. Theobald, and B. Yaakobi, *Phys. Plasmas* **17**, 056312 (2010).
4. D. K. Bradley *et al.*, *Rev. Sci. Instrum.* **66**, 716 (1995).
5. T. R. Boehly, D. L. Brown, R. S. Craxton, R. L. Keck, J. P. Knauer, J. H. Kelly, T. J. Kessler, S. A. Kumpan, S. J. Loucks, S. A. Letzring, F. J. Marshall, R. L. McCrory, S. F. B. Morse, W. Seka, J. M. Soures, and C. P. Verdon, *Opt. Commun.* **133**, 495 (1997).
6. T. C. Sangster, V. N. Goncharov, R. Betti, P. B. Radha, T. R. Boehly, D. T. Casey, T. J. B. Collins, R. S. Craxton, J. A. Delettrez, D. H. Edgell, R. Epstein, C. J. Forrest, J. A. Frenje, D. H. Froula, M. Gatu-Johnson, V. Yu. Glebov, D. R. Harding, M. Hohenberger, S. X. Hu, I. V. Igumenshchev, R. Janezic, J. H. Kelly, T. J. Kessler, C. Kingsley, T. Z. Kosc, J. P. Knauer, S. J. Loucks, J. A. Marozas, F. J. Marshall, A. V. Maximov, R. L. McCrory, P. W. McKenty, D. D. Meyerhofer, D. T. Michel, J. F. Myatt, R. D. Petrasso, S. P. Regan, W. Seka, W. T. Shmayda, R. W. Short, A. Shvydki, S. Skupsky, J. M. Soures, C. Stoeckl, W. Theobald, V. Versteeg, B. Yaakobi, and J. D. Zuegel, *Phys. Plasmas* **20**, 056317 (2013).
7. C. Stoeckl, J. A. Delettrez, J. H. Kelly, T. J. Kessler, B. E. Kruschwitz, S. J. Loucks, R. L. McCrory, D. D. Meyerhofer, D. N. Maywar, S. F. B. Morse, J. Myatt, A. L. Rigatti, L. J. Waxer, J. D. Zuegel, and R. B. Stephens, *Fusion Sci. Technol.* **49**, 367 (2006).
8. C. Stoeckl, G. Fiksel, D. Guy, C. Mileham, P. M. Nilson, T. C. Sangster, M. J. Shoup III, and W. Theobald, *Rev. Sci. Instrum.* **83**, 033107 (2012).
9. *LLE Review Quarterly Report* **81**, 6, Laboratory for Laser Energetics, University of Rochester, Rochester, NY, LLE Document No. DOE/SF/19460-335 (1999).
10. INRAD Optics, Northvale, NJ 07647.
11. Photon Engineering, accessed 9 April 2012, <http://www.photonengr.com>.
12. Q22, QED Technologies, LLC, Rochester, NY 14607.
13. J. A. Oertel, T. Archuleta, C. G. Peterson, and F. J. Marshall, *Rev. Sci. Instrum.* **68**, 789 (1997).
14. NTI AG - LinMot & MagSpring, CH-8957 Spreitenbach, Switzerland.
15. J. Delettrez, R. Epstein, M. C. Richardson, P. A. Jaanimagi, and B. L. Henke, *Phys. Rev. A* **36**, 3926 (1987).
16. Prism Computational Sciences, Inc., Madison, WI 53711.

Time-Resolved Compression of a Spherical Shell with a Re-Entrant Cone to High Areal Density for Fast-Ignition Laser Fusion

The compression of matter to a very high density is of general interest for high-energy-density physics,¹ laboratory astrophysics,² and inertial confinement fusion (ICF).³ This article reports on picosecond, time-resolved, monochromatic 8-keV x-ray radiographic measurements of imploded cone-in-shell targets on the OMEGA laser. The results show that a spherical shell with a re-entrant cone—a system with broken spherical symmetry—can be successfully compressed with long-pulse (\sim ns) lasers to a final mass density and geometry that provide favorable characteristics for subsequent ignition with a short-pulse (\sim ps) laser. We find excellent agreement with predictions from two-dimensional (2-D) radiation–hydrodynamic simulations with the code *DRACO*.⁴ This work is an important step forward for fast ignition⁵ because it demonstrates that sufficient areal density can be assembled at the tip of the re-entrant cone to trap the fraction of the fast-electron energy spectrum (\sim MeV) from the short-pulse laser that is relevant for fast ignition.

Over the last four decades, a tremendous effort has been devoted to studying the physics of high-density matter by compressing spherical shells with powerful laser beams.^{6,7} Achieving high compression with pressures $\sim 10^{16}$ Pa is vital for ICF, where a few milligrams of frozen deuterium and tritium fuel are compressed by laser light ablation (direct drive) or by x-ray ablation (indirect drive) to such high temperatures and densities that ignition is reached and a thermonuclear burn wave spreads through the shell. Similar pressures found inside astrophysical objects make laboratory compression experiments interesting for studying those material states. Pressures of $\sim 10^{16}$ Pa prevail in the sun’s core, while they are $\sim 100\times$ lower in the core of giant planets. An important step toward ignition has been recently demonstrated by measuring fusion energy that exceeds the energy coupled in the fuel in an ICF implosion.⁸ So far, ignition has not been reached despite code predictions. Besides the conventional “hot-spot” approach, which triggers ignition in the center of a rapidly converging shell, alternative approaches such as fast ignition (FI)⁵ and shock ignition (SI),⁹ which separate the compression and ignition phases of the implosion, have been proposed. Ignition is achieved from highly localized heating: on the side of the high-density fuel

using a separate ultrahigh-intensity laser (FI) or in the center of the compressed shell by a converging shock wave (SI). These concepts are attractive because higher gains might be achievable than with central hot-spot ignition. Early experiments studying the FI concept^{10,11} reported a coupling efficiency of 15% to 30% of the short-pulse laser energy into the compressed plasma. Those experiments were limited by several factors, including insufficient drive-laser energy (2.5 kJ), no pulse-shaping capability, and a longer drive-laser wavelength (532 nm instead of 351 nm)—unfavorable factors for achieving high compression. In addition, the low number of overlapping drive beams resulted in a large illumination nonuniformity that affected the symmetry and possibly the hydrodynamic stability of the implosion. Laser pulse shaping is necessary to compress the target on a low adiabat (α), which is defined as the ratio of the plasma pressure in the shell to the Fermi pressure of a degenerate electron gas.¹² A low adiabat is a prerequisite for high target compression. Based on our experiments and simulations, we conclude that the FI experiments^{10,11} were merely qualitative and were not guided by sufficient simulation capability to adequately describe this complicated radiation–hydrodynamic problem. It is therefore questionable whether sufficient compression was achieved to stop MeV electrons and surprising that such high coupling efficiencies were reported^{10,11} (efficiencies that could not be reproduced in experiments on OMEGA¹³). Follow-up experiments at the Institute for Laser Engineering confirm an insufficient compression, being $\sim 10\times$ lower than was previously estimated, and a much lower ($\sim 1.6\%$) short-pulse beam-energy coupling.¹⁴

In the experiments reported here, thin plastic shells with an embedded hollow cone made out of high-Z material were imploded. The purpose of the cone was to provide a plasma-free path for the short-pulse ignition laser to propagate as close as possible to the dense fuel. One complication is that the cone breaks the spherical symmetry and requires multidimensional simulation capability to accurately model both the flow of the material and the interaction between radiation and matter. The picosecond, time-resolved radiographic measurements of the hydrodynamic evolution of cone-in-shell implosions presented

here demonstrate for the first time the assembly of plasma dense enough to stop MeV electrons at a time when the cone tip has not been breached by the implosion, which is an important requirement for fast ignition. This is possible only because of the unique experimental capability of the Omega Laser Facility and a significant improvement in multidimensional simulations. The excellent agreement between experiment and simulation obtained here provides a benchmark for the code calculations that will be used to further improve implosion performance.

Important quantities that characterize the fuel assembly are the mass-density distribution $\rho(r)$ and the areal density ρR , which is given by the integral of ρ over the spatial coordinate from the shell's center to infinity, $\int_0^\infty \rho dr$. Measurements of ρR and ρ provide a method to compare the actual and predicted implosion performances. Radiography with x rays in combination with a framing camera is a technique¹⁵ to spatially measure and temporally resolve the fuel mass; it has been used on OMEGA to study the implosion dynamics of deuterium gas-filled plastic spherical shells without a cone using an ~ 5 -keV broadband backlighter driven by an ~ 1 -ns laser, and a camera with an ~ 40 -ps integration time.¹⁶ A mass-density distribution $\rho(r)$ and a ρR of up to ~ 60 mg/cm² were measured at various

times outside of peak compression.¹⁶ In those experiments a strong x-ray self-emission from the hot core prevented a measurement at peak compression. Previous experiments with cone-in-shell targets in indirect¹⁷ and direct drive^{18,19} investigated high-adiabat implosions with simple square pulses, which lacked quantitative comparison to simulations.

The current experiment used thick ($42\text{-}\mu\text{m}$) plastic shells with a cone and a low gas pressure (~ 0.8 atm of air) imploded by a shaped laser pulse to minimize x-ray self-emission. An x-ray source driven by a short pulse with a shorter emission time and a higher photon energy combined with a narrow-bandwidth ($\Delta E/E = 1.2 \times 10^{-3}$) crystal imager provided the necessary tool to study the fuel assembly in unprecedented detail. The mass-absorption coefficient μ of the compressed material is a function of the photon energy, and measuring it with a spectrally pure photon source significantly decreases the uncertainty in the inference of mass density and areal density. Figure 139.34(a) shows the experimental setup. The cone-in-shell target [Fig. 139.34(b)] consisted of a hollow gold cone mounted inside a plastic shell. A small aluminum cylindrical tip was mounted on the end of the cone. The purpose of the $60\text{-}\mu\text{m}$ -thick Al tip was to delay the shock breakout

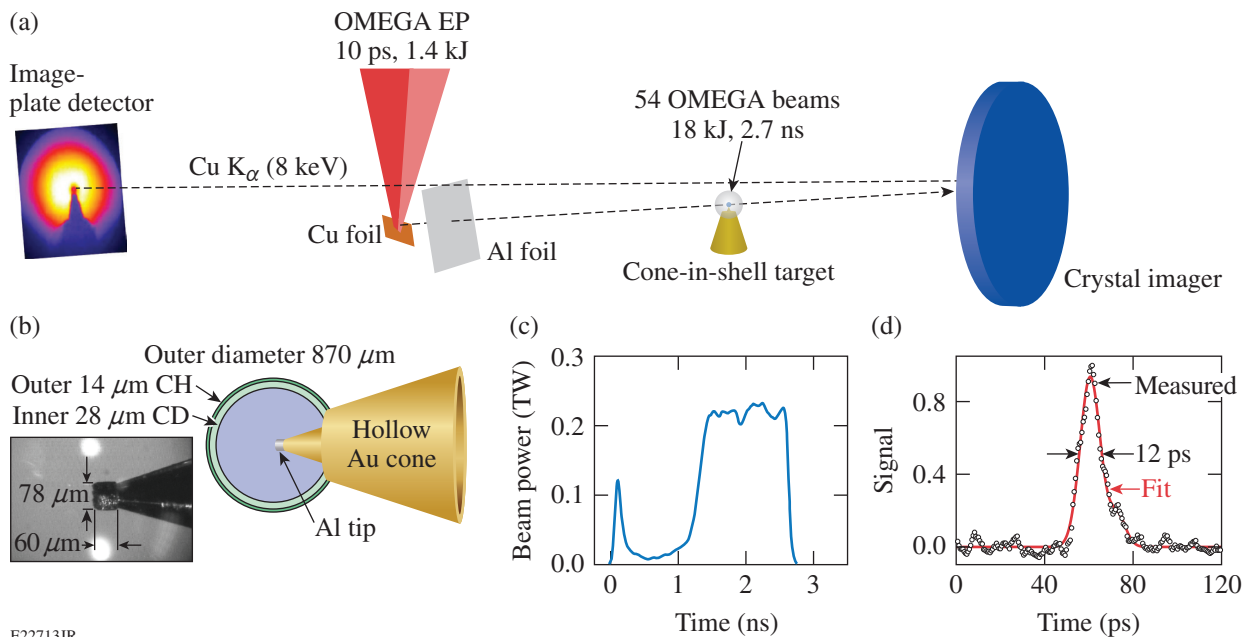


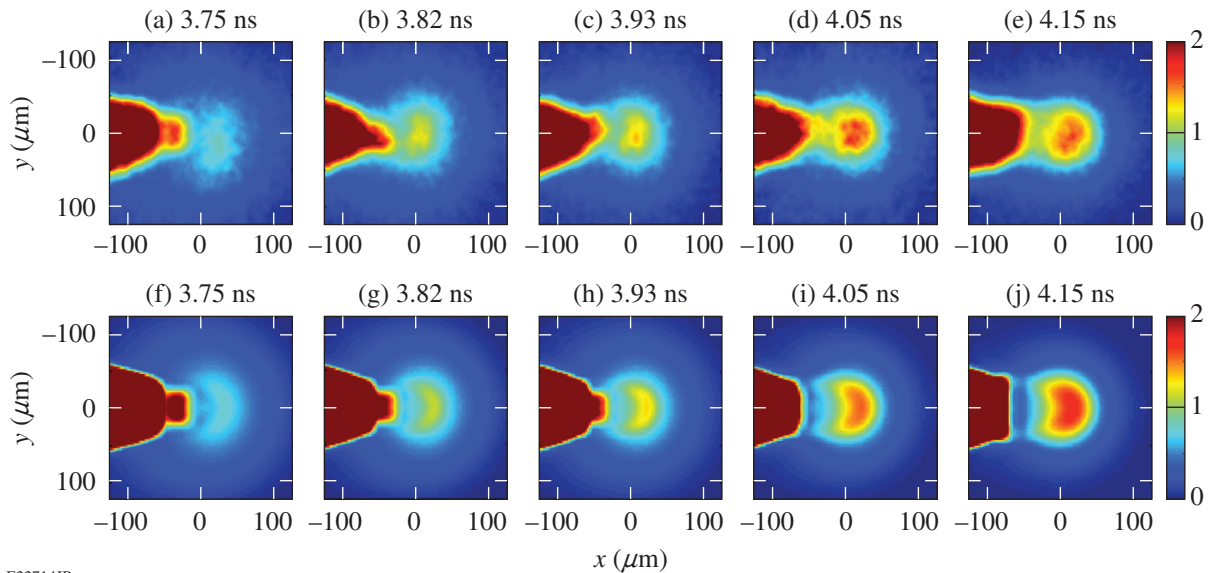
Figure 139.34

(a) Schematic of the setup of the backlighter experiment with a Cu foil irradiated by the OMEGA EP short-pulse beam and using 54 OMEGA beams to implode a cone-in-shell target. A $50\text{-}\mu\text{m}$ -thick Al foil was located 2 mm from the Cu foil to shield it from plasma and x-ray radiation from the implosion. A raw image of the fuel assembly is shown in the image plane. The distances are not to scale. (b) Illustration of the cone-in-shell target. (c) Laser pulse shape to implode the capsule. (d) Time-resolved K_α x-ray emission from a Cu foil target irradiated with an ~ 1 -kJ, 10-ps pulse.

compared to a previous design with a 15- μm Au tip.¹³ There is a trade-off between having sufficient tip material to delay the breakout and a good electron coupling into the core because more material affects the electron transport and increases the standoff distance from source to core. After imploding the shell with 54 OMEGA UV beams⁶ with an energy of ~ 18 kJ and the drive pulse shown in Fig. 139.34(c), a thin Cu foil was irradiated by the ~ 1.4 -kJ, 10-ps OMEGA EP short-pulse laser.²⁰ The OMEGA EP laser was defocused to an ~ 200 - μm spot that provided an intensity of $\sim 5 \times 10^{17}$ W/cm² and generated fast electrons with a kinetic energy in the range of several 100 keV to \sim MeV (Ref. 21). Strong electrostatic sheath fields at the target boundary retain most of the fast electrons in the ~ 1 -mm foil. The electrons recirculate and generate K_{α} radiation, providing a relatively uniform Cu K_{α} area backlighter source. A spherical Bragg crystal imager²² tuned to the Cu $K_{\alpha 1}$ line (8.048 keV) was located on the opposite side of the target and imaged the implosion onto an image-plate detector with a magnification of 14.7. The imaging system efficiently rejects unwanted background and x-ray self-emission from the implosion. The technique also benefits from a higher probing photon energy because the plasma self-emission scales with $\exp(-h\nu/kT)$, where $h\nu$ is the photon energy and kT is the plasma temperature. In shots without a backlighter, the background at 8 keV

caused by self-emission from the implosion was measured to be $\sim 40\times$ weaker than the signal of the K_{α} backlighter. Another important parameter for this technique is the emission time of the backlighter, which determines the time resolution because a time-integrating detector was used. Figure 139.34(d) shows a time-resolved measurement of the K_{α} flash²¹ by coupling an ultrafast x-ray streak camera to the Bragg crystal imager. A K_{α} emission time of 12 ps was quantified, which is short enough to prevent any spatial blurring from the hydrodynamic motion.

First, an image of an undriven target was taken, where the Al tip is clearly visible and less opaque than the gold cone. The image was corrected for spatially varying backlighter intensity, similar to that described in Ref. 16, and for hard x rays that were generated in the foil and scattered in the diagnostic. This shot provided an independent measurement of the magnification of 14.8 ± 0.1 and a measure of the spatial resolution of 22 ± 3 μm . The backlighter was then used to image imploded targets. The time delay between the implosion laser and short-pulse laser was varied on a shot-to-shot basis to probe the fuel assembly at various times [see Figs. 139.35(a)–139.35(e)]. The false color scheme represents the measured optical depth given by $\ln(I_0/I)$, where I is the measured transmitted signal and I_0 is the measured backlighter intensity. The frame in



E22714JR

Figure 139.35

Flash radiography images of imploded cone-in-shell targets at various stages of the implosion. The probing time was measured *in situ* with ± 0.05 -ns accuracy at full energy by operating the neutron temporal diagnostic²³ in hard x-ray mode. The top row shows the experimental data at (a) 3.75 ns, (b) 3.82 ns, (c) 3.93 ns, (d) 4.05 ns, and (e) 4.15 ns after the start of the UV drive-laser pulse. The bottom row [(f)–(j)] shows simulated radiographs from 2-D radiation–hydrodynamic simulations. The false color scheme indicates the optical depth.

Fig. 139.35(a) shows the implosion at 3.75 ns after the start of the drive pulse. Time zero is defined as the time when 2% of the peak power from the drive-laser pulse is reached. The fuel starts to assemble in front of the tip and the Al tip was compressed to a higher density, which can be seen when comparing the measured optical depth in the Al tip to that of the undriven target. At later times the Al tip was more deformed and eventually completely destroyed as the fuel assembly reached a higher density. Peak compression was reached at the time of the frame in Fig. 139.35(d) at $T_{\text{peak}} = 4.05$ ns, while the last frame was recorded after peak compression at 4.15 ns. Figures 139.35(f)–139.35(j) display calculated backlighter images for those shots. The simulations were performed with the 2-D radiation–hydrodynamic code *DRACO*⁴ in cylindrical geometry and were post-processed with the code *Spect3D*.²⁴ The simulation capability was significantly improved compared to the results reported in Ref. 13. The radiation transport has been included, the Eulerian scheme improved, and nonlocal thermal electron transport²⁵ and cross-beam energy transfer²⁶ accounted for. The simulations compare well with the measured images, revealing similar structure and size of the imploded plastic material. The simulated optical densities agree to better than 10% with the measured optical densities. Slight differences are observed in the shape of the high-density region, which might be caused by three-dimensional (3-D) effects that were not taken into account in the simulations. For late times, some differences are observed in the region between the destroyed Al tip and the dense plasma core. While the simulations show a distinctive gap, the gap is less pronounced in the measurements, which could be a result of turbulent plasma behavior and some mixing of ablated Al material with the plastic. No significant mixing of aluminum and plastic material is noticed in the 2-D simulations but could be stronger in reality. Slight shot-to-shot differences in the deformation of the Al tip do not affect the overall performance of the implosion.

The measured optical-depth distribution was used to infer time-resolved radial density distributions and time-resolved areal densities under the assumption of cylindrical symmetry of the plasma along the cone axis. The optical depth τ is given by the integral over the absorption coefficient κ along the path of an x-ray photon through the dense plasma $\tau = \int \kappa(x) dx$, measured at the specific backlighter photon energy. Vertical line-out profiles $\tau(y)$ (see Fig. 139.36) taken through the dense core show maximum values of up to 1.65 ± 0.1 and a full width at half maximum (FWHM) as small as $\sim 80 \mu\text{m}$. Those profiles were Abel inverted to infer κ . The absorption coefficient is equal to the product of the mass-absorption coefficient μ and the mass density ρ , where μ is a function of plasma electron temperature

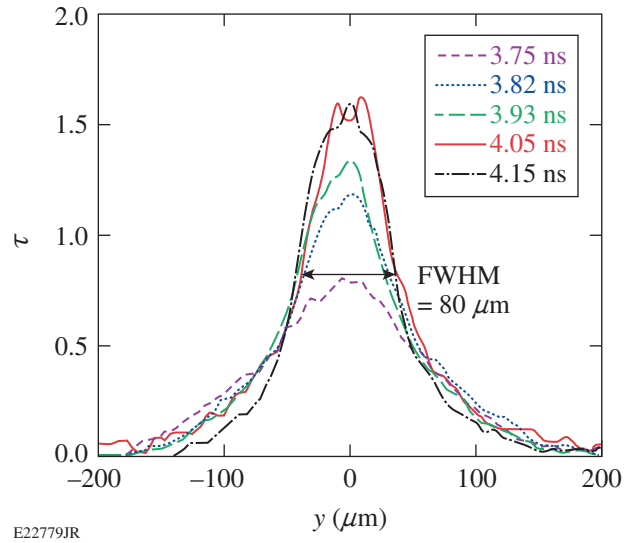


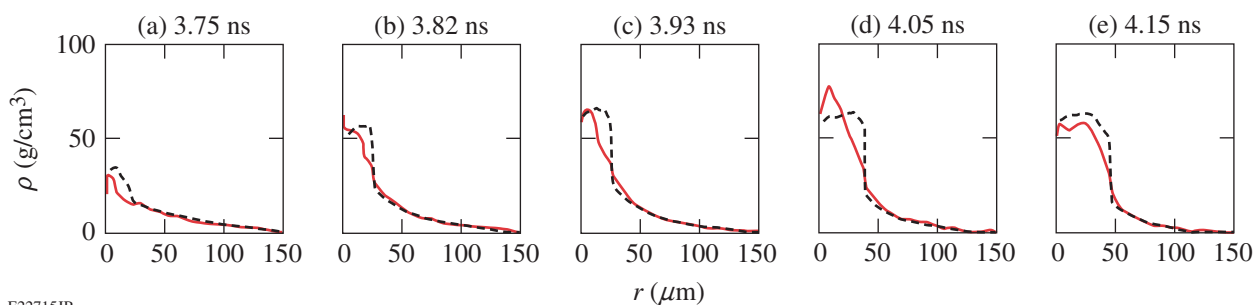
Figure 139.36

Time-resolved optical-depth lineouts through the dense core of compressed plastic measured at a photon energy of 8.048 keV.

T_e and ρ . A steady-state nonlocal thermal electron calculation of μ was performed and the density profile was inferred by dividing κ by μ . Inferred and simulated $\rho(r)$ are compared in Figs. 139.37(a)–139.37(e) at various times. They are very similar for radii larger than $50 \mu\text{m}$ but show slight differences in the dense region. The inferred $\rho(r)$ is integrated to obtain ρR , which is compared to the predicted value [Fig. 139.38(a)]. The measured areal densities agree with the simulations to better than 15%. A simple expression for maximum ρR was derived in Ref. 27 for an imploded DT capsule filled with 1 atm of DT gas, which makes it possible for the maximum ρR to be scaled with the drive laser energy E_L , the laser wavelength λ , and the adiabat α_{inn} of the inner portion of the shell:

$$(\rho R)_{\text{max}} \left(\text{mg/cm}^2 \right) \approx 260 E_L^{1/3} \text{ (kJ)} \frac{\left[0.35 / \lambda (\mu\text{m}) \right]^{0.25}}{\alpha_{\text{inn}}^{0.54}}.$$

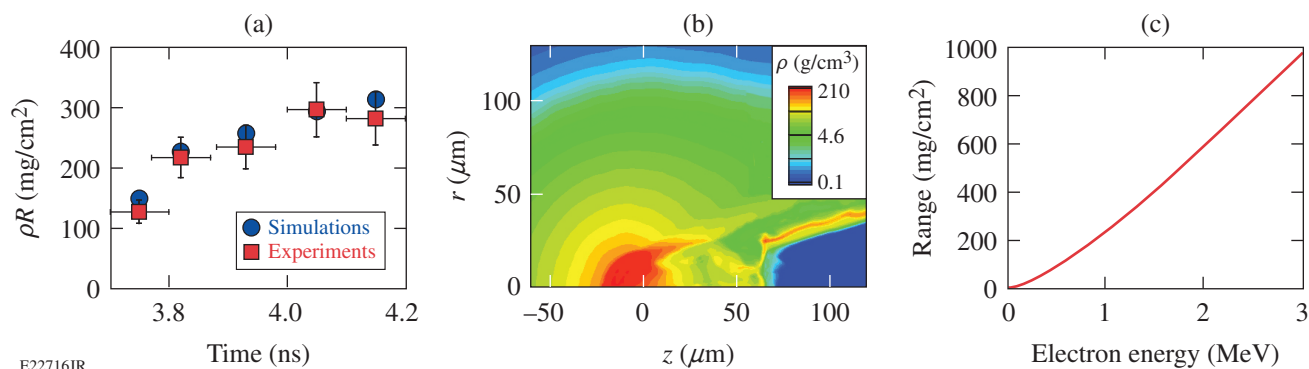
For the current experiment, $E_L = 18$ kJ and $\alpha_{\text{inn}} = 3.5$, for which the simple expression yields ~ 350 mg/cm², only $\sim 17\%$ higher than the actual value, showing that the scaling model can be used to estimate the expected $(\rho R)_{\text{max}}$ for different energies and adiabats. For a laser energy of 1.9 MJ, which was used in a recent experiment⁸ at the National Ignition Facility, and for $\alpha_{\text{inn}} = 3.5$, a value of $(\rho R)_{\text{max}} \sim 1600$ mg/cm² is estimated, which is a factor of ~ 4.6 higher than with OMEGA. A higher areal density allows for particle stopping up to a higher kinetic energy and, given a certain distribution of kinetic energies, relaxes the requirement to ignite the fuel.



E22715JR

Figure 139.37

Measured (solid) and simulated (dashed) density profiles perpendicular to the cone axis for various times.



E22716JR

Figure 139.38

(a) Measured (squares) and simulated (circles) areal density perpendicular to the cone axis for various times. (b) Simulated mass-density distribution of the improved implosion at the time of shock breakout at 3.96 ns, which provides an areal density of 500 mg/cm². (c) Calculated range of fast electrons in compressed deuterated plastic.

In addition, the breakout time of the shock driven through the cone tip was measured independently, similar to experiments that were described in detail in Refs. 13 and 19. The shots were performed by firing only the OMEGA beams and switching off the OMEGA EP beam. The compressing shell pushed a jet of plasma material toward the cone tip and created a shock wave through the cone wall. When the shock wave reached the inner cone surface, it generated optical emission, which was measured temporally and spatially resolved from the inside with a streaked optical pyrometer²⁸ and two velocity interferometer systems for any reflector.²⁹ The measured average breakout time from three implosions was $T_{\text{shock}} = 3.85 \pm 0.04$ ns, which agrees well with the predicted value of 3.84 ns. The target is more resilient against the strong shock from the implosion than a previous design with a gold-only cone.¹³ Those experiments measured the breakout time for various gold-cone tips with thicknesses from 5 to 15 μm and demonstrated a later breakout for thicker tips. For a 15- μm thickness, the breakout time was 3.76 ns. Therefore, the target

with the 60- μm -thick Al tip improved the margin for the arrival of the short-pulse laser by ~ 90 ps, bringing the ρR at 3.85 ns to ~ 200 mg/cm² [Fig. 139.38(a)], which is $\sim 70\%$ of the peak ρR .

Our simulations indicate that an even higher ρR might be achievable on OMEGA by removing the air from the shell and reducing the power of the laser pulse picket. Figure 139.38(b) shows the calculated mass-density map at shock breakout for the improved design. The mass and energy of the hot spot are decreased, which delays the cone-tip breakout by reducing the pressure on the cone tip. Fuel stagnation is closer to the target center with a higher density and higher areal density. It brings the shock breakout as close as 80 ps to the peak compression time. At the time of shock breakout, the areal density reaches 500 mg/cm², 83% of $\rho R_{\text{max}} = 600$ mg/cm². It is important to note that such high areal densities provide sufficiently dense plasma to stop fast electrons. Figure 139.38(c) shows the calculated average range of fast electrons in compressed deuterated plastic including blooming and straggling.³⁰ Electrons up to

1.8 MeV will completely range out in a $\rho R = 500\text{-mg/cm}^2$ plastic plasma, while a 200-mg/cm^2 plasma stops electrons up to 0.9 MeV.

In conclusion, a spherical plastic shell with a re-entrant cone was successfully compressed to a high areal density ($\sim 300\text{ mg/cm}^2$) at a distance of $\sim 50\text{ }\mu\text{m}$ in front of the cone tip, which provides sufficient stopping power for $\sim\text{MeV}$ electrons—a characteristic that is required for subsequent ignition with a short-pulse ($\sim\text{ps}$) laser.

ACKNOWLEDGMENT

This material is based upon work supported by the Department of Energy National Nuclear Security Administration under Award Number DE-NA0001944, the OFES Fusion Science Center grant No. DE-FC02-04ER54789, the OFES ACE Fast Ignition grant No. DE-FG02-05ER54839, the DOE Laboratory Basic Science Program, the University of Rochester, and the New York State Energy Research and Development Authority. The support of DOE does not constitute an endorsement by DOE of the views expressed in this article. J. J. S. participated in this work thanks to funding from the French National Agency for Research (ANR) and the competitiveness cluster Alpha-Route des Lasers through project TERRE ANR-2011-BS04-014.

REFERENCES

1. R. P. Drake, *High-Energy-Density Physics: Fundamentals, Inertial Fusion, and Experimental Astrophysics*, Shock Wave and High Pressure Phenomena (Springer, Berlin, 2006).
2. B. A. Remington, R. P. Drake, and D. D. Ryutov, *Rev. Mod. Phys.* **78**, 755 (2006).
3. J. Nuckolls *et al.*, *Nature* **239**, 139 (1972).
4. P. B. Radha, T. J. B. Collins, J. A. Delettrez, Y. Elbaz, R. Epstein, V. Yu. Glebov, V. N. Goncharov, R. L. Keck, J. P. Knauer, J. A. Marozas, F. J. Marshall, R. L. McCrory, P. W. McKenty, D. D. Meyerhofer, S. P. Regan, T. C. Sangster, W. Seka, D. Shvarts, S. Skupsky, Y. Srebro, and C. Stoeckl, *Phys. Plasmas* **12**, 056307 (2005).
5. M. Tabak *et al.*, *Phys. Plasmas* **1**, 1626 (1994).
6. T. R. Boehly, D. L. Brown, R. S. Craxton, R. L. Keck, J. P. Knauer, J. H. Kelly, T. J. Kessler, S. A. Kumpan, S. J. Loucks, S. A. Letzring, F. J. Marshall, R. L. McCrory, S. F. B. Morse, W. Seka, J. M. Soures, and C. P. Verdon, *Opt. Commun.* **133**, 495 (1997).
7. E. I. Moses *et al.*, *Phys. Plasmas* **16**, 041006 (2009).
8. O. A. Hurricane *et al.*, *Nature* **506**, 343 (2014).
9. R. Betti, C. D. Zhou, K. S. Anderson, L. J. Perkins, W. Theobald, and A. A. Solodov, *Phys. Rev. Lett.* **98**, 155001 (2007).
10. R. Kodama *et al.*, *Nature* **412**, 798 (2001).
11. R. Kodama *et al.*, *Nature* **418**, 933 (2002).
12. S. Atzeni and J. Meyer-ter-Vehn, *The Physics of Inertial Fusion: Beam Plasma Interaction, Hydrodynamics, Hot Dense Matter*, International Series of Monographs on Physics (Clarendon Press, Oxford, 2004).
13. W. Theobald, A. A. Solodov, C. Stoeckl, K. S. Anderson, R. Betti, T. R. Boehly, R. S. Craxton, J. A. Delettrez, C. Dorrer, J. A. Frenje, V. Yu. Glebov, H. Habara, K. A. Tanaka, J. P. Knauer, R. Lauck, F. J. Marshall, K. L. Marshall, D. D. Meyerhofer, P. M. Nilson, P. K. Patel, H. Chen, T. C. Sangster, W. Seka, N. Sinenian, T. Ma, F. N. Beg, E. Giraldez, and R. B. Stephens, *Phys. Plasmas* **18**, 056305 (2011).
14. Y. Arikawa *et al.*, *Bull. Am. Phys. Soc.* **58**, 372 (2013).
15. O. L. Landen *et al.*, *Rev. Sci. Instrum.* **72**, 627 (2001).
16. F. J. Marshall, P. W. McKenty, J. A. Delettrez, R. Epstein, J. P. Knauer, V. A. Smalyuk, J. A. Frenje, C. K. Li, R. D. Petrasso, F. H. Séguin, and R. C. Mancini, *Phys. Rev. Lett.* **102**, 185004 (2009).
17. R. B. Stephens *et al.*, *Phys. Rev. Lett.* **91**, 185001 (2003).
18. R. B. Stephens, S. P. Hatchett, M. Tabak, C. Stoeckl, H. Shiraga, S. Fujioka, M. Bonino, A. Nikroo, R. Petrasso, T. C. Sangster, J. Smith, and K. A. Tanaka, *Phys. Plasmas* **12**, 056312 (2005).
19. C. Stoeckl, T. R. Boehly, J. A. Delettrez, S. P. Hatchett, J. A. Frenje, V. Yu. Glebov, C. K. Li, J. E. Miller, R. D. Petrasso, F. H. Séguin, V. A. Smalyuk, R. B. Stephens, W. Theobald, B. Yaakobi, and T. C. Sangster, *Plasma Phys. Control. Fusion* **47**, B859 (2005).
20. L. J. Waxer, D. N. Maywar, J. H. Kelly, T. J. Kessler, B. E. Kruschwitz, S. J. Loucks, R. L. McCrory, D. D. Meyerhofer, S. F. B. Morse, C. Stoeckl, and J. D. Zuegel, *Opt. Photonics News* **16**, 30 (2005).
21. P. M. Nilson, J. R. Davies, W. Theobald, P. A. Jaanimagi, C. Mileham, R. K. Jungquist, C. Stoeckl, I. A. Begishev, A. A. Solodov, J. F. Myatt, J. D. Zuegel, T. C. Sangster, R. Betti, and D. D. Meyerhofer, *Phys. Rev. Lett.* **108**, 085002 (2012).
22. C. Stoeckl, G. Fiksel, D. Guy, C. Mileham, P. M. Nilson, T. C. Sangster, M. J. Shoup III, and W. Theobald, *Rev. Sci. Instrum.* **83**, 033107 (2012).
23. R. A. Lerche, D. W. Phillion, and G. L. Tietbohl, *Rev. Sci. Instrum.* **66**, 933 (1995).
24. J. J. MacFarlane *et al.*, *High Energy Density Phys.* **3**, 181 (2007).
25. V. N. Goncharov, T. C. Sangster, P. B. Radha, R. Betti, T. R. Boehly, T. J. B. Collins, R. S. Craxton, J. A. Delettrez, R. Epstein, V. Yu.

- Glebov, S. X. Hu, I. V. Igumenshchev, J. P. Knauer, S. J. Loucks, J. A. Marozas, F. J. Marshall, R. L. McCrory, P. W. McKenty, D. D. Meyerhofer, S. P. Regan, W. Seka, S. Skupsky, V. A. Smalyuk, J. M. Sours, C. Stoeckl, D. Shvarts, J. A. Frenje, R. D. Petrasso, C. K. Li, F. Séguin, W. Manheimer, and D. G. Colombant, *Phys. Plasmas* **15**, 056310 (2008).
26. D. H. Froula, I. V. Igumenshchev, D. T. Michel, D. H. Edgell, R. Follett, V. Yu. Glebov, V. N. Goncharov, J. Kwiatkowski, F. J. Marshall, P. B. Radha, W. Seka, C. Sorce, S. Stagnitto, C. Stoeckl, and T. C. Sangster, *Phys. Rev. Lett.* **108**, 125003 (2012).
27. R. Betti and C. Zhou, *Phys. Plasmas* **12**, 110702 (2005).
28. J. E. Miller, T. R. Boehly, A. Melchior, D. D. Meyerhofer, P. M. Celliers, J. H. Eggert, D. G. Hicks, C. M. Sorce, J. A. Oertel, and P. M. Emmel, *Rev. Sci. Instrum.* **78**, 034903 (2007).
29. P. M. Celliers, D. K. Bradley, G. W. Collins, D. G. Hicks, T. R. Boehly, and W. J. Armstrong, *Rev. Sci. Instrum.* **75**, 4916 (2004).
30. A. A. Solodov and R. Betti, *Phys. Plasmas* **15**, 042707 (2008).

Precompensation of Gain Nonuniformity in a Nd:Glass Amplifier Using a Programmable Beam-Shaping System

Introduction

A dynamic beam-shaping system using a liquid crystal spatial light modulator (SLM) has undergone a successful transition from initial proof-of-principle demonstrations^{1,2} to implementation in a high-energy laser such as LLE's OMEGA EP.³ The operation principle of the beam-shaping system is based on the phase-only carrier method, which enables one to have arbitrary two-dimensional (2-D) control of both the laser-beam fluence and wavefront by adjusting the modulation depth and the bias of the carrier phase. A liquid crystal on silicon (LCOS) SLM can be used to create a programmable high-frequency carrier phase. Closed-loop operation of such a device paired with feedback from a near-field camera or a wavefront sensor dramatically improves the performance.²

Gain precompensation⁴ and spot shadowing,^{5,6} are important applications of a dynamic beam shaper in high-energy lasers. The precompensation of gain inhomogeneity in amplifiers reduces the peak-to-mode in fluence distribution in such a way that the total energy of the beam can be increased without risking damage to the optics. The gain precompensation in OMEGA EP long-pulse (ns) beamlines is achieved in multiple steps using both static and dynamic beam shapers.^{3,7} The dynamic beam shaper is located in the low-energy front end, where a residual 2-D correction map is applied to improve the overall system gain precompensation performance and the uniformity of the final output beam. A similar gain precompensation experiment was performed in another facility for a Nd:glass amplifier but with insignificant improvement in beam uniformity.⁸

This article presents a more-challenging application of dynamic beam shaping in the context of a 50-J, 700-fs optical parametric chirped-pulse-amplification (OPCPA) system. The high degree of gain saturation in the optical parametric amplification (OPA) crystals precludes the possibility of installing the SLM before the OPA. The incident beam energy on an SLM installed after the OPA is high enough, however, to damage the device if not carefully managed. Pulse contrast degradation caused by the secondary reflection from the front

surface of the SLM cover glass is a non-negligible problem in this pulse-width regime. It introduces a prepulse 30 ps before the main pulse. We have been able to mitigate or remove these problems. The details of our approach will be described later.

Significant improvements and diversifications in the algorithms and the mode of operations of the carrier method have been made. First, a large discrepancy was found between the analytic transmission function derived in Ref. 1 and the experimental function. An empirical formula is introduced here that agrees better with the measurements. It greatly improves the accuracy of the open-loop algorithm. The closed-loop algorithm introduced in Ref. 2 is based on incrementing or decrementing a fixed unit-step size of the digital command map. It can be inefficient to use a fixed step size where many steps are required for convergence. A more-efficient closed-loop algorithm will be discussed.

The type of carrier used in the carrier beam-shaping method is not limited to a one-dimensional (1-D) rectangular carrier. A checkerboard-pattern carrier was successfully used in the laser-cavity mode shaping in Ref. 9. The choice of the transmitted diffraction order does not need to be the zeroth order. A sawtooth-shaped carrier beam can maximize the diffracted energy into the first-order diffraction term, where the first-order term is chosen to be the main transmitted beam. Such mode of operation is fail-safe since the beam can propagate only in the presence of a carrier.

Improvements to the carrier beam-shaping algorithms will be discussed followed by detailed descriptions of the laser system and the experimental results.

Improvement and Diversification of the Original Carrier Beam-Shaping Method

In the original phase-only carrier beam-shaping method, a rectangular carrier phase is applied to an SLM. A beam incident on the SLM acquires high-frequency modulation in phase and diffracts into the zeroth- and first-order diffractions. As the modulation peak-to-valley (p-v) approaches π , more

energy diffracts into the first- and higher-order diffractions. The diffracted beams are filtered and only the zeroth-order beam is allowed to pass. In this way the intensity transmission factor can be adjusted by controlling the modulation depth of the carrier phase. A 2-D transmission map as a function of carrier amplitude can be generated to achieve a desired beam shape. This principle can be modified in such a way that the first-order diffraction beam passes, whereas the zeroth-order beam is blocked. The benefit of such a configuration is that the beam does not propagate when the SLM fails to introduce the carrier, which is a useful feature for fail-safe operation in a high-energy laser. The disadvantage is that the maximum transmission cannot exceed 50% because the first-order diffractions are equally split. The low efficiency can be improved by using a sawtooth carrier phase (blazed grating) instead of a rectangular one. The diffraction efficiency of the first-order diffraction for the sawtooth carrier phase can be very high. These two modes of operation are schematically shown in Fig. 139.39, where Fig. 139.39(a) describes the original carrier beam-shaping setup and Fig. 139.39(b) shows the modified carrier method in Littrow configuration. We refer to the first configuration as normal mode and the second as diffractive mode. For later discussions, the transmission $[T(x,y)]$ of a carrier method in the near field of each setup after filtering is defined as

$$T(x,y) = \frac{E_{0\text{th order}}(x,y)}{E_{\text{inc}}(x,y)} \quad (1)$$

and

$$T(x,y) = \frac{E_{1\text{st order}}(x,y)}{E_{\text{inc}}(x,y)} \quad (2)$$

for normal- and diffractive-mode methods, respectively. E_{inc} is the incident local energy on the SLM and $E_{0\text{th order}}$, $E_{1\text{st order}}$ are the local reflected energy contained in the zeroth- or first-order diffraction beam, respectively.

1. Improvement in the Open-Loop Algorithm

The algorithm described here assumes using an LCOS-SLM device whose voltage-to-phase-retardation response is linearized by using a look-up table (LUT). Use of an LUT does not completely remove the small variations in phase retardation in individual pixels of an SLM. In our case, the variation is $\pm 6\%$. In an open-loop algorithm, we attempted to achieve the best beam-shaping performance in a single step, neglecting these small variations. We used a reflective LCOS-SLM from Hamamatsu (X10468). The phase of an individual pixel is controlled by applying voltage on the nematic liquid crystal sandwiched between two parallel-aligned alignment layers. The SLM has 600×800 $20\text{-}\mu\text{m}$ pixels over a $12 \times 16\text{-mm}^2$ area. A phase retardation from 0 to 2 waves can be independently introduced on each pixel.

a. Normal mode. The theoretical normal-mode transmission for a rectangular carrier phase with $\pm 2\pi A$ fluctuation was shown to be $|\cos(2\pi A)|^2$ in Ref. 1. The actual transmission deviates, however, from the theoretical prediction. The theoretical and measured transmission curves are shown in Fig. 139.40. The transmission loss from the SLM's reflectivity (93%) was not included in the calculation or measurements. The plot of blue circles is the theoretical prediction, whereas the colored solid lines are the transmissions measured at three different carrier frequencies by varying the carrier amplitude (A) from 0 to 1 wave. The transmission at each carrier frequency was averaged over nine different points on the SLM. The black, blue, and red solid lines correspond to the carrier periodicity

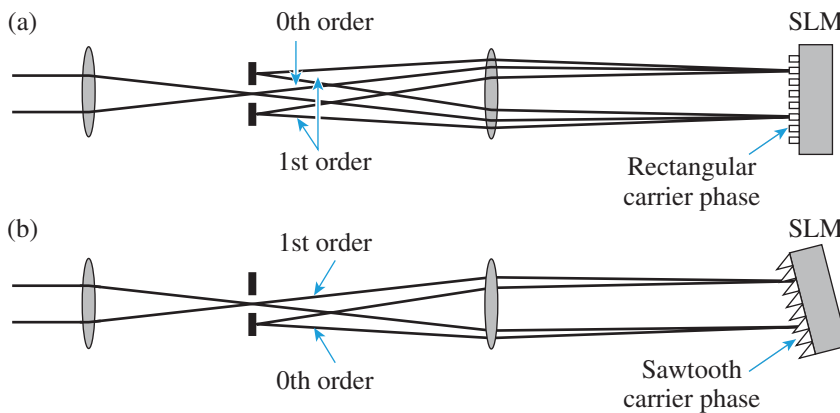


Figure 139.39 Two modes of carrier-beam shaping: (a) normal mode using the zeroth-order beam as the main beam and (b) diffractive mode using the first-order beam as the main beam.

G10187JR

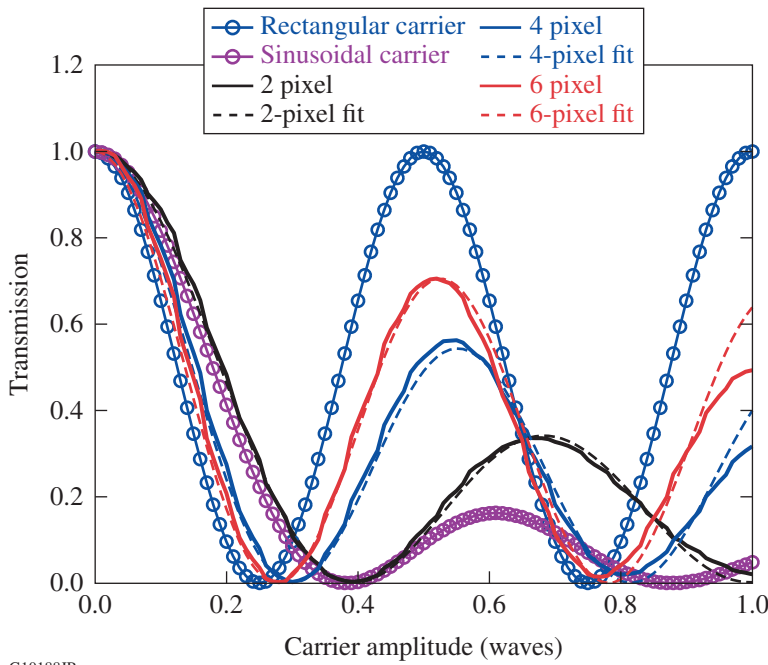


Figure 139.40
Transmission curve with respect to varying wavefront amplitude. The 6-pixel-period carrier transmission is closer to that of the rectangular carrier and the 2-pixel-carrier transmission is closer to the sinusoidal carrier transmission. There is a finite extinction resulting from scattering.

G10188JR

of two, four, and six pixels, respectively. The measured transmission curves show discrepancies with the theoretical curve in that the location of the first minimum is farther away from the theoretical 0.25 and the second peak is lower than 1. The deviation becomes larger as the carrier frequency increases. Another theoretical transmission curve based on a sinusoidal carrier is shown by the plot of purple circles. The analytic transmission function of a sinusoidal carrier is a Bessel function (J_0). Comparison of the analytic and measured transmission curves shows that the measured transmission has characteristics somewhere between the rectangular and sinusoidal carriers. Based on this observation, the empirical transmission function can be expressed using both cosine and Bessel functions as follows:

$$T(A) = (1 - c)[(1 - a) \cos(2\pi bA) + aJ_0(2\pi bA)]^2 c, \quad (3)$$

where T is the transmission as a function of carrier amplitude A . The fit parameters (a, b, c) for each averaged transmission curve are given in Table 139.II. The numerically fit transmission functions are shown as dashed lines in Fig. 139.40.

The locations of the first minima calculated from the analytic function with the given fit parameters are shown in the A_{\min} column. The minimum transmission is the same as c . The value of c is shown to the fourth digit to emphasize the fact that there is a low level of leak even at “zero” transmission. The extinction is better at a lower carrier frequency.

Table 139.II: Rectangular-carrier transmission parameters. The transmission of the 2-pixel (px)-period carrier is fit over $0 < A < 1$. The fit range for 4-pixel- and 6-pixel-period carriers is $0 < A < 0.6$.

Carrier Period	a	b	c	A_{\min}
2 px	0.64	0.80	0.0015	0.40
4 px	0.39	0.95	0.0006	0.30
6 px	0.23	0.97	0.0001	0.28

The choice of carrier frequency depends on beam-shaping applications. The 6-pixel-period carrier requires a smaller carrier wavefront amplitude than the 2-pixel carrier (0.28 versus 0.40) to achieve maximum contrast, leaving the rest of the dynamic range for wavefront correction. On the other hand, the two-pixel-period carrier allows for more digital levels per unit transmission change, and therefore a finer beam-shaping scale.

b. Diffractive mode. The transmission characteristic of the diffractive-mode beam shaping using a sawtooth carrier is shown in Fig. 139.41. The transmission with respect to the blazed-grating amplitude was measured at different grating periods. Each curve was averaged over nine different points on the SLM. The analytic transmission function for a sawtooth carrier is

$$T(A) = \Gamma \left\{ \frac{\sin [2\pi (A - 0.5)]}{2\pi (A - 0.5)} \right\}^2, \quad (4)$$

where Γ is the diffraction efficiency and A is half the p-v of the sawtooth carrier. Γ is lower than 1 because the sawtooth shape is pixelated in LCOS-SLM. As in the case of the rectangular carrier, the analytic transmission function does not agree well with the measured transmission, albeit the discrepancy is smaller in this case. We find that the following empirical expression, made of trigonometric and Bessel functions similar to Eq. (3), fits the data better than the analytic function:

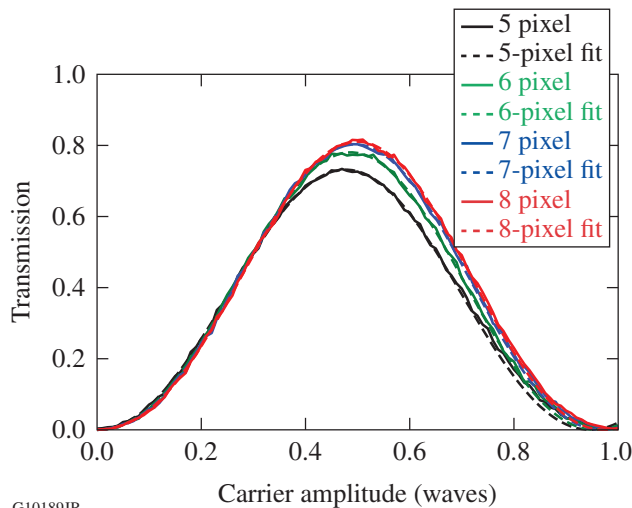
$$T(A) = c \left[(1 - a) \sin (2\pi bA) + aJ_2 (2\pi bA) \right]^2. \quad (5)$$

The fit parameters (a, b, c) are summarized in Table 139.III.

Table 139.III: Sawtooth-carrier transmission parameters. The curves were fit over $0 < A < 0.7$.

Carrier Period	a	b	c	A_{\max}	T_{\max}
5 px	0.52	0.61	1.88	0.48	0.73
6 px	0.65	0.65	2.60	0.49	0.78
7 px	0.69	0.66	2.89	0.50	0.80
8 px	0.70	0.67	3.00	0.50	0.81

Retaining a high diffraction efficiency is important for a diffractive mode. Figure 139.41 suggests that the maximum transmission reaches 81% with an 8-pixel carrier but does



G10189JR

Figure 139.41
Transmission characteristic of the diffractive-mode carrier.

not improve much beyond that. The carrier frequency cannot be set too low in any case because the first- and zeroth-order diffractions must be angularly separated. The effective spatial resolution is also reduced with a large period carrier. As in the rectangular carrier setup, the 93% reflectivity of the device was not included in the measurement. The actual maximum throughput is 75% for the 8-pixel carrier.

The fit parameters in either normal or diffractive mode must be recharacterized whenever there is a change in the design of the LCOS chip, such as the fill factor.

2. Closed-Loop Algorithm

Based on the quasilinear response of the SLM to command voltage, a general form of a 2-D command map $C(x, y)$ including wavefront shaping [$W(x, y)$, bias of carrier] and transmission control [$A(x, y)$, envelope of carrier, same as A in Eqs. (3) and (5)] can be written as

$$C(x, y) = \gamma \left[W(x, y) + A(x, y) \times (\text{carrier}) \right] \quad (6)$$

or

$$C(x, y) = C_W(x, y) + C_A(x, y) \times (\text{carrier}), \quad (7)$$

where the spatial frequency of $W(x, y)$ should be smaller than that of the carrier, γ is a conversion factor from wavefront unit to command voltage, and C_W and C_A are command maps corresponding to W and A , respectively. Because of the small local variations in the phase retardation at a constant voltage across the device, $C(x, y)$ producing the required $W(x, y)$ and $A(x, y)$ cannot be exactly determined in a single step. A closed-loop algorithm is required to improve the result. A variant of the Newton method and a closed-loop algorithm based on that method will be discussed.

a. Constant maximum-derivative Newton method. The Newton method iteratively finds a solution for the equation $F(x) = 0$ using

$$x_{n+1} = x_n - \frac{F(x_n)}{F'(x_n)}, \quad (8)$$

where x corresponds to the command map state. For given wavefront and transmission objectives (W_{obj} and T_{obj}), the function $F(x)$ corresponds to $W(x) - W_{\text{obj}}$ for wavefront shaping and $T(x) - T_{\text{obj}}$ for intensity shaping. $W(x)$ represents the actual

wavefront produced by the SLM at a given command voltage $x = C_W$, and $T(x)$ represents the actual transmission of intensity at a given command voltage $x = C_A$. With only the approximate form of $W(x)$ or $T(x)$ known, the derivative in the Newton search cannot be calculated exactly. $F'(x)$ can be replaced with the derivative of an analytic expression for the mean response. This approach works quite well most of the time but it is not stable. Toward the end of the iterations, x_n can be caught up in an oscillation around the solution and might even diverge, especially where the response is jagged. Our approach is to fix the derivative to a constant value smaller or larger than the actual derivative, depending on its sign. This ensures the convergence of the iterator for any noisy functions. The original Newton search method is modified to

$$x_{n+1} = x_n - \frac{F(x_n)}{F'_{\max}}, \tag{9}$$

where F'_{\max} is smaller than $\inf[F'(x)]$ for a noisy downhill function or larger than $\sup[F'(x)]$ for a noisy uphill function. We present a graphical illustration of this approach in Fig. 139.42 for a noisy uphill function. The initial solution starting from the right-hand side approaches toward the solution without divergence using a positive constant derivative larger than any part of the actual derivative in the function even in noisy conditions. A starting point located in the left-hand side again approaches the solution without divergence. A similar argument can be given for a noisy downhill function. Figure 139.43

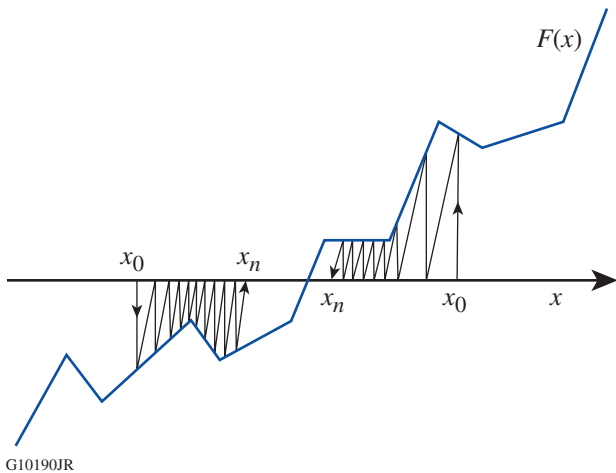


Figure 139.42 Illustration of the constant maximum-derivative Newton search algorithm. A zero of a noisy uphill function is found without diverging by using a constant search derivative larger than $\sup[F'(x)]$, even with local downhill sections.

shows the actual derivatives of the measured normal-mode transmission function of the six-pixel carrier at various points on the SLM, which is very noisy. Since the transmission function for the normal beam-shaping mode is globally downhill, the appropriate constant derivative can be set to -10 lower than any measured derivative.

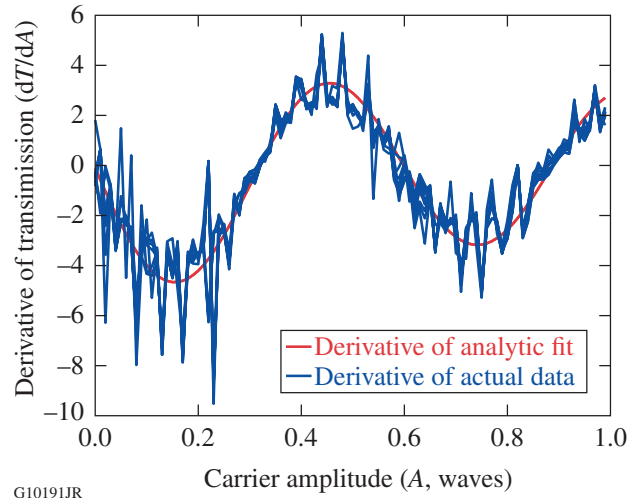


Figure 139.43 The derivative of transmission function. The actual derivative of the measured transmission data of six-pixel period carrier modulation is shown on top of the derivative of the empirical formula.

The proposed method is different from the damped Newton method, which is

$$x_{n+1} = x_n - \alpha \frac{F(x_n)}{F'(x_n)}, \tag{10}$$

where α is a damping factor. This damping factor α allows one to make a conservative move in the next step, but it is not free from the erratic behavior of $F'(x)$. It is also unstable where $F'(x)$ is close to zero, which is one of the general problems of the Newton method. On the other hand, the constant maximum-derivative Newton method always converges. The proposed method is well suited for the case where the general behavior of a function can be expressed as an invertible analytic function but its micro-behavior is not well characterized. The proximity of the solution is reached by inverting the analytic function such as Eq. (3) or Eq. (5). The final solution is refined by Eq. (9).

b. Wavefront- and fluence-shaping algorithms. The iteration algorithms for either wavefront shaping or fluence shaping are formulated using the constant maximum-derivative Newton

method. Since x_n in Eq. (9) represents an independent point in a 2-D command map, F'_{\max} can be independently set for different points on the SLM. Nonetheless, a single number is used for the entire 2-D map for convenience. Since the wavefront response with respect to its command voltage C_W is a monotonically increasing function, one chooses $F'_{\max} > \sup[F'(x)]$. The wavefront response function can be expressed as

$$W(C_W) = W_0(C_W) + \eta(C_W), \quad (11)$$

where $W_0(C_W)$ represents an averaged response of the SLM with respect to the command map. In general this function is a linear function of C_W and $\eta(C_W)$ accounts for the small deviation in the actual response from the ideal linear function. With the objective wavefront denoted as W_{obj} and the constant search derivative as $(dW/dC_W)_{\max}$, the iteration process of the command voltage can be established as follows:

$$C_{W,1} = W_0^{-1}(W_{\text{obj}}), \quad (12)$$

$$C_{W,n+1} = C_{W,n} - \frac{1}{(dW/dC_W)_{\max}} [W(C_{W,n}) - W_{\text{obj}}].$$

The function $W(C_{W,n})$ implies the measurement of the actual wavefront with the n th command map state $C_{W,n}$.

An intensity-shaping closed-loop algorithm can be similarly constructed. The transmission function is again expressed as the sum of an averaged response and small deviation as

$$T(C_A) = T_0(C_A) + \zeta(C_A), \quad (13)$$

where $T_0(C_A)$ denotes either Eq. (3) or Eq. (5) and $\zeta(C_A)$ is a small deviation function. Defining the objective transmission as T_{obj} and the maximum derivative as $(dT/dC_A)_{\max}$, the iteration process for the carrier envelope command voltage is

$$C_{A,1} = T_0^{-1}(T_{\text{obj}}), \quad (14)$$

$$C_{A,n+1} = C_{A,n} - \frac{1}{(dT/dC_A)_{\max}} [T(C_{A,n}) - T_{\text{obj}}].$$

The constant search derivative $(dT/dC_A)_{\max}$ is to be understood as a negative value smaller than the infimum of dT/dC_A in the case of normal-mode beam shaping or a positive value larger than the supremum of dT/dC_A in the case of reverse beam shaping. In either case, the valid interval of C_A is from zero to

$C_{A,\min}$ or $C_{A,\max}$. $C_{A,\min}$ and $C_{A,\max}$ are command voltages corresponding to A_{\min} or A_{\max} shown in Tables 139.II and 139.III. The inversion function T_0^{-1} is numerically calculated.

Since the fluence is the quantity measured directly, it is more useful to express the above iteration formula in terms of fluences. Since the objective fluence map F_{obj} is $T_{\text{obj}} \times F_{\text{init}}$, where F_{init} is the initial fluence map,

$$C_{A,1} = T_0^{-1}(F_{\text{obj}}/F_{\text{init}}), \quad (15)$$

$$C_{A,n+1} = C_{A,n} - \frac{1}{(dT/dC_A)_{\max}} [F(C_{A,n}) - F_{\text{obj}}]/F_{\text{init}}.$$

The iteration does not start if $|F_{\text{init}}| < \epsilon$ or $|F_{\text{init}} - F_{\text{obj}}| < \epsilon$ since it suggests that there is either no beam to shape or no need to shape. C_A locally corresponding to these conditions is fixed at 0 for normal mode or at $C_{A,\max}$ for diffractive mode. The iteration stops if $|F(C_{A,n}) - F_{\text{obj}}| < \epsilon$ or if $C_{A,n} > C_{A,\min}$ for normal mode or if $C_{A,n} < 0$ for diffractive mode. The second criterion is needed when F_{obj} is specified to be much smaller than the system can handle. For example, the minimum transmission of a rectangular carrier can be a few percent higher for a certain LCOS-SLM model with a low fill factor, while the objective transmission can be ideally set to 0%. Unable to reach the solution, the iteration will keep increasing $C_{A,n}$ past the minimum (same as A_{\min} in Table 139.II). Setting an upper limit to $C_{A,n}$ will prevent this runaway situation.

Equations (12) and (15) can be rewritten using gain parameters (g_W and g_A) that are positive and smaller than 1:

$$C_{W,n+1} = C_{W,n} + g_W [W_{\text{obj}} - W(C_{W,n})] \quad (16)$$

and

$$C_{A,n+1} = C_{A,n} \pm g_A [F(C_{A,n}) - F_{\text{obj}}]/F_{\text{init}}, \quad (17)$$

where positive and negative signs in front of g_A correspond to normal and diffractive modes, respectively.

Application in Gain Precompensation for a Nd:Glass Amplifier

The Multi-Terawatt (MTW) laser at LLE consists of an OPCPA front end and two glass amplifiers.¹⁰ The OPCPA front end consists of three OPA stages—one before and two after the stretcher. The preamplification before the stretcher improves

the pulse contrast.¹¹ The two OPA stages after the stretcher amplify the pulse up to ~200 mJ. The first main amplifier after the OPCPA front end is a 25-mm-diam Nd:glass rod amplifier (RA) in a double-pass configuration. The second main amplifier is made of four 400-mm-aperture disks installed in a zigzag formation at the Brewster angle. The 200-mJ pulse from the OPCPA front end is amplified to 2 J through the RA and can be boosted up to 120 J by four passes through the disk amplifier. The amplified pulse is then compressed and sent to the target chamber. The schematic of the whole system is shown in Fig. 139.44(a). The SLM is placed between the OPCPA front-end output and the RA at an image plane. A more-detailed schematic of this part of the system is shown in Fig. 139.44(b). The square output beam from the OPCPA front end is anamorphically imaged to the rectangular area of the SLM (see **Improvement in the Open-Loop Algorithm**, p. 199). It is restored back to the original square beam by double-passing the same anamorphic imaging system. A static phase corrector in front of the SLM cancels the intrinsic wavefront error in the SLM.² The beam is shaped to a gain-precompensated profile by the SLM using the normal-mode carrier method. After the SLM, the beam is switched out by polarization optics and imaged to the exit surface of the RA. On double-passing the RA, the amplified pulse is magnified and imaged to the disk amplifier. A sample of the injection beam to the disk amplifier is picked off by an uncoated mirror blank and imaged to a wavefront sensor.

The anamorphic image relay (AIR) is made of two pairs of cylindrical lenses. The outer and inner pairs of cylindrical

lenses separately image the horizontal and vertical dimensions with different magnifications. The 13 × 13-mm² input beam is transformed into a 12 × 16-mm² beam on the SLM. An AIR works for only a fixed object distance. The error in the object distance is recovered by adjusting the image distance, but only in one dimension in an AIR. The tolerance in object positioning within which the imaging conditions in horizontal and vertical dimensions remain the same can be derived by using the Maréchal criterion for the defocus term as

$$Az_{\text{obj}} \leq \frac{D^2}{\lambda \Delta M^2}, \quad (18)$$

where $\Delta M^2 = |M_x^2 - M_y^2|$ and D is the smallest feature size of the object. With a few-hundred-micron feature size in the beam and $\Delta M^2 = 0.66$, the positioning tolerance is tens of millimeters.

The full utilization of the rectangular area of the SLM reduces the peak fluence by 25% and allows for a safer operation below the damage threshold of the SLM. The damage threshold of LCOS samples, which were the same kind as used in the device, was found to be 230 mJ/cm² using the same 2.5-ns OPCPA pulses running at 5 Hz. The peak fluence of the anamorphically imaged beam on the SLM at the maximum OPCPA energy (200 mJ) does not exceed 160 mJ/cm². The AIR does not require a vacuum system; there is a large separation between the sagittal and tangential focal planes, significantly reducing the intensity near the focus.

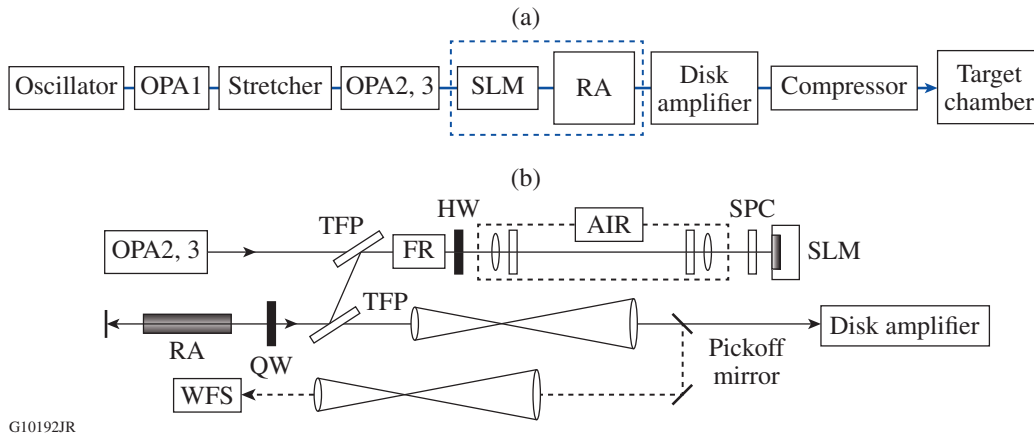


Figure 139.44

(a) Overall schematic of the Multi-Terawatt (MTW) laser; (b) detailed schematic of the MTW beam-shaping system. The image relay shown between the rod amplifier (RA) and disk amplifier is a simplified representation. TFP: thin-film polarizer; FR: Faraday rotator; HW: half-wave plate; QW: quarter-wave plate; SPC: static phase corrector; WFS: wavefront sensor; AIR: anamorphic image relay.

The reflection from the antireflective (AR)-coated first surface of the SLM cover glass introduces a prepulse 30 ps before the main pulse, down at the -40-dB level. This is not acceptable for experiments requiring a high-contrast pulse. The SLM was customized with a wedged cover glass to eliminate the prepulse; the wedge angle was 4.1 mrad. An alternative would be diffractive-mode beam shaping, where the prepulse from the cover glass is automatically separated from the main pulse.

The beam profile at the diagnostic wavefront sensor [WFS in Fig. 139.44(b)] before and after the amplification in the rod amplifier is shown in Fig. 139.45. The relatively uniform input OPCPA beam profile shown in Fig. 139.45(a) is highly distorted at the bottom corners after amplification in the rod amplifier [Fig 139.45(b)].

Based on the two fluence maps measured before and after the amplification, a gain-precompensated fluence map, or an objective map, can be designed that will become uniform on

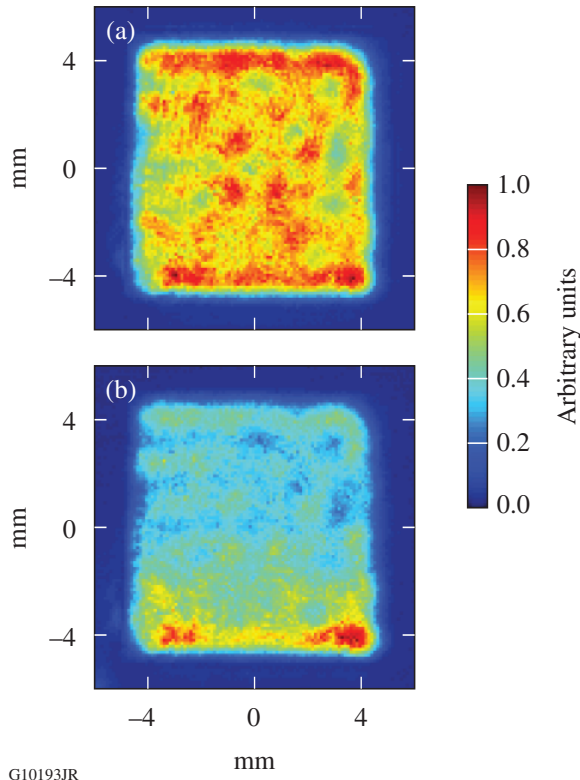


Figure 139.45
Beam profile (a) before and (b) after amplification through the rod amplifier. The lower bottom corners of the beam become hot after amplification. The dimensions of the images correspond to camera space in the diagnostic beam path.

amplification. Assuming the objective is a super-Gaussian beam, the objective fluence has the following form:

$$F_{\text{obj}} = F_{\text{peak}} \times F_0 \times T_{\text{gain}}, \quad (19)$$

where F_{peak} is a constant that adjusts the maximum objective fluence and F_0 is a super-Gaussian beam profile usually expressed as

$$F_0 = \exp \left\{ - \left[\left(\frac{x - x_c}{R_x} \right)^m + \left(\frac{y - y_c}{R_y} \right)^m \right] \right\}. \quad (20)$$

T_{gain} is a map of the ratio between the fluences before and after amplification:

$$T_{\text{gain}} = \frac{F_{\text{init}}}{F_{\text{amp}}}, \quad (21)$$

where F_{init} and F_{amp} correspond to Figs. 139.45(a) and 139.45(b), respectively.

The ratio map calculated as above cannot be directly used because it is not well defined where the denominator is close to or equal to zero. A special region of interest is created to avoid this problem and to add stability in a 2-D polynomial fit. The region of interest consists of an interior region and an exterior rectangular frame as shown in Fig. 139.46. In the interior region

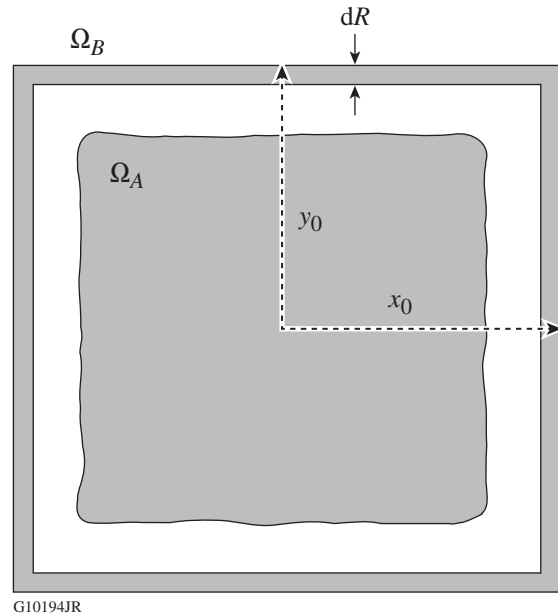


Figure 139.46
Region of interest for polynomial fit.

(Ω_A) the signal level of both F_{init} and F_{amp} is above 5% of the maximum signal level. The outer region (Ω_B) is a region of the rectangular frame. The coefficients for a set of 2-D Legendre polynomials are calculated to fit the measured gain ratio within the interior region and all zeros in the exterior frame region. The zeros in the frame stabilize the edge of the polynomials. The outer region has dimensions of $2x_0 \times 2y_0$ with the frame thickness dR . There is a no strict rule to setting x_0 , y_0 , and dR . The frame size should be large enough to cover the interior region but not bigger than the camera area; dR should be set thin enough to provide the best numerical fit. The number of modes used in this case was 240. The polynomial representation of T_{gain} is normalized to 1 at the end.

The polynomial fit in combination with the super-Gaussian envelope F_0 provides a smooth objective profile that can be experimentally achieved. In Eq. (19), F_{peak} is a single number that can be adjusted from zero to a few times the maximum of F_{init} ; F_{peak} is set as high as possible to minimize the energy loss from beam shaping.

As a final step, the part of the objective map accidentally set higher than F_{init} is set to F_{init} and set to zero where it is negative. The remaining sharp features are low-pass filtered.

Figure 139.47(a) shows the beam-shaping result precompensating the gain nonuniformity in the amplifier shown in Fig. 139.45(b). The precompensated beam is restored to a flat beam profile after amplification as shown in Fig. 139.47(b). It takes only 30 min from the measurement of an uncompensated RA beam to a design of an objective map and a completion of the closed loop. The beam shape is maintained at near-optimum condition in daily operations by rerunning the closed loop.

The beam uniformity achieved in the RA stage is not degraded as the beam passes through the next amplifier,

which is the disk amplifier. The profile of a 39-J beam at the output of the disk amplifier near an image plane is shown in Fig. 139.48. Improvement in beam uniformity helps to operate the system under safe conditions by keeping the maximum fluence below the damage threshold of the compressor gratings. The maximum fluence of this beam is 1.1 J/cm^2 , whereas the damage threshold of the grating is 1.5 J/cm^2 at 10 ps measured by N -on-1 tests.

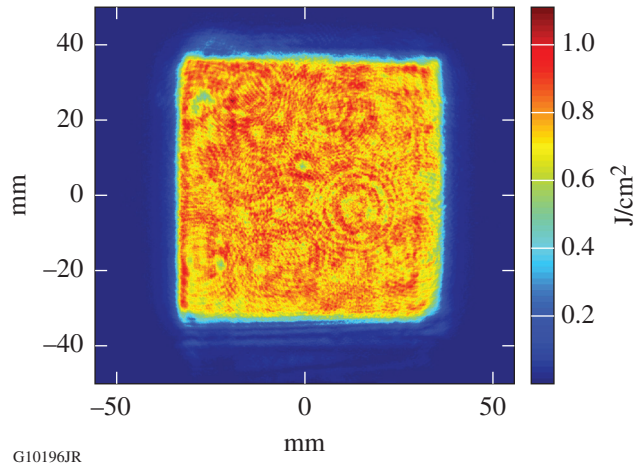


Figure 139.48
Beam profile of the disk-amplifier output near an image plane. The energy in the beam is 39 J and the full width at half maximum is 70 mm.

Conclusions

The previous carrier-beam-shaping method using an SLM has been improved in both open-loop and closed-loop algorithms. The improvements to the open-loop algorithm are based on using a measured transmission function rather than a theoretical function. The measured function can still be expressed as a simple analytic function with three parameters specific to the device and the carrier type. A new search method dubbed as the constant maximum-derivative Newton method improves

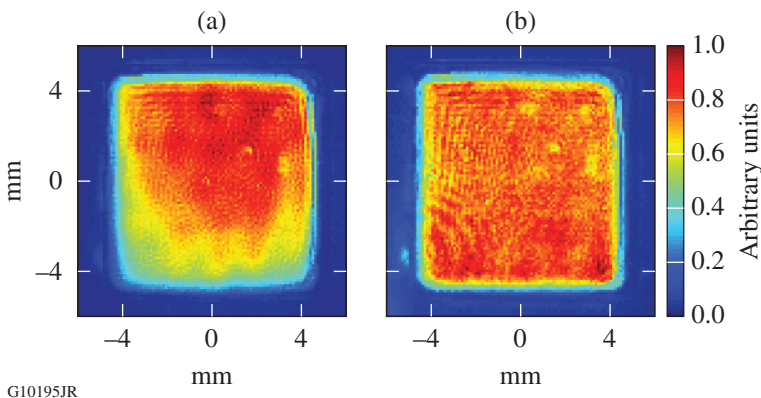


Figure 139.47
Precompensated beam profile (a) before and (b) after amplification through the RA. The lower bottom corners of the beam are attenuated before amplification and become even after amplification.

the closed-loop algorithm in terms of convergence stability and speed. The details of both wavefront- and fluence-shaping closed-loop algorithms were summarized in Eqs. (16) and (17). A new method of carrier-beam shaping using a sawtooth carrier and the first-order diffraction as the main beam was explored. It has a fail-safe feature and higher beam contrast, which might be useful in some applications.

The beam-shaping system was implemented in a multi-terawatt OPCPA laser. The gain precompensation of a 200-mJ, 2.5-ns OPCPA laser beam improves the beam uniformity of the next-stage amplification. The objective map for the precompensation is designed based on pre- and post-amplification beam profiles. The improved uniformity in the precompensated amplified beam is striking in that it is better than the unamplified OPCPA input beam. The improved uniformity in the amplified beam through the RA with the help of beam shaping allows for a safer energy ramp in the next-stage boost amplifier and a better protection of the gratings in the pulse compressor. The best beam shape can be maintained thanks to the dynamic adjustability of the beam shaper regardless of the small daily changes in the OPCPA beam profile and the gain response in the rod amplifier.

Other important issues were also addressed in applying the SLM-based beam-shaping system to a high-energy laser. The device can be run safely below the damage threshold even at full OPCPA energy by utilizing the entire available SLM area. This is done by anamorphically imaging a square input beam onto the rectangular area of the SLM. The prepulse coming from the SLM's front surface, which adversely affects a solid-target experiment, was eliminated by using a customized wedged cover glass.

With future improvements in the damage threshold and the bandwidth of a liquid crystal device that can be used with the carrier-beam-shaping method, a beam-shaping system similar to the one described in this article may find a broader application in improving laser performance.

ACKNOWLEDGMENT

This material is based upon work supported by the Department of Energy National Nuclear Security Administration under Award Number DE-NA0001944, the University of Rochester, and the New York State Energy Research and Development Authority. The support of DOE does not constitute an endorsement by DOE of the views expressed in this paper.

REFERENCES

1. V. Bagnoud and J. D. Zuegel, *Opt. Lett.* **29**, 295 (2004).
2. S.-W. Bahk, E. Fess, B. E. Kruschwitz, and J. D. Zuegel, *Opt. Express* **18**, 9151 (2010).
3. M. Barczys, S.-W. Bahk, M. Spilatro, D. Coppenbarger, E. Hill, T. H. Hinterman, R. W. Kidder, J. Puth, T. Touris, and J. D. Zuegel, in *High Power Lasers for Fusion Research II*, edited by A. A. S. Awwal (SPIE, Bellingham, WA, 2013), Vol. 8602, Paper 86020F.
4. C. Dorrer and J. D. Zuegel, *J. Opt. Soc. Am. B* **24**, 1268 (2007).
5. J. Heebner *et al.*, in *High Power Lasers for Fusion Research*, edited by A. A. S. Awwal, A. M. Dunne, H. Azechi, and B. E. Kruschwitz (SPIE, Bellingham, WA, 2011), Vol. 7916, Paper 79160H.
6. S.-W. Bahk, J. D. Zuegel, J. R. Fienup, C. C. Widmayer, and J. Heebner, *Appl. Opt.* **47**, 6586 (2008).
7. M. J. Guardalben and L. J. Waxer, in *High Power Lasers for Fusion Research*, edited by A. A. S. Awwal, A. M. Dunne, H. Azechi, and B. E. Kruschwitz (SPIE, Bellingham, WA, 2011), Vol. 7916, Paper 79160G.
8. T. Zhao *et al.*, *J. Mod. Opt.* **60**, 109 (2012).
9. S. Ngcobo *et al.*, *Nat. Commun.* **4**, 2289 (2013).
10. V. Bagnoud, J. Puth, I. Begishev, M. Guardalben, J. D. Zuegel, N. Forget, and C. Le Blanc, in *Conference on Lasers and Electro-Optics/Quantum Electronics and Laser Science and Photonic Applications, Systems and Technologies*, Technical Digest (CD) (Optical Society of America, Washington, DC, 2005), Paper JFA1.
11. C. Dorrer, I. A. Begishev, A. V. Okishev, and J. D. Zuegel, *Opt. Lett.* **32**, 2143 (2007).

A New Neutron Time-of-Flight Detector for Fuel-Areal-Density Measurements on OMEGA

The areal density of the compressed core is an important observable in inertial confinement fusion¹ (ICF) experiments. The most-common method to infer the fuel areal density in cryogenic deuterium–tritium (DT) implosions uses the primary 14.1-MeV neutrons that elastically scatter off the deuterons and tritons in the dense shell surrounding the hot spot.² There are two independent diagnostics on OMEGA³ to measure the fuel areal density. The first one is the magnetic recoil spectrometer (MRS),⁴ which measures the forward-scattered neutron spectrum between 10 and 12 MeV. The second is a neutron time-of-flight (nTOF) detector in a well-collimated line of sight (LOS), which measures backscattered neutrons⁵ between 1 and 6 MeV. Simultaneous fuel-areal-density measurements by the MRS and nTOF, which view the target from different directions, make it possible to study implosion asymmetries on OMEGA. This article describes recent improvements and modifications to the nTOF system for the fuel areal density on OMEGA.

A neutron time-of-flight spectrum for a cryogenic DT implosion with an areal density of 220 mg/cm² and a T_i of 2.4 keV for a detector at 13.4 m from the target is shown in Fig. 139.49. This spectrum was generated using one-dimensional (1-D) *LILAC*⁶ simulations and post-processed in *IRIS*.⁷ The spectrum consists of at least six separate neutron contributions and has a dynamic range of 10⁶. The dominant DT peak is estimated to deposit more than 90% of the neutron energy into a scintillator-based nTOF detector. Such a large signal may saturate the photomultiplier tube (PMT) and produce a long light-afterglow component in the scintillator.⁸ At least four gated PMT's with different sensitivities are required to cover the full dynamic range of the entire neutron spectrum.

To mitigate the long light-afterglow component, advanced scintillating compounds were developed including a liquid scintillator based on oxygenated xylene⁹ and a solid bibenzyl crystal.¹⁰ The maximum diameter of the scintillator cavity (8 in.) is determined by the maximum available distance from the target on OMEGA (13.4 m) and the diameter of the hole in the concrete floor of the Target Bay that is used as a second collimator.⁵ The thickness of the scintillator cavity was chosen

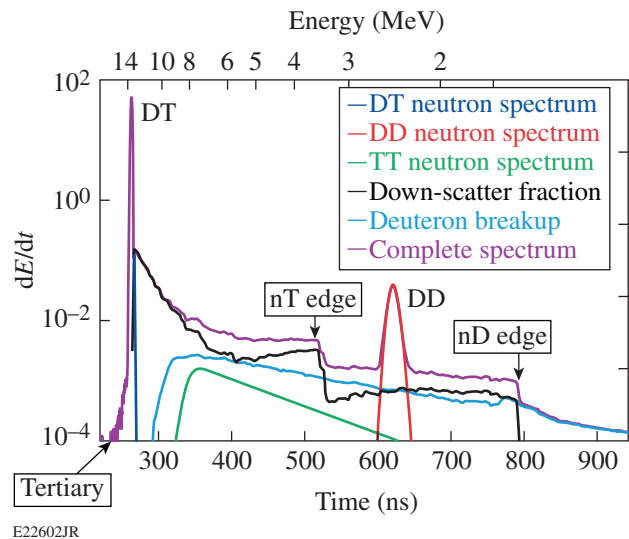


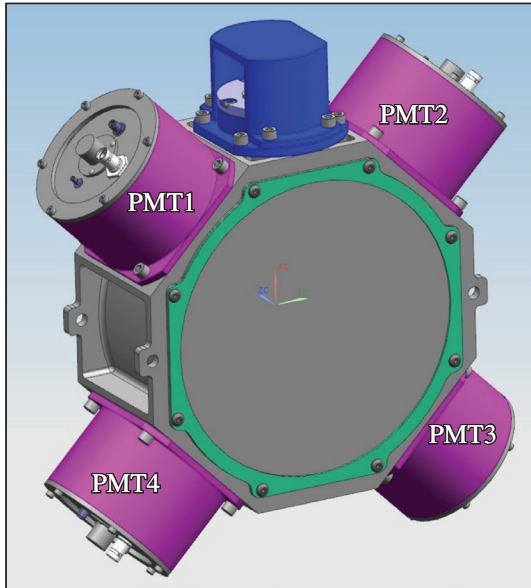
Figure 139.49

A neutron time-of-flight spectrum is generated for a cryogenic DT implosions on OMEGA.

to be 4 in. to ensure adequate neutron statistics for the yields available with cryogenic DT shots on OMEGA.

The new 8 × 4 nTOF detector is a modification and improvement of the nTOF20-Spec detectors¹¹ for the National Ignition Facility (NIF) and 6 × 2 nTOF detector⁵ on OMEGA. The number of PMT's was increased from two to four; the scintillator volume was increased by a factor of 2.7; the mass of material in the detector body was decreased as much as possible; and compartments for neutral-density filters between windows and PMT's were eliminated. A computer-aided design (CAD) model of the new 8 × 4 nTOF detector is shown in Fig. 139.50. The main part of the detector is a thin-wall, stainless-steel scintillator cavity with five holes machined from a single piece of metal. The inside cavity dimensions are 8 in. diameter by 4 in. thick. To decrease the chemical-reaction surface area, the cavity and thin stainless-steel covers were electropolished after manufacturing. The four larger holes have 50-mm fused-silica windows. Four PMT housings were designed to accommodate Photek¹² PMT240 or PMT140 gated microchannel plate (MCP)

photomultipliers with a 40-mm photocathode. The 3-cm hole on the top is used to fill the cavity with a scintillator and is covered with an expansion bellows after filling. Two flat stainless-steel covers seal the scintillator cavity on the front and back of the detector. For ion-temperature measurements, optional indented covers can be used instead, thereby reducing the scintillator thickness from 10 to 5 cm.



E22603JR

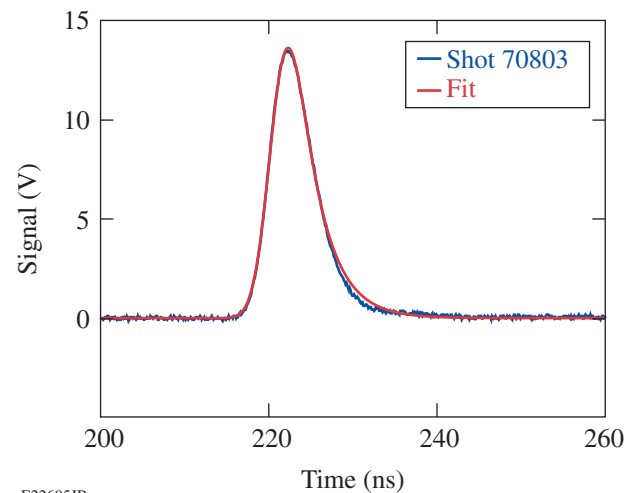
Figure 139.50
A computer model of the 8×4 nTOF detector.

The 8×4 nTOF is mounted to the ceiling beneath the Target Bay at 13.4 m from the target. The mid-beam collimator⁵ was modified to project a 19-cm-diam neutron beam to the face of the 8×4 nTOF detector. To decrease neutron scattering, the 20-mm-thick quartz vacuum window to the target chamber was replaced by a 1.9-mm stainless-steel window.

One PMT140 and three PMT240's were installed on the 8×4 nTOF. The low-gain PMT140 measures the primary DT neutron signal; the first PMT240 measures DT areal density in the nT-edge region from 1.5 to 6 MeV, the second PMT240 measures DT areal density in the nD-edge region below 2-MeV, and the third PMT240 is used for testing. We use the most-recent fast-gated Photek PMT240's with a meshed photocathode and fast GM300-8U gate units that together provide a gate recovery time of about 15 ns. The signals from each of the four PMT's are transmitted by 6-m-long LMR-600 cables to four 1-GHz, 10-GS/s Tektronix DPO7104 oscilloscopes. A resistive splitter divides the PMT signal into four oscilloscope channels with

different sensitivity settings to increase the dynamic range of the recording system.

The primary DT neutrons are measured by the ungated PMT140 with a gain of 50. Figure 139.51 shows the typical scope trace of the neutron signal from the PMT140 taken for a cryogenic shot with a DT yield of 2.3×10^{13} . The signal in Fig. 139.51 was fitted by a convolution¹³ of a Gaussian and exponential scintillator decay to calculate the total charge. Such a fit approximates the measured signal very well without any rescattering tails. This 8×4 nTOF detector channel was calibrated for a primary DT yield against the 12-m nTOF-H detector¹⁴ with a statistical precision of 3.5% rms (root mean square).



E22605JR

Figure 139.51
Neutron signal recorded for the PMT140 on a DT shot with a yield of 2.3×10^{13} .

Figure 139.52 shows the scope traces from the PMT240 with a gain of 400 for three cryogenic shots in the nT-edge region, normalized to the primary DT yield. The DT neutron peak was gated out; the small peak at 215 ns is a result of direct interactions of rescattered neutrons with the MCP's in the PMT. The gate was turned off at 300 ns for two of the shots and at 320 ns for the third shot. The nT edge at ~ 470 ns is clearly visible, as is the difference in areal density between shots. An analysis of these shots, as described in Ref. 5, produced areal densities of 165 mg/cm^2 , 124 mg/cm^2 , and 174 mg/cm^2 . The nD edge at 730 ns is barely visible in Fig. 139.52.

A scope trace from a different PMT240 with a gain 1×10^4 for an nD-edge region measurement is shown in Fig. 139.53. The gate-out region for this PMT was extended to the end of the DD neutron peak at 600 ns (see Fig. 139.52). The PMT can

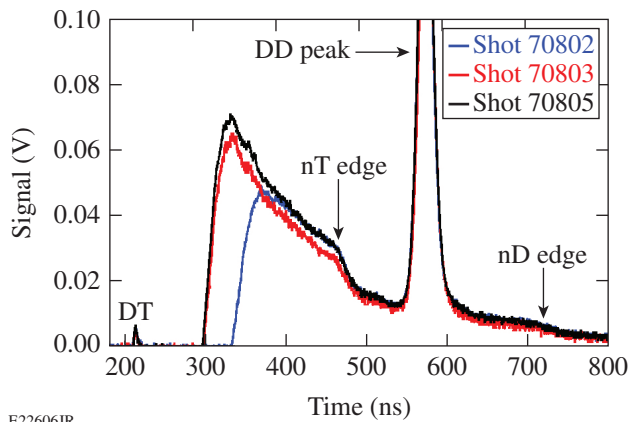


Figure 139.52
Neutron signal recorded for the gated PMT240 on DT cryogenic shots 70802, 70803, and 70805.

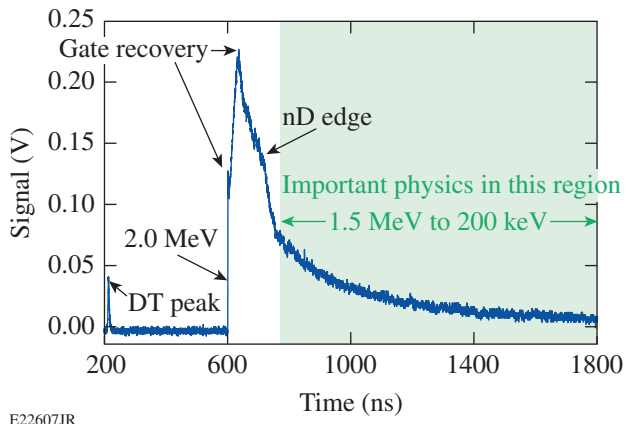


Figure 139.53
Neutron signal recorded for the gated PMT240 on DT cryogenic shot 69239 with a yield of 1.8×10^{13} .

be operated at a much higher gain if the primary DD peak is eliminated with the gate. As in Fig. 139.52, the direct interaction of DT neutrons with the MCP can be seen at 215 ns; gate recovery can be seen from 600 ns to 615 ns, and the nD edge is now clearly visible at 730 ns. The areal density from the nD edge is inferred based on an analysis similar to that used for the nT edge. Recent areal-density measurements from the nT- and nD-edge regions are compared in Table 139.IV. There is good agreement between areal densities measured in nT- and nD-edge regions. The signal below the nD edge (1.56 MeV) consists of the residual neutron-scattering background, T-T reactions, and a deuteron breakup reaction. All these contributions are currently under study.

Table 139.IV: Comparison of areal densities measured in nT- and nD-edge regions.

Shot number	nT areal density (mg/cm ²)	nD areal density (mg/cm ²)
71527	158	166
71528	180	177
71529	166	175
71530	187	179

The fourth PMT was used to investigate the possibility of measuring tertiary¹⁵ neutrons with energies larger than the primary 14.06-MeV neutrons. The yield of the tertiary neutrons is about 10^{-6} from the primary D-T yield and they appear just before the rising edge of the DT peak. To record tertiary neutrons, a high-gain PMT is needed that is sensitive only during the short arrival time window before the DT peak. The most-recent Photech PMT's have a normally off-gating option that is ideal for tertiary neutron measurements. Figure 139.54 shows raw scope traces from the PMT240 with a gain of 10^6 that were recorded on three different shots using the same PMT, scope, and different gate timing. Shot 69233 (blue trace) was recorded in the normally on-gating option in an x-ray-producing shot and shows the position of the x-ray peak in time. Shot 69236 (red trace) was recorded in the normally off-gating mode without any gate pulse and showed the position of the DT peak from direct interaction of neutrons with the MCP at 220 ns. Shot 69242, with a primary yield of 1.8×10^{13} , was recorded with the normally off-gating mode and a 160-ns-wide gate-opening pulse. Figure 139.54 shows that the gate eliminates the hard x rays and most of the DT pulse. The rising edge of the DT pulse saturates the scope after 215 ns, causing oscillation in the signal. However, the scope survives and is fully operational after several similar tests. The data at

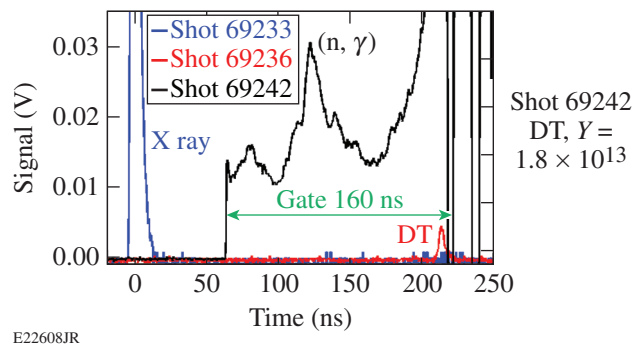


Figure 139.54
X-ray and neutron signals recorded for the normally off-gated PMT240 with a gain of 10^6 on shots 69233, 69236, and 69242.

~180 ns (shown in Fig. 139.54) are most probably from neutron interactions with structures in the target area. The technical ability to measure neutrons with an energy of more than 14 MeV was demonstrated using the nTOF technique. Tertiary measurements on OMEGA are extremely difficult because the areal density is relatively low and the 8×4 nTOF detector is not sufficiently shielded from gammas. On the NIF, where yields and areal densities are higher and the nTOF detectors in the “neutron alcove” are well-shielded, the situation is much more favorable.

The new 8×4 nTOF detector with four gated PMT’s each with different gains makes it possible for the primary DT and D₂ neutrons to be measured on the same shot on the same LOS. Fuel areal densities can be inferred from down-scattered neutrons in the nT- and nD-edge regions, and tertiary neutrons can be studied using the same detector. The 8×4 nTOF is now the main detector for areal-density measurements on OMEGA.

ACKNOWLEDGMENT

This work was partially supported by the Department of Energy National Nuclear Security Administration under Award No. DE-NA0001944, the University of Rochester, and the New York State Energy Research and Development Authority. The support of DOE does not constitute an endorsement by DOE of the views expressed in this article.

REFERENCES

1. J. D. Lindl, *Inertial Confinement Fusion: The Quest for Ignition and Energy Gain Using Indirect Drive* (Springer-Verlag, New York, 1998).
2. C. D. Zhou and R. Betti, *Phys. Plasmas* **15**, 102707 (2008).
3. T. R. Boehly, D. L. Brown, R. S. Craxton, R. L. Keck, J. P. Knauer, J. H. Kelly, T. J. Kessler, S. A. Kumpan, S. J. Loucks, S. A. Letzring, F. J. Marshall, R. L. McCrory, S. F. B. Morse, W. Seka, J. M. Soures, and C. P. Verdon, *Opt. Commun.* **133**, 495 (1997).
4. J. A. Frenje, D. T. Casey, C. K. Li, J. R. Rygg, F. H. Séguin, R. D. Petrasso, V. Yu. Glebov, D. D. Meyerhofer, T. C. Sangster, S. Hatchett, S. Haan, C. Cerjan, O. Landen, M. Moran, P. Song, D. C. Wilson, and R. J. Leeper, *Rev. Sci. Instrum.* **79**, 10E502 (2008).
5. C. J. Forrest, P. B. Radha, V. Yu. Glebov, V. N. Goncharov, J. P. Knauer, A. Pruyne, M. Romanofsky, T. C. Sangster, M. J. Shoup III, C. Stoeckl, D. T. Casey, M. Gatu-Johnson, and S. Gardner, *Rev. Sci. Instrum.* **83**, 10D919 (2012).
6. J. Delettrez, R. Epstein, M. C. Richardson, P. A. Jaanimagi, and B. L. Henke, *Phys. Rev. A* **36**, 3926 (1987).
7. P. B. Radha, J. A. Delettrez, R. Epstein, S. Skupsky, J. M. Soures, S. Cremer, and R. D. Petrasso, *Bull. Am. Phys. Soc.* **44**, 194 (1999).
8. C. Stoeckl, M. Cruz, V. Yu. Glebov, J. P. Knauer, R. Lauck, K. Marshall, C. Mileham, T. C. Sangster, and W. Theobald, *Rev. Sci. Instrum.* **81**, 10D302 (2010).
9. R. Lauck *et al.*, *IEEE Trans. Nucl. Sci.* **56**, 989 (2009).
10. V. Yu. Glebov, C. Forrest, J. P. Knauer, A. Pruyne, M. Romanofsky, T. C. Sangster, M. J. Shoup III, C. Stoeckl, J. A. Caggiano, M. L. Carman, T. J. Clancy, R. Hatarik, J. McNaney, and N. P. Zaitseva, *Rev. Sci. Instrum.* **83**, 10D309 (2012).
11. V. Yu. Glebov, T. C. Sangster, C. Stoeckl, J. P. Knauer, W. Theobald, K. L. Marshall, M. J. Shoup III, T. Buczek, M. Cruz, T. Duffy, M. Romanofsky, M. Fox, A. Pruyne, M. J. Moran, R. A. Lerche, J. McNaney, J. D. Kilkenny, M. J. Eckart, D. Schneider, D. Munro, W. Stoeffl, R. Zacharias, J. J. Haslam, T. Clancy, M. Yeoman, D. Warwas, C. J. Horsfield, J.-L. Bourgade, O. Landoas, L. Disdier, G. A. Chandler, and R. J. Leeper, *Rev. Sci. Instrum.* **81**, 10D325 (2010).
12. Photek Ltd., St. Leonards-on-Sea, East Sussex, TN38 9NS, United Kingdom.
13. T. J. Murphy, R. E. Chrien, and K. A. Klare, *Rev. Sci. Instrum.* **68**, 610 (1997).
14. V. Yu. Glebov, C. Stoeckl, T. C. Sangster, S. Roberts, G. J. Schmid, R. A. Lerche, and M. J. Moran, *Rev. Sci. Instrum.* **75**, 3559 (2004).
15. H. Azechi, M. D. Cable, and R. O. Stapf, *Laser Part. Beams* **9**, 119 (1991).

Publications and Conference Presentations

Publications

- D. Batani, S. Baton, A. Casner, S. Depierreux, M. Hohenberger, O. Klimo, M. Koenig, C. Labaune, X. Ribeyre, C. Rousseaux, G. Schurtz, W. Theobald, and V. T. Tikhonchuk, "Physics Issues for Shock Ignition," *Nucl. Fusion* **54**, 054009 (2014).
- H.-M. P. Chen, J. J. Ou, and S. H. Chen, "Glassy Liquid Crystals as Self-Organized Films for Robust Optoelectronic Devices," in *Nanoscience with Liquid Crystals: From Self-Organized Nanostructures to Applications*, edited by Q. Li, Springer Series in NanoScience and Technology (Springer, Switzerland, 2014), Chap. 6, pp. 179–208.
- V. N. Goncharov, T. C. Sangster, R. Betti, T. R. Boehly, M. J. Bonino, T. J. B. Collins, R. S. Craxton, J. A. Delettrez, D. H. Edgell, R. Epstein, R. K. Follett, C. J. Forrest, D. H. Froula, V. Yu. Glebov, D. R. Harding, R. J. Henchen, S. X. Hu, I. V. Igumenshchev, R. Janezic, J. H. Kelly, T. J. Kessler, T. Z. Kosc, S. J. Loucks, J. A. Marozas, F. J. Marshall, A. V. Maximov, R. L. McCrory, P. W. McKenty, D. D. Meyerhofer, D. T. Michel, J. F. Myatt, R. Nora, P. B. Radha, S. P. Regan, W. Seka, W. T. Shmayda, R. W. Short, A. Shvydky, S. Skupsky, C. Stoeckl, B. Yaakobi, J. A. Frenje, M. Gatu-Johnson, R. D. Petrasso, and D. T. Casey, "Improving the Hot-Spot Pressure and Demonstrating Ignition Hydrodynamic Equivalence in Cryogenic Deuterium–Tritium Implosions on OMEGA," *Phys. Plasmas* **21**, 056315 (2014) (invited).
- D. Haberberger, S. Ivancic, S. X. Hu, R. Boni, M. Barczys, R. S. Craxton, and D. H. Froula, "Measurements of Electron Density Profiles Using an Angular Filter Refractometer," *Phys. Plasmas* **21**, 056304 (2014) (invited).
- J. D. Hager, T. J. B. Collins, V. A. Smalyuk, J. P. Knauer, D. D. Meyerhofer, and T. C. Sangster, "Study of Rayleigh–Taylor Growth in Laser Irradiated Planar SiO₂ Targets at Ignition-Relevant Conditions," *Phys. Plasmas* **20**, 072707 (2013).
- D. R. Harding, H. Goodrich, A. Caveglia, and M. Anthamatten, "Effect of Temperature and Volume on the Tensile and Adhesive Properties of Photocurable Resins," *J. Polym. Sci. B, Polym. Phys.* **52**, 936 (2014).
- S. X. Hu, T. R. Boehly, and L. A. Collins, "Properties of Warm Dense Polystyrene Plasmas Along the Principal Hugoniot," *Phys. Rev. E* **89**, 063104 (2014).
- S. X. Hu, L. A. Collins, T. R. Boehly, J. D. Kress, V. N. Goncharov, and S. Skupsky, "First-Principles Thermal Conductivity of Warm-Dense Deuterium Plasmas for Inertial Confinement Fusion Applications," *Phys. Rev. E* **89**, 043105 (2014).
- I. V. Igumenshchev, A. B. Zylstra, C. K. Li, P. M. Nilson, V. N. Goncharov, and R. D. Petrasso, "Self-Generated Magnetic Fields in Direct-Drive Implosion Experiments," *Phys. Plasmas* **21**, 062707 (2014).
- V. V. Ivanov, A. A. Anderson, D. Papp, B. R. Talbot, J. P. Chittenden, N. Niasse, and I. A. Begishev, "UV Laser-Probing Diagnostics for the Dense Z Pinch," *IEEE Trans. Plasma Sci.* **42**, 1153 (2014).
- J. F. Myatt, J. Zhang, R. W. Short, A. V. Maximov, W. Seka, D. H. Froula, D. H. Edgell, D. T. Michel, I. V. Igumenshchev, D. E. Hinkel, P. Michel, and J. D. Moody, "Multiple-Beam Laser–Plasma Interactions in Inertial Confinement Fusion," *Phys. Plasmas* **21**, 055501 (2014) (invited).
- T. Nagayama, R. C. Mancini, R. Florido, D. Mayes, R. Tommasini, J. A. Koch, J. A. Delettrez, S. P. Regan, and V. A. Smalyuk, "Direct Asymmetry Measurement of Temperature and Density Spatial Distributions in Inertial Confinement Fusion Plasmas from Pinhole Space-Resolved Spectra," *Phys. Plasmas* **21**, 050702 (2014).
- R. Nora, R. Betti, K. S. Anderson, A. Shvydky, A. Bose, K. M. Woo, A. R. Christopherson, J. A. Marozas, T. J. B. Collins, P. B. Radha, S. X. Hu, R. Epstein, F. J. Marshall, R. L. McCrory, T. C. Sangster, and D. D. Meyerhofer, "Theory of Hydro-Equivalent

Ignition for Inertial Fusion and Its Applications to OMEGA and the National Ignition Facility,” *Phys. Plasmas* **21**, 056316 (2014) (invited).

S. Papernov, A. A. Kozlov, J. B. Oliver, T. J. Kessler, A. Shvydky, and A. B. Marozas, “Near-Ultraviolet Absorption-Annealing in Hafnium Oxide Thin Films Subjected to Continuous-Wave Laser Radiation,” *Opt. Eng.* **53**, 122504 (2014).

P. B. Radha, M. Hohenberger, F. J. Marshall, R. S. Craxton, D. H. Edgell, D. H. Froula, V. N. Goncharov, J. A. Marozas, R. L. McCrory, P. W. McKenty, D. D. Meyerhofer, D. T. Michel, J. F. Myatt, T. C. Sangster, W. Seka, and S. Skupsky, “Polar-Drive Implosions—Results from OMEGA and the National Ignition Facility,” *Stockpile Stewardship Quarterly* **4**, 10, NNSA Office of Research, Development, Test, and Evaluation, Washington, D.C., DOE/NA-0023 (2014).

B. Rice, J. Quinzi, L. Lund, J. Ulreich, and M. Shoup, “Measurement of Young’s Modulus and Damping of Fibers at Cryogenic Temperatures,” *Cryogenics* **63**, 43 (2014).

H. G. Rinderknecht, H. Sio, C. K. Li, N. Hoffman, A. B. Zylstra, M. J. Rosenberg, J. A. Frenje, M. Gatu Johnson, F. H. Séguin, R. D. Petrasso, R. Betti, V. Yu. Glebov, D. D. Meyerhofer, T. C. Sangster, W. Seka, C. Stoeckl, G. Kagan, K. Molvig, C. Bellei, P. Amendt, O. Landen, J. R. Rygg, V. A. Smalyuk, S. Wilks, A. Greenwood, and A. Nikroo, “Kinetic Mix Mechanisms in Shock-Driven Inertial Confinement Fusion Implosions,” *Phys. Plasmas* **21**, 056311 (2014).

H. G. Rinderknecht, H. Sio, C. K. Li, A. B. Zylstra, M. J. Rosenberg, P. Amendt, J. Delettrez, C. Bellei, J. A. Frenje, M. Gatu Johnson, F. H. Séguin, R. D. Petrasso, R. Betti, V. Yu. Glebov, D. D. Meyerhofer, T. C. Sangster, C. Stoeckl, O. Landen, V. A. Smalyuk, S. Wilks, A. Greenwood, and A. Nikroo, “First Observations of Nonhydrodynamic Mix at the Fuel-Shell Interface in Shock-Driven Inertial Confinement Implosions,” *Phys. Rev. Lett.* **112**, 135001 (2014).

M. J. Rosenberg, H. G. Rinderknecht, N. M. Hoffman, P. A. Amendt, S. Atzeni, A. B. Zylstra, C. K. Li, F. H. Séguin, H. Sio, M. Gatu Johnson, J. A. Frenje, R. D. Petrasso, V. Yu. Glebov, C. Stoeckl, W. Seka, F. J. Marshall, J. A. Delettrez, T. C. Sangster, R. Betti, V. N. Goncharov, D. D. Meyerhofer, S. Skupsky, C. Bellei, J. Pino, S. C. Wilks, G. Kagan, K. Molvig, and A. Nikroo, “Exploration of the Transition from the Hydrodynamiclike to the Strongly Kinetic Regime in Shock-Driven Implosions,” *Phys. Rev. Lett.* **112**, 185001 (2014).

M. J. Rosenberg, F. H. Séguin, C. J. Waugh, H. G. Rinderknecht, D. Orozco, J. A. Frenje, M. Gatu Johnson, H. Sio, A. B. Zylstra, N. Sinenian, C. K. Li, R. D. Petrasso, V. Yu. Glebov, C. Stoeckl, M. Hohenberger, T. C. Sangster, S. LePape, A. J. Mackinnon, R. M. Bionta, O. L. Landen, R. A. Zacharias, Y. Kim, H. W. Herrmann, and J. D. Kilkenny, “Empirical Assessment of the Detection Efficiency of CR-39 at High Proton Fluence and a Compact, Proton Detector for High-Fluence Applications,” *Rev. Sci. Instrum.* **85**, 043302 (2014).

W. Seka, J. F. Myatt, R. W. Short, D. H. Froula, J. Katz, V. N. Goncharov, and I. V. Igumenshev, “Nonuniformly Driven Two-Plasmon-Decay Instability in Direct-Drive Implosions,” *Phys. Rev. Lett.* **112**, 145001 (2014).

V. A. Smalyuk, M. Barrios, J. A. Caggiano, D. T. Casey, C. J. Cerjan, D. S. Clark, M. J. Edwards, J. A. Frenje, M. Gatu-Johnson, V. Y. Glebov, G. Grim, S. W. Haan, B. A. Hammel, A. Hamza, D. E. Hoover, W. W. Hsing, O. Hurricane, J. D. Kilkenny, J. L. Kline, J. P. Knauer, J. Kroll, O. L. Landen, J. D. Lindl, T. Ma, J. M. McNaney, M. Mintz, A. Moore, A. Nikroo, T. Parham, J. L. Peterson, R. Petrasso, L. Pickworth, J. E. Pino, K. Raman, S. P. Regan, B. A. Remington, H. F. Robey, D. P. Rowley, D. B. Sayre, R. E. Tipton, S. V. Weber, K. Widmann, D. C. Wilson, and C. B. Yeaman, “Hydrodynamic Instability Growth and Mix Experiments at the National Ignition Facility,” *Phys. Plasmas* **21**, 056301 (2014).

H. X. Vu, D. F. DuBois, D. A. Russell, J. F. Myatt, and J. Zhang, “Nonlinear Development of the Two-Plasmon Decay Instability in Three Dimensions,” *Phys. Plasmas* **21**, 042705 (2014).

R. Yan, J. Li, and C. Ren, “Intermittent Laser-Plasma Interactions and Hot Electron Generation in Shock Ignition,” *Phys. Plasmas* **21**, 062705 (2014).

J. Zhang, M. Mikulics, R. Adam, D. Grützmacher, and R. Sobolewski, “Generation of THz Transients by Photoexcited Single-Crystal GaAs Meso-Structures,” *Appl. Phys. B.* **113**, 339 (2013).

A. B. Zylstra, M. Gatu Johnson, J. A. Frenje, F. H. Séguin, H. G. Rinderknecht, M. J. Rosenberg, H. W. Sio, C. K. Li, R. D. Petrasso, M. McCluskey, D. Mastro Simone, V. Yu. Glebov, C. Forrest, C. Stoeckl, and T. C. Sangster, “A Compact Neutron Spectrometer for Characterizing Inertial Confinement Fusion Implosions at OMEGA and the NIF,” *Rev. Sci. Instrum.* **85**, 063502 (2014).

Forthcoming Publications

S.-W. Bahk, I. A. Begishev, and J. D. Zuegel, “Precompensation of Gain Nonuniformity in a Nd:glass Amplifier Using a Programmable Beam-Shaping System,” to be published in *Optics Communications*.

C. Dorrer, “Analysis of Nonlinear Optical Propagation in a Longitudinal Deuterated Potassium Dihydrogen Phosphate Pockels Cell,” to be published in the *Journal of the Optical Society of America B*.

C. Dorrer, R. G. Roides, J. Bromage, and J. D. Zuegel, “Self-Phase Modulation Compensation in a Regenerative Amplifier Using Cascaded Second-Order Nonlinearities,” to be published in *Optics Letters*.

D. Eimerl, E. M. Campbell, W. F. Krupke, J. Zweiback, W. L. Kruer, J. Marozas, J. Zuegel, J. Myatt, J. Kelly, D. Froula, and R. L. McCrory, “StarDriver: A Flexible Laser Driver for Inertial Confinement Fusion and High Energy Density Physics,” to be published in the *Journal of Fusion Energy*.

R. Epstein, S. P. Regan, B. A. Hammel, L. J. Suter, H. A. Scott, M. A. Barrios, D. K. Bradley, D. A. Callahan, C. Cerjan, G. W. Collins, S. N. Dixit, T. Doepfner, M. J. Edwards, D. R. Farley, K. B. Fournier, S. Glenn, S. H. Glenzer, I. E. Golovkin,

A. Hamza, D. G. Hicks, N. Izumi, O. S. Jones, M. H. Key, J. D. Kilkenny, J. L. Kline, G. A. Kyrala, O. L. Landen, T. Ma, J. J. MacFarlane, A. J. Mackinnon, R. C. Mancini, R. L. McCrory, D. D. Meyerhofer, N. B. Meezan, A. Nikroo, H.-S. Park, P. K. Patel, J. E. Ralph, B. A. Remington, T. C. Sangster, V. A. Smalyuk, P. T. Springer, R. P. J. Town, and J. L. Tucker, “Applications and Results of X-Ray Spectroscopy in Implosion Experiments on the National Ignition Facility,” to be published in *Proceedings of Atomic Processes in Plasmas* (invited).

H. P. H. Liddell, J. C. Lambropoulos, and S. D. Jacobs, “Thermomechanical Model to Assess Stresses Developed During Elevated-Temperature Cleaning of Coated Optics,” to be published in *Applied Optics*.

F. Philippe, V. Tassin, S. Despierreux, P. Gauthier, P. E. Masson-Laborde, M. C. Monteil, P. Seytor, B. Villette, B. Lasinski, H. S. Park, J. S. Ross, P. Amendt, T. Döppner, D. E. Hinkel, R. Wallace, E. Williams, P. Michel, J. Frenje, M. Gatu-Johnson, C. K. Li, R. Petrasso, V. Glebov, C. Sorce, C. Stoeckl, A. Nikroo, and E. Giraldez, “Demonstrated High Performance of Gas-Filled Rugby-Shaped Hohlräume on Omega,” to be published in *Physics of Plasmas*.

H. G. Rinderknecht, H. Sio, J. A. Frenje, J. Magoon, A. Agliata, M. Shoup, S. Ayers, C. G. Bailey, M. Gatu Johnson, A. B. Zylstra, N. Sinenian, M. J. Rosenberg, C. K. Li, F. H. Séguin, R. D. Petrasso, J. R. Rygg, J. R. Kimbrough, A. Mackinnon, P. Bell, R. Bionta, T. Clancy, R. Zacharias, A. House, T. Döppner, H. S. Park, S. LePape, O. Landen, N. Meezan, H. Robey, V. Yu. Glebov, M. Hohenberger, C. Stoeckl, T. C. Sangster, C. Li, J. Parat, R. Olson, J. Kline, and J. Kilkenny, “A Magnetic Particle Time-of-Flight (MagPTOF) Diagnostic for Measurements of Shock- and Compression-Bang Time at the NIF,” to be published in *Review of Scientific Instruments* (invited).

M. Storm, B. Eichman, C. Orban, S. Jiang, G. Fiksel, C. Stoeckl, G. Dyer, T. Ditmire, R. Stephens, W. Theobald, J. A. Delettrez, R. R. Freeman, and K. Akli, “ K_{α} X-Ray Imaging of Laser-Irradiated, Limited-Mass Zirconium Foils,” to be published in *Physics of Plasmas*.

J. Zhang, J. F. Myatt, A. V. Maximov, R. W. Short, H. H. Vu, D. F. DuBois, and D. A. Russell, “Multibeam Two-Plasmon Decay: Linear Threshold to Nonlinear Saturation in Three Dimensions,” to be published in *Physical Review Letters*.

Conference Presentations

T. Jacobs, M. Mayton, Z. Hobbs, and S. D. Jacobs, “Cerium Oxide Polishing Slurry Reclamation: Process Improvements at Flint Creek Resources and Sydor Optics,” CEIS 14th Annual University Technology Showcase, Rochester, NY, 10 April 2014.

W. T. Shmayda, M. D. Wittman, J. Reid, N. Redden, R. Early, J. Magoon, K. Heung, S. Xiao, T. Sessions, and S. Redd, “Initial Operation of the μ TCAP Using H₂ and D₂,” Tritium Focus Group, Aiken, SC, 22–24 April 2014.

The following presentations were made at the Sixth Omega Laser Facility Users Group Workshop, Rochester, NY, 23–25 April 2014:

W. J. Armstrong, J. Puth, and R. Rombaut, “Target Diagnostic Timing Manager (TDTM).”

A. Bose, K. Woo, R. Nora, and R. Betti, “Hydrodynamic Scaling of the Deceleration Phase from OMEGA to NIF Implosions.”

A. Christopherson, R. Betti, R. Epstein, F. J. Marshall, R. Nora, P. B. Radha, C. Stoeckl, J. A. Delettrez, and C. J. Forrest, “Comprehensive Analysis of a High Adiabatic Implosion on OMEGA.”

V. N. Goncharov, T. C. Sangster, R. Betti, T. R. Boehly, T. J. B. Collins, R. S. Craxton, J. A. Delettrez, D. H. Edgell, R. Epstein, C. J. Forrest, D. H. Froula, V. Yu. Glebov, D. R. Harding, S. X. Hu, I. V. Igumenshchev, R. Janezic, J. H. Kelly, T. J. Kessler, T. Z. Kosc, S. J. Loucks, J. A. Marozas, F. J. Marshall, A. V. Maximov, R. L. McCrory, P. W. McKenty, D. D. Meyerhofer, D. T. Michel, J. F. Myatt, R. Nora, P. B. Radha, S. P. Regan, W. Seka, W. T. Shmayda, R. W. Short, A. Shvydky, S. Skupsky, C. Sorce, C. Stoeckl, B. Yaakobi, J. A. Frenje, M. Gatu Johnson, R. D. Petrasso, and D. T. Casey, “Demonstrating Ignition Hydrodynamic Equivalence in Cryogenic DT Implosions on OMEGA.”

S. Goodman, W. T. Shmayda, and N. Redden, “Evaluation of a Compact Cryotrap.”

M. C. Gregor, R. Boni, A. Sorce, C. A. McCoy, M. Millot, J. H. Eggert, P. M. Celliers, T. R. Boehly, and D. D. Meyerhofer, “The Absolute Calibration of the Streaked Optical Pyrometer at the Omega Laser Facility.”

D. Haberberger, R. Boni, M. Barczys, J. Brown, R. Huff, S. X. Hu, S. Ivancic, R. G. Roides, M. Bedzyk, R. S. Craxton, F. Ehrne, C. Stoeckl, E. Hill, R. K. Jungquist, J. Magoon, D. Mastrosimone, J. Puth, W. Seka, M. J. Shoup III, W. Theobald, D. Weiner, J. D. Zuegel, D. H. Froula, J. Moody, D. Turnbull, B. Pollock, S. Ross, and A. Harvey-Thompson, “Optical Probing Measurements on OMEGA EP.”

R. A. Hamilton, W. T. Shmayda, and N. Redden, “X-Ray Emission from DT-Filled Targets.”

E. Hill, G. Balonek, R. Cuffney, J. H. Kelly, and T. Z. Kosc, “OMEGA SSD Arbitrary Waveform Generation Installation and Activation.”

E. Hwang, R. Boni, and W. R. Donaldson, “Testing of the OMEGA Beam-Timing System.”

R. W. Kidder and C. Kingsley, “LLE Resources are Established to Provide Access to Information for External Users.”

Y. Kong, R. S. Craxton, P. W. McKenty, and C.-K. Li, “Beam-Pointing Optimization for Proton Backlighting at the National Ignition Facility.”

B. E. Kruschwitz, A. Kalb, J. Kwiatkowski, and T. Nguyen, “Co-Propagation of Short-Pulse Beams on OMEGA EP.”

J. Kwiatkowski, E. Hill, B. Ehrich, M. Heimbueger, and F. J. Marshall, “OMEGA EP Pointing, Focusing, and Timing.”

D. Mastrosimone, G. Fiksel, J. Magoon, A. Agliata, P.-Y. Chang, and D. Barnak, “Fielding MIFEDS on OMEGA.”

S. F. B. Morse, “Omega Facility Update: OLUG Recommendations and Items of General Interest.”

G. Pien, W. J. Armstrong, and M. Labuzeta, “Diagnostic Effectiveness and Availability at the Omega Laser Facility.”

C. Sorce, A. Sorce, J. Katz, R. E. Bahr, and P. M. Nilson, "Omega Laser Facility Diagnostic Highlights."

M. D. Wittman, N. Redden, J. Reid, and W. T. Shmayda, "Initial Operation of the Isotope Separation System Using Protium and Deuterium."

The following presentations were made at the Cryo Workshop, Rochester, NY, 29–30 April 2014:

D. H. Froula, A. K. Davis, D. H. Edgell, G. Fiksel, R. K. Follett, V. N. Goncharov, R. J. Henchen, H. Hu, S. X. Hu, I. V. Igumenshchev, T. J. Kessler, D. D. Meyerhofer, D. T. Michel, J. F. Myatt, P. B. Radha, T. C. Sangster, C. Stoeckl, and B. Yaakobi, "Mitigation of Cross-Beam Energy Transfer in Direct-Drive Implosions on OMEGA."

V. N. Goncharov, T. C. Sangster, R. Betti, T. R. Boehly, T. J. B. Collins, R. S. Craxton, J. A. Delettrez, D. H. Edgell, R. Epstein, C. J. Forrest, D. H. Froula, V. Yu. Glebov, D. R. Harding, S. X. Hu, I. V. Igumenshchev, R. Janezic, J. H. Kelly, T. J. Kessler, T. Z. Kosc, S. J. Loucks, J. A. Marozas, F. J. Marshall, A. V. Maximov, R. L. McCrory, P. W. McKenty, D. D. Meyerhofer, D. T. Michel, J. F. Myatt, R. Nora, P. B. Radha, S. P. Regan, W. Seka, W. T. Shmayda, R. W. Short, A. Shvydky, S. Skupsky, C. Sorce, C. Stoeckl, B. Yaakobi, J. A. Frenje, M. Gatu Johnson, R. D. Petrasso, and D. T. Casey, "Demonstrating Ignition Hydrodynamic Equivalence in Cryogenic DT Implosions on OMEGA."

R. L. McCrory, "Direct-Drive Cryogenic Implosion Workshop: Goals and Charge."

P. W. McKenty, "Hydrodynamic Modeling in 2-D and 3-D: Plans and Challenges."

J. F. Myatt, D. F. DuBois, H. X. Vu, and D. A. Russell, "Hot-Electron Production and Preheat at the Omega Laser Facility."

T. C. Sangster, V. N. Goncharov, R. Betti, T. R. Boehly, T. J. B. Collins, R. S. Craxton, J. A. Delettrez, D. H. Edgell, R. Epstein, C. J. Forrest, D. H. Froula, V. Yu. Glebov, D. R. Harding, M. Hohenberger, S. X. Hu, I. V. Igumenshchev, R. T. Janezic, J. H. Kelly, T. J. Kessler, J. P. Knauer, T. Z. Kosc, S. J. Loucks, J. A. Marozas, F. J. Marshall, A. V. Maximov, R. L. McCrory,

P. W. McKenty, D. D. Meyerhofer, D. T. Michel, J. F. Myatt, P. B. Radha, S. P. Regan, W. Seka, W. T. Shmayda, R. W. Short, A. Shvydky, S. Skupsky, C. Sorce, C. Stoeckl, B. Yaakobi, J. A. Frenje, M. Gatu Johnson, R. D. Petrasso, A. Nikroo, and M. Farrell, "Overview of Cryogenic Target Experiments."

J. B. Oliver, T. J. Kessler, B. Charles, and C. Smith, "Fabrication of a Continuous-Enfolded Grating by Ion-Beam-Sputter Deposition," SVC Techcon 2014, Chicago, IL, 3–8 May 2014.

R. Betti, "Status and Prospects for High-Energy-Density Science on High-Power Lasers in the U.S.," International Symposium on Status and Prospects of High Energy Density Science by Giant Lasers, Tokyo, Japan, 1–4 June 2014.

The following presentations were made at the 20th High-Temperature Plasma Diagnostics, Atlanta, GA, 1–5 June 2014:

P.-Y. Chang, A. Agliata, D. H. Barnak, R. Betti, G. Fiksel, D. Hassett, D. J. Lonobile, J. Magoon, M. J. Shoup III, and C. S. Taylor, "Magnetized High-Energy-Density-Physics Platform on OMEGA."

A. Davies, R. Boni, S. Ivancic, R. Brown, D. H. Froula, D. Haberberger, J. D. Moody, B. Pollock, S. Ross, and D. Turnbull, "Polarimetry Diagnostic on OMEGA EP Using a 10-ps, 263-nm Probe Beam."

A. K. Davis, D. T. Micshel, S. X. Hu, R. S. Craxton, R. Epstein, V. N. Goncharov, I. V. Igumenshchev, T. C. Sangster, and D. H. Froula, "Mass Ablation Rate Measurements in Direct-Drive Cryogenic Implosions Using X-Ray Self-Emission Images."

V. Yu. Glebov, C. J. Forrest, K. L. Marshall, M. Romanofsky, T. C. Sangster, M. J. Shoup III, and C. Stoeckl, "A New Neutron Time-of-Flight Detector for Fuel Areal-Density Measurements on OMEGA."

M. C. Gregor, R. Boni, A. Sorce, C. A. McCoy, T. R. Boehly, D. D. Meyerhofer, M. Millot, J. H. Eggert, and P. M. Celliers,

“The Absolute Calibration of the OMEGA Streaked Optical Pyrometer at the Omega Laser Facility.”

M. Hohenberger, F. Albert, N. E. Palmer, J. J. Lee, T. Döppner, L. Divol, E. L. Dewald, B. Bachmann, A. G. MacPhee, G. LaCaille, D. K. Bradley, and C. Stoeckl, “Time-Resolved Measurements of the Hot-Electron Population in Ignition-Scale Experiments on the National Ignition Facility” (invited).

F. J. Marshall and P. B. Radha, “Masked Backlighter Technique Used to Simultaneously Image X-Ray Absorption and X-Ray Emission from an ICF Plasma.”

C. Stoeckl, M. Bedzyk, G. Brent, R. Epstein, G. Fiksel, D. Guy, V. N. Goncharov, S. X. Hu, S. Ingraham, D. W. Jacobs-Perkins, R. K. Jungquist, F. J. Marshall, C. Mileham, P. M. Nilson, T. C. Sangster, M. J. Shoup III, and W. Theobald, “Soft X-Ray Backlighting of Cryogenic Implosions Using a Narrowband Crystal Imaging System” (invited).

S. X. Hu, “Attosecond Control of Photoabsorption Through Manipulating the Electron–Electron Correlation,” 45th Annual DAMOP Meeting, Madison, WI, 2–6 June 2014.

The following presentations were made at CLEO 2014, San Jose, CA, 8–13 June 2014:

S.-W. Bahk, J. Bromage, and J. D. Zuegel, “A Linear Phase-Conjugation Imaging (LPCI) System.”

J. Bromage and C. Dorrer, “Pump-to-Signal Spatial Modulation Transfer in Noncollinear Optical Parametric Amplifiers.”

J. Bromage, R. G. Roides, S.-W. Bahk, C. Mileham, L. E. McIntire, C. Dorrer, and J. D. Zuegel, “A White-Light–Seeded Front End for Ultra-Intense Optical Parametric Chirped-Pulse Amplification.”

C. Dorrer, “Spectral and Temporal Properties of Optical Signals with Multiple Sinusoidal Phase Modulations.”

C. Dorrer, R. G. Roides, J. Bromage, and J. D. Zuegel, “Self-Phase Modulation Compensation in a Regenerative Amplifier Using Cascaded Second-Order Nonlinearities.”

J. D. Zuegel, J. Bromage, S.-W. Bahk, I. A. Begishev, J. Bunkenburg, T. Conley, C. Dorrer, D. H. Froula, H. Huang, R. K. Jungquist, C. Kellogg, T. J. Kessler, E. Kowaluk, M. Millecchia, S. F. B. Morse, A. V. Okishev, J. B. Oliver, T. Petersen, and J. Qiao, “Status of High-Energy OPCPA at LLE and Future Prospects” (invited).

The following presentations were made at the 44th Annual Anomalous Absorption Conference, Estes Park, CO, 8–13 June 2014.

K. S. Anderson, P. W. McKenty, T. J. B. Collins, J. A. Marozas, M. Lafon, and R. Betti, “An Implosion-Velocity Survey for Shock Ignition at the National Ignition Facility.”

D. H. Edgell, V. N. Goncharov, I. V. Igumenshchev, D. T. Michel, J. F. Myatt, and D. H. Froula, “Two-Plasmon–Decay Scaling for Improved-Performance Cryogenic Implosion Strategies.”

R. K. Follett, D. H. Edgell, R. J. Henchen, S. X. Hu, D. T. Michel, J. F. Myatt, H. Wen, and D. H. Froula, “Observation of Two-Plasmon–Decay Common Plasma Waves Using Ultra-violet Thomson Scattering.”

D. H. Froula, T. J. Kessler, G. Fiksel, I. V. Igumenshchev, V. N. Goncharov, H. Huang, S. X. Hu, J. H. Kelly, D. T. Michel, and A. Shvydky, “Mitigation of Cross-Beam Energy Transfer in Direct-Drive Implosions on OMEGA.”

J. A. Marozas, T. J. B. Collins, J. D. Zuegel, P. B. Radha, F. J. Marshall, and W. Seka, “Cross-Beam Energy Transfer Mitigation Strategy for NIF Polar Drive.”

J. F. Myatt, J. Shaw, J. Zhang, A. V. Maximov, R. W. Short, W. Seka, D. H. Edgell, D. H. Froula, D. F. DuBois, D. A. Russell, and H. X. Vu, “A Numerical Investigation of Two-Plasmon–Decay Localization in 60-Beam Spherical Implosion Experiments on OMEGA.”

S. P. Regan, R. Epstein, B. A. Hammel, L. J. Suter, H. A. Scott, M. A. Barrios, D. K. Bradley, D. A. Callahan, C. Cerjan, G. W. Collins, T. Dittrich, S. N. Dixit, T. Doepfner, M. J. Edwards, K. B. Fournier, S. Glenn, S. H. Glenzer, I. E. Golovkin, S. W. Haan, A. Hamza, D. Hinkel, H. Huang, O. A. Hurricane, C. A. Iglesias, N. Izumi, J. Jaquez, O. S. Jones, J. D. Kilkenny, J. L. Kline, G. A. Kyrala, O. L. Landen, T. Ma, J. J. MacFarlane, A. J. Mackinnon, R. C. Mancini, R. L. McCrory, N. B. Meezan, D. D. Meyerhofer, A. Nikroo, A. Pak, H. S. Park, P. K. Patel, J. Ralph, B. A. Remington, T. C. Sangster, V. A. Smalyuk, P. T. Springer, R. P. J. Town, and B. G. Wilson, “X-Ray Spectroscopy of Implosions at the National Ignition Facility” (invited).

W. Seka, J. F. Myatt, J. Zhang, R. W. Short, J. A. Delettrez, D. H. Froula, D. T. Michel, A. V. Maximov, V. N. Goncharov, and I. V. Igumenshchev, “Multibeam Interaction Processes Relevant to Direct-Drive Inertial Confinement Fusion.”

R. W. Short, J. F. Myatt, J. Zhang, and W. Seka, “Absolute and Convective Two-Plasmon Decay Driven by Multiple Laser Beams.”

A. A. Solodov, W. Theobald, K. S. Anderson, A. Shvydky, R. Epstein, P. M. Nilson, R. Betti, J. F. Myatt, C. Stoeckl, L. C. Jarrott, C. McGuffey, B. Qiao, F. N. Beg, M. S. Wei, and R. B. Stephens, “Simulations of Integrated Fast-Ignition Experiments on OMEGA.”

W. Theobald, R. Nora, M. Lafon, K. S. Anderson, A. Casner, M. Hohenberger, F. J. Marshall, D. T. Michel, C. Reverdin, X. Ribeyre, T. C. Sangster, W. Seka, A. A. Solodov, C. Stoeckl, A. Vallet, J. Peebles, M. S. Wei, B. Yaakobi, and R. Betti,

“Strong-Shock Generation and Laser–Plasma Interactions for Shock-Ignition Inertial Fusion” (invited).

R. Yan, J. Li, and C. Ren, “Intermittent Laser–Plasma Interactions and Hot-Electron Generation in Shock Ignition.”

—————
The following presentations were made at Research at High Pressure, Biddeford, ME, 22–27 June 2014:

M. C. Gregor, C. A. McCoy, T. R. Boehly, D. E. Fratanduono, and P. M. Celliers, “The Release Behavior of High-Density Carbon.”

C. A. McCoy, M. C. Gregor, T. R. Boehly, D. E. Fratanduono, and P. M. Celliers, “Sound-Speed Measurements with Non-Steady Wave Correction.”

—————
D. T. Michel, R. S. Craxton, A. K. Davis, R. Epstein, V. Yu. Glebov, V. N. Goncharov, S. X. Hu, I. V. Igumenshchev, D. D. Meyerhofer, P. B. Radha, T. C. Sangster, W. Seka, C. Stoeckl, and D. H. Froula, “Implosion Dynamics in Direct-Drive Experiments,” 41st EPS Conference on Plasma Physics, Berlin, Germany, 23–27 June 2014 (invited).

—————
K. S. Anderson, “A Conceptual Summary of Basic Mathematics in Laser Fusion,” Toyota-RIT Applied Math Initiative, Rochester, NY, 30 June–3 July 2014.

